

Kinetic Methods for Understanding Linker Exchange in Metal-Organic Frameworks

Author: Joseph Morabito

Persistent link: <http://hdl.handle.net/2345/bc-ir:107593>

This work is posted on [eScholarship@BC](#),
Boston College University Libraries.

Boston College Electronic Thesis or Dissertation, 2017

Copyright is held by the author. This work is licensed under a Creative Commons Attribution-NonCommercial-NoDerivatives 4.0 International License (<http://creativecommons.org/licenses/by-nc-nd/4.0>).

Kinetic Methods for Understanding Linker Exchange in Metal-Organic Frameworks

Joseph V. Morabito

A dissertation
submitted to the Faculty of
the department of Chemistry
in partial fulfillment
of the requirements for the degree of
Doctor of Philosophy

Boston College
Morrissey College of Arts and Sciences
Graduate School

June 2017

KINETIC METHODS FOR UNDERSTANDING LINKER EXCHANGE IN METAL-ORGANIC FRAMEWORKS

Joseph V. Morabito

Advisor: Prof. Chia-Kuang (Frank) Tsung, Ph.D.

ABSTRACT Exchange reactions have enabled a new level of control in the rational, stepwise preparation of metal-organic framework (MOF) materials. However, their full potential is limited by a lack of understanding of the molecular mechanisms by which they occur. This dissertation describes our efforts to understand this important class of reactions in two parts. The first reports our use of a linker exchange process to encapsulate guest molecules larger than the limiting pore aperture of the MOF. The concept is demonstrated, along with evidence for guest encapsulation and its relation to a dissociative linker exchange process. The second part describes our development of the first quantitative kinetic method for studying MOF linker exchange reactions and our application of this method to understand the solvent dependence of the reaction of ZIF-8 with imidazole. This project involved the collection of the largest set of rate data available on any MOF linker exchange reaction. The combination of this dataset with small molecule encapsulation experiments allowed us to formulate a mechanistic model that could account for all the observed kinetic and structural data. By comparison with the kinetic behavior of complexes in solution, we were able to fit the kinetic behavior of ZIF-8 into the broader family of coordination compounds. Aside from the specific use that our kinetic data may have in predicting the reactivity of ZIF linker exchange, we hope that the conceptual bridges made between MOFs and related metal-organic compounds can help reveal underlying patterns in behavior and advance the field.

ACKNOWLEDGEMENTS

No achievement can occur without the support of people behind the scenes. I want to thank first and foremost my incredible wife-to-be Isabelle. Your unconditional love, insatiable curiosity, and unflappable willpower were my rock of stability on this sometimes-stormy academic voyage. To our next adventure!

To my parents, for whom I have everything to thank, but in particular for the values of truth and curiosity you fostered in me. Your love and support carried me through everything and I don't say thank you enough.

Thanks to my friends, especially Brett, James, Nick, Jon, JP, Mark, Troy, Lotta, and Tobyn. I can't imagine a more stimulating group. You are the weirdest group of people I have ever met, and by weirdest I mean...

Special thanks, of course, to my advisor, Frank. You've known me through many stages, and your guidance and patient way of allowing me figure it out have allowed me to grow into the researcher that I am today. May the collaboration not end here!

Thanks to Ken Metz, who taught me more than he may realize. They say you learn the most by teaching, and it helps to have a model of what teaching well looks like.

Thanks to my friends in the lab, particularly Alli. Your friendship made the long days enjoyable.

Thanks to the scientists who came before. To Wilkins, Swaddle, and Helfferich. To Reddy, Jencks, and Hoffman. You shared your hard-won secrets with the belief that together we prosper. I am proud to continue your legacy.

Thanks finally to my committee members, Dunwei Wang and Matthias Waegele.

TABLE OF CONTENTS

Table of Contents	iv
List of tables.....	v
List of figures.....	viii
List of abbreviations.....	xii
1.0 Chapter 1: Linker exchange reactions in metal–organic frameworks.....	1
1.1 Metal-organic frameworks	1
1.2 Linker exchange in MOFs	2
1.3 Motivation for studying the mechanism of MOF linker exchange.....	3
1.4 The scope of this dissertation.....	5
References.....	7
2.0 Chapter 2: Molecular Encapsulation Beyond the Aperture Size Limit Through Dissociative Linker Exchange in Metal-Organic Framework Crystals.	9
Introduction	10
Results and discussion.....	11
Conclusion.....	30
Experimental methods	31
References.....	39
3.0 Chapter 3: Understanding the Solvent-Dependence of MOF Linker Exchange Kinetics in the Reaction of ZIF-8 with Imidazole	44
Introduction	45
Results and discussion.....	49
Conclusion.....	81
Experimental methods	84
References.....	93
4.0 Appendix I: Kinetics plots	122
5.0 Appendix II: Calculations of surface ligand density.....	133
6.0 Appendix III: Powder X-ray diffraction patterns.....	138
7.0 Appendix IV: Transmission electron micrographs.....	153
8.0 Appendix V: Solvent properties	158

LIST OF TABLES

Chapter 2

Table 2-1. Leaching experiments

Table 2-2. Fluorescence lifetime and fluorescence intensity measurements

Table 2-3. Observed rate constants determined by initial rates

Table 2-4. The spin-lattice relaxation times (T_1) determined for each proton in the acid-digested solutions of the $\text{Zn}(\text{MeIm})_{2-x}(\text{Im})_x$ products

Chapter 3

Table 3-1. The parameters obtained from the particle size distributions

Table 3-2. Experimental Rate Constants (k_{obs} in $\text{s}^{-1} \times 10^{-6}$) and Calculated Half-lives of Ligand Exchange of ZIF-8/**sod**- $\text{Zn}(\text{MeIm})_2$ with Imidazole

Table 3-3. Values for conversion and phases observed for 10-d reactions at 70 °C

Table 3-4. Spin-lattice relaxation time, T_1 , values for samples of digested $\text{Zn}(2\text{-MeIm})_{2-x}(\text{Im})_x$ at various values of conversion

Appendix I

Table AI-1. Values of conversion for reactions in DMSO at 70 °C

Table AI-2. Values of conversion for reactions in ethanol at 70 °C

Table AI-3. Values of conversion for reactions in *n*-butanol at 70 °C

Table AI-4. Values of conversion for reactions in acetonitrile at 70 °C

Table AI-5. Values of conversion for reactions in methanol at 70 °C

Table AI-6. Values of conversion for reactions in water at 4 °C

Appendix II

Table AII-1. The correlation between ZIF-8 crystal size and the y-intercept in conversion vs. time plots

Appendix V

Table AV-1. Parameters of solvent polarity

Table AV-2. Parameters of solvent Lewis acidity

Table AV-3. Parameters of solvent Lewis basicity

Table AV-4. Parameters of solvent Brønsted-Lowry acidity and solvent effects on imidazole and imidazolium acidity

Table AV-5. Solvent molecular sizes and parameters affecting mass transport in solution and in ZIF-8

Table AV-6. Imidazole molecules per pore on average

LIST OF FIGURES

Chapter 1

Figure 1-1. From metal complexes in solution to extended metal-organic frameworks

Figure 1-2. The solid-liquid linker exchange reaction of ZIF-8 with imidazole in solution

Chapter 2

Figure 2-1. Molecular encapsulation of a large organic guest into the pores of ZIF-8 through dissociative linker exchange

Figure 2-2. The molecular dimensions of the guest molecules (Rhodamine 6G and triphenylphosphine) compared to the pore dimensions of the host material (ZIF-8)

Figure 2-3. Rhodamine 6G encapsulation through ZIF-8 linker exchange

Figure 2-4. Transmission electron microscope (TEM) images and particle size distributions (PSDs) of ZIF-8 crystals

Figure 2-5. Powder X-ray diffraction patterns of R6G@ZIF-8

Figure 2-6. ZIF-8 surface interaction experiments

Figure 2-7. PVP washing experiments

Figure 2-8. Observed rate constants (k_{obs}) for exchange of ZIF-8 with imidazole at different initial concentrations of imidazole

Figure 2-9. Representative $^1\text{H-NMR}$ spectra of acid-digested $\text{Zn}(\text{MeIm})_{2-x}(\text{Im})_x$ over the course of the exchange reaction for the series with $\text{Im/MeIm} = 30$

Figure 2-10. Plot of conversion vs. time of the $\text{Zn}(\text{MeIm})_2$ to $\text{Zn}(\text{MeIm})_{2-x}(\text{Im})_x$ exchange reaction at varying concentrations of imidazole

Figure 2-11. A representative energy dispersive X-ray spectrum of PPh_3 @ZIF-8 loaded with initial $[\text{PPh}_3]$ of 220 mM

Figure 2-12. Powder X-ray diffraction patterns of PPh_3 @ZIF-8

Figure 2-13. N_2 absorption (filled symbols) and desorption (open symbols) isotherms of ZIF-8 (red), 165 mM triphenylphosphine@ZIF-8 (blue) and 220 mM triphenylphosphine@ZIF-8 (green).

Chapter 3

Figure 3-1. The important roles of MOF metal-ligand bond reversibility in two contexts

Figure 3-2. The structure of ZIF-8/*sod*- $\text{Zn}(\text{MeIm})_2$ reduced to a subunit complex for the purpose of drawing reaction schemes

Figure 3-3. Two hypothetical pathways for linker exchange of *sod*- $\text{Zn}(\text{MeIm})_2$ with imidazole: (I) zero-order in imidazole and (II) first-order in imidazole

Figure 3-4. The structural basis for kinetic experiments to rule out rate control by diffusion

Figure 3-5. The dependence of linker exchange kinetics on ZIF-8 crystal size as measured in *n*-butanol at 70 °C with (a) 0.0735 M and (b) 0.294 M imidazole

Figure 3-6. Particle size distributions obtained from TEM imaging of size-controlled ZIF-8 particles

Figure 3-7. The correlation between ZIF-8 crystal size and the y-intercept in conversion vs. time plots for (a) 0.0735 M and (b) 0.294 M imidazole in *n*-butanol at 70 °C

Figure 3-8. Plots of observed initial rate constant, k_{obs} , versus free concentration of imidazole, $[\text{ImH}_0]$, for (a) dimethyl sulfoxide, (b) ethanol, (c) 1-butanol, (d) acetonitrile, (e) methanol, and (f) water (filled) and deuterium oxide (open)

Figure 3-9. Hypothesis that second-order in imidazole kinetics could be a consequence of imidazole dimers playing a key role in a first step, rate-determining proton transfer to the 2-methylimidazolate linker

Figure 3-10. Encapsulation of a large organic dye by a dissociative linker exchange pathway in ZIF-8/*sod*-Zn(MeIm)₂

Figure 3-11. Loadings of Rhodamine 6G (R6G) dye guest into ZIF-8 as determined by digestion UV/vis

Figure 3-12. Photographs of the solvent dependent encapsulation of Rhodamine 6G dye encapsulation in ZIF-8

Figure 3-13. Equilibrium constant versus initial $[\text{ImH}]$ for 10-day reactions at 70 °C

Figure 3-14. Eyring plot used to estimate k_{obs} at 4 °C in *n*-butanol with $[\text{ImH}_0]$ of 0.0735 M

Figure 3-15. A three-pathway mechanism consistent with the experimental data on ZIF-8/*sod*-Zn(MeIm)₂ linker substitution with imidazole (ImH)

Figure 3-16. A representative ¹H-NMR spectrum from the kinetics measurements showing the peaks used for analysis

Figure 3-17. Detail of the imidazole protons in the ¹H-NMR spectra for representative samples in a kinetics run

Figure 3-18. ¹H-NMR spectra from a T_1 measurement (entry 3 in Table 3-4) by the inversion recovery method

Appendix I

Figure AI-1. Conversion versus time plots used for determining the rate constants of ligand exchange in dimethyl sulfoxide (DMSO) at 70 °C.

Figure AI-2. Conversion versus time plots used for determining the rate constants of ligand exchange in ethanol at 70 °C.

Figure AI-3. Conversion versus time plots used for determining the rate constants of ligand exchange in *n*-butanol at 70 °C.

Figure AI-4. Conversion versus time plots used for determining the rate constants of ligand exchange in acetonitrile at 70 °C for ACS grade acetonitrile (filled triangle, ▼) or anhydrous acetonitrile (open triangle, ▽, only in the $[\text{imidazole}] = 0.294$ M plot).

Figure AI-5. Conversion versus time plots used for determining the rate constants of ligand exchange in methanol at 70 °C.

Figure AI-6. Conversion versus time plots used for determining the rate constants of ligand exchange in water and deuterium oxide at 4 °C.

Figure AI-7. Conversion (as χ_{MeIm}) versus time plots used for determining the rate constants of ligand exchange for size-controlled ZIF-8 samples in *n*-butanol (BuOH) with 0.0735 M imidazole at 70 °C.

Figure AI-8. Conversion (as χ_{MeIm}) versus time plots used for determining the rate constants of ligand exchange for size-controlled ZIF-8 samples in *n*-butanol (BuOH) with 0.294 M imidazole at 70 °C.

Figure AI-9. Conversion versus time plots used for determining the rate constants of ligand exchange in *n*-butanol with 0.0735 M imidazole at 75, 85, 95, and 105 °C.

Appendix II

Figure AII-1. Two typical surfaces of ZIF-8 {100} and {110} used to calculate the surface density (molecules per nm²) of surface RIm(H) species.

Appendix III

Figure AIII-1. PXRD patterns of the products with the highest values of conversion that were used for determining rate constants in dimethyl sulfoxide solutions

Figure AIII-2. PXRD patterns of the products with the highest values of conversion that were used for determining rate constants in ethanol solutions

Figure AIII-3. PXRD patterns of the products with the highest values of conversion that were used for determining rate constants in *n*-butanol solutions

Figure AIII-4. PXRD patterns of the products with the highest values of conversion that were used for determining rate constants in acetonitrile solutions

Figure AIII-5. PXRD patterns of the products with the highest values of conversion that were used for determining rate constants in methanol solutions

Figure AIII-6. PXRD patterns of the products with the highest values of conversion that were used for determining rate constants in aqueous solutions at 4 °C

Figure AIII-7. PXRD patterns for a mixed **sod/zni** phase samples

Figure AIII-8. Plots of the data from Table 3-3: conversion ($= \chi_{\text{Im}} = 1 - \chi_{2\text{-MeIm}}$) versus initial [ImH]

Figure AIII-9. Change in free energy, ΔG° , versus initial [ImH] for 10-d reactions at 70 °C.

Figure AIII-10. PXRD patterns of the products from 10-day reactions in dimethyl sulfoxide

Figure AIII-11. PXRD patterns of the products from 10-day reactions in ethanol

Figure AIII-12. PXRD patterns of the products from 10-day reactions in *n*-butanol

Figure AIII-13. PXRD patterns of the products from 10-day reactions in acetonitrile

Figure AIII-14. PXRD patterns of the products from 10-day reactions in methanol

Figure AIII-15. PXRD patterns of the products from 6-day reactions in water at 4 °C

Appendix IV

Figure AIV-1. TEM images used to calculate the grain size distribution of the commercial sample, Basolite Z1200, with a D50 of 265 nm

Figure AIV-2. TEM images used to calculate the grain size distribution of the sample “M” with a D50 of 85 nm

Figure AIV-3. TEM images used to calculate the grain size distribution of the sample “L” with a D50 of 125 nm

Figure AIV-4. TEM images used to calculate the grain size distribution of the sample “XL” with a D50 of 239 nm

Figure AIV-5. TEM images used to calculate the grain size distribution of the sample “XXL” with a D50 of 404 nm

Figure AIV-6. TEM images used to calculate the grain size distribution of the sample with a D50 of 1.96 μm

Figure AIV-7. TEM images used to calculate the grain size distribution of the sample with a D50 of 7.76 μm

LIST OF ABBREVIATIONS

BuOH	<i>n</i> -butanol
conv	conversion
d	days
DMF	N,N-dimethylformamide
DMSO	dimethylsulfoxide
EtOH	ethanol
ImH	imidazole
Im ⁻	imidazolate
h	hours
MeCN	acetonitrile
MeImH	2-methylimidazole
MeIm ⁻	2-methylimidazolate
MeOH	methanol
min	minutes
MSM	methyl sulfonyl methane
sod	the sodalite topology
ZIF-8	the metal-organic framework with composition zinc(II)- <i>bis</i> -2-methylimidazolate and the sodalite topology
zni	the framework topology isostructural with zinc iodide

1.0 CHAPTER 1

Linker exchange reactions in metal–organic frameworks

1.1 Metal-organic frameworks

Metal-organic frameworks (MOFs) can be considered the three-dimensional analogs of simpler one-dimensional metal complexes in solution. For example, the MOF ZIF-8,^{1,2} with Zn(II) nodes connected by 2-methylimidazolate linkers in the sodalite topology can be considered the open framework analog of the $\text{Zn}(\text{imidazole})_4 \cdot 2\text{ClO}_4$ complex, which also features tetrahedral Zn(II) (Figure 1-1).³

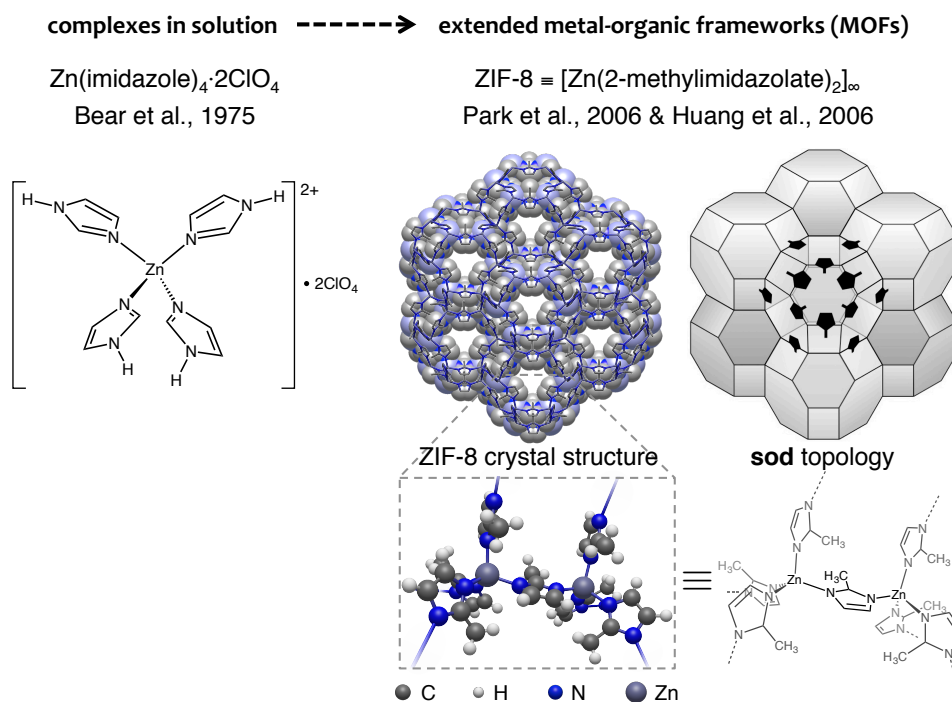


Figure 1-1. From metal complexes in solution to extended metal-organic frameworks.

1.2 Linker exchange in MOFs

Like their counterpart complexes in solution, MOFs can undergo ligand exchange reactions, in which their organic linkers are replaced by others from solution. For example the 2-methylimidazolate (MeIm^-) linkers of ZIF-8 can be replaced with imidazolate (Im^-) through a reaction of the solid MOF with imidazole (ImH) from solution (Figure 1-2).⁴ Likewise, $\text{Zn}(\text{ImH})_4 \cdot 2\text{ClO}_4$ undergoes rapid ligand exchange in solution,⁵ as do most complexes of $\text{Zn}(\text{II})$. We can intuit that these processes are closely related; however, the exact correspondences are unknown. This is because, whereas the kinetics and mechanism of ligand substitutions of metal complexes in solution is a mature field,⁶ no systematic study of the mechanisms of linker exchange in MOFs has been undertaken since the first report of the phenomenon in 2011.⁷

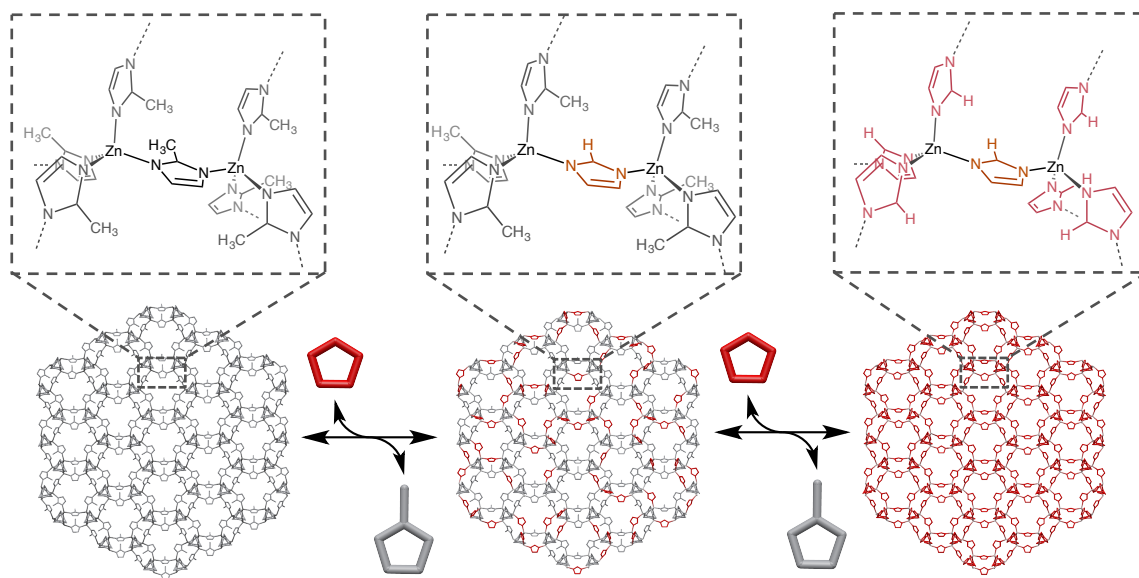


Figure 1-2. The solid-liquid linker exchange reaction of ZIF-8 with imidazole in solution, involving stepwise replacement of the organic linkers of the framework without dissolution of the MOF crystals.

1.3 Motivation for studying the mechanism of MOF linker exchange

The study of reaction mechanism has long been central to the study of coordination compounds and to improvements in their synthesis. In fact, in 1962, the first ever article in the new journal *Inorganic Chemistry* began, “Mechanisms of reactions of metal complexes have been studied in some detail and progress has been made toward a better understanding of these reaction processes. It is hoped that such knowledge will lead to the synthesis of new compounds and to new methods for the preparation of known compounds.”⁸

Our motivation behind studying the mechanism of MOF linker exchange was that we might be able to rationally predict how to guide a MOF linker exchange reaction towards a desired structural or stereochemical outcome. A well-known example of the power of mechanistic knowledge on ligand substitution for directing structural outcomes is the *trans effect* in square planar Pt(II) compounds.⁶ The *trans effect*—the observation that the substitution kinetics of a ligand are dramatically affected by the ligand *trans* to the leaving group—has enabled the rational preparation of compounds with stereochemical control, including most notably the anticancer drug cisplatin.

There are many reasons why we would want to direct the structural outcome of a linker substitution reaction in a MOF. For example, consider we introduce two linkers with different functional groups, and are somehow able to direct them with specific orientation to each other. Such an environment could create pockets with exquisite specificity for the binding of a substrate, like the active site of an enzyme. Next, consider if we could direct the reactivity of a *trans* linker at an initially symmetrical MOF node. This could introduce anisotropic properties to the entire crystal that could result in useful

mechanical responses such as linear actuation. Finally, consider if we could exchange in linkers with different functionality and direct them to substitute with a gradient of concentration across a MOF crystal (core-shell/radial gradient) or MOF membrane (layered/linear gradient). This could create materials with *gradients of chemical potential* that could direct transport of molecules like the selective ion channels in cell membranes.

Beyond these futuristic possibilities, there are many more prosaic, yet urgent matters in MOF synthesis that could be addressed by mechanistic knowledge of linker exchange. For example, attempted exchange reactions frequently fail to result in high incorporation of the new linker, or in other cases high incorporation is reached only at the expense of an undesirable crystalline phase change. In an ideal world, MOF linker exchange would be a routine tool to obtain a desired functionality in a MOF, like cross coupling or alkyne-azide click chemistry in organic synthesis. In reality, however, one linker exchange reaction often becomes a project in and of itself, requiring extensive trial and error to find the right conditions. Mechanistic knowledge of the linker exchange process could make these reactions predictable and allow for rationale diagnosis of a problem, rather than time-intensive screening of conditions.

An example of the power of mechanistic thinking for the rational synthesis of MOFs using exchange reactions is found in a report from Liu et al.⁹ (using metal ion rather than organic linker exchange). The authors obtained a MOF with uncommonly high chemical stability in a stepwise process that involved (1) synthesis of a MOF with Fe(II) nodes, (2) exchange of Fe(II) with Cr(II), and (3) oxidation of Cr(II) to Cr(III). The inertness of Cr(III) causes MOF self-assembly using that ion to fail to result in structures with long-range order. The stepwise approach takes advantage of the much higher kinetic

lability of Fe(II) complexes to assemble to MOF, before locking in the chemically stable structure with the reaction to install Cr(III). If this level of control can be reached knowing nothing more than the water exchange rate constants of the transition metal ions,⁶ imagine what could be accomplished with specific knowledge on the molecular pathways of linker exchange.

1.4 The scope of this dissertation

Our interest in the mechanism of MOF linker exchange began with a novel idea for preparing encapsulated catalysts in MOFs. This idea was based on our reading of the scant literature available on linker exchange at the time and our hypothesis that certain aspects of the reaction process might allow us the chance to encapsulate guests that are larger than the pore window (or *aperture*) that traditionally limits the size of a guest that may be incorporated. The demonstration of this idea, along with the evidence for guest encapsulation and its relation to linker exchange kinetics are the subject of Chapter 2.

As the literature on MOF linker exchange developed during and soon after the encapsulation project, we realized that no groups were paying attention to the mechanisms of linker exchange. This omission was particularly striking, considering that a vast body of knowledge exists around the substitution mechanisms of simpler complexes in solution. Some of the lack of attention on substitution mechanisms can probably be attributed to the interdisciplinary nature of MOF research. MOFs are unique among coordination compounds in that many of the groups studying their properties do not come from a traditional inorganic chemistry background. This exciting dynamic of having so many viewpoints on one material makes for interesting conferences, but it also

means that knowledge that is canonical for one discipline may unfamiliar to others, even as they run the same reactions.

The lack of a shared background was, however, not the only barrier stopping researchers from studying the mechanism of MOF linker exchange. Soon after beginning our work, we quickly realized that the reactions are complicated to study kinetically, as compared to complexes in solution. First, there is a lack of suitable spectroscopic signatures for following exchange, whereas such techniques were essential in the study of ligand substitution mechanisms in solution. Moreover, mass transport—a limitation for only the fastest reactions in solution, where barriers to diffusion are low—becomes significant in a MOF, and we had to devise methods to test for and circumvent diffusion limitations.

Our development of a suitable kinetic method to study linker exchange reactions in MOFs and our application of this method to study the solvent dependence of the reaction of ZIF-8 with imidazole are the subject of Chapter 3. Significantly, this chapter also includes our development of a mechanistic model that can rationalize the observed kinetic and structural behavior of the linker exchange reaction in ZIF-8. This proposal is the first of its kind for this class of reactions, and it was enabled by our collection of the largest set of rate data yet for a linker substitution reaction in a MOF. Through comparison with the known behavior of related complexes in solution, we were able to discern in what ways linker exchange in MOFs was like and unlike the behavior of complexes in solution. In fitting the kinetic behavior of MOFs this way into the broader family of coordination compounds, we have strived to build bridges between disciplinary sets of knowledge. Beyond the immediate impact of our research for understanding linker

exchange reactions in ZIFs, we hope that these bridges will advance the field of MOFs and metal–organic materials by helping researchers to connect the dots and see the patterns that underlie the kinetic behavior of coordination compounds.

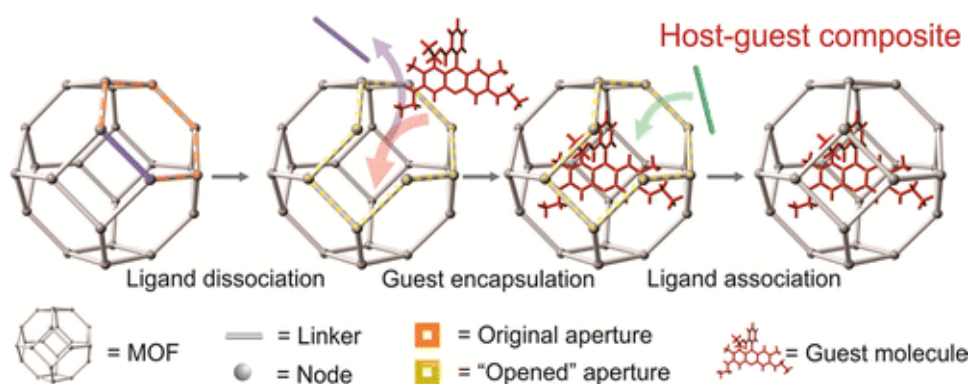
References

- (1) Park, K. S.; Ni, Z.; Côté, A. P.; Choi, J. Y.; Huang, R.; Uribe-Romo, F. J.; Chae, H. K.; O’Keefe, M.; Yaghi, O. M. Exceptional chemical and thermal stability of zeolitic imidazolate frameworks. *Proc. Natl. Acad. Sci. USA* **2006**, *103*, 10186–10191.
- (2) Huang, X.-C.; Lin, Y.-Y.; Zhang, J.-P.; Chen, X.-M. Ligand-Directed Strategy for Zeolite-Type Metal–Organic Frameworks: Zinc(II) Imidazolates with Unusual Zeolitic Topologies. *Angew. Chem. Int. Ed.* **2006**, *45*, 1557–1559.
- (3) Bear, C. A.; Duggan, K. A.; Freeman, H. C. Tetraimidazolezinc(II) Perchlorate. *Acta Crystallogr. Sect. B* **1975**, *31*, 2713–2715.
- (4) Karagiari, O.; Lalonde, M. B.; Bury, W.; Sarjeant, A. A.; Farha, O. K.; Hupp, J. T. Opening ZIF-8: A Catalytically Active Zeolitic Imidazolate Framework of Sodalite Topology with Unsubstituted Linkers. *J. Am. Chem. Soc.* **2012**, *134*, 18790–18796.
- (5) Sham, S. and Wu, G. Zinc-67 NMR study of tetrahedral and octahedral zinc sites with symmetrical oxygen, nitrogen, and sulfur ligands *Can. J. Chem.* **1999**, *77*, 1782–1787.
- (6) Wilkins, R. G. *Kinetics and Mechanism of Reactions of Transition Metal Complexes*, 2nd ed.; VCH: New York, 1991.
- (7) Burnett, B. J.; Barron, P. M.; Hu, C.; Choe, W. Stepwise Synthesis of Metal–Organic Frameworks: Replacement of Structural Organic Linkers. *J. Am. Chem. Soc.* **2011**, *133*, 9984–9987.

- (8) Basolo, F. and Hammaker, G. S. Synthesis and Isomerization of Nitritopentammine Complexes of Rhodium(III), Iridium(III), and Platinum(IV). *Inorg. Chem.* **1962**, *1*, 1–5.
- (9) Liu, T. - F.; Zou, L.; Feng, D.; Chen, Y.-P.; Fordham, S.; Wang, X.; Liu, Y.; Zhou, H.-C. Stepwise Synthesis of Robust Metal–Organic Frameworks via Postsynthetic Metathesis and Oxidation of Metal Nodes in a Single-Crystal to Single-Crystal Transformation. *J. Am. Chem. Soc.* **2014**, *136*, 7813–7816.

2.0 CHAPTER 2

Molecular Encapsulation Beyond the Aperture Size Limit Through Dissociative Linker Exchange in Metal-Organic Framework Crystals



A significant portion of the work described in this chapter has been published in:

Morabito, J. V.; Chou, L.-Y.; Li, Z.; Manna, C. M.; Petroff, C. A.; Kyada, R. J.; Palomba, J. M.; Byers, J. A.; Tsung, C.-K. Molecular Encapsulation beyond the Aperture Size Limit through Dissociative Linker Exchange in Metal–Organic Framework Crystals. *J. Am. Chem. Soc.* **2014**, *136*, 12540–12543.

2.1 Introduction: Host-guest materials with metal–organic frameworks

The incorporation of functional guest molecules into the cavities of crystalline porous materials makes it possible to engineer these materials for drug delivery,^{1,2} sensing,^{3,4} electrical conductivity,^{5,6} luminescence,^{7,9} and energy conversion.¹⁰⁻¹² Host-guest crystalline porous materials have been studied in aluminosilicate zeolites since the 1980s.¹³ Recently, MOFs have been identified to offer more opportunities for host-guest composites compared to zeolites due to their chemically tunable pore surfaces, their comparatively mild syntheses, and their unique properties such as framework flexibility,¹⁴ post-synthetic modification,¹⁵ and exchangeable organic linkers.^{16,17} The great diversity of MOF properties and structure types has led to various approaches for the synthesis of host-guest composites.^{15,18-20}

Despite these advances, approaches for incorporating large and more diverse guests are still limited to a few specific MOF types. For example, negatively charged MOFs have been utilized to incorporate cationic organic compounds and metals,¹⁸⁻²⁰ and MOFs with unoccupied sites can encapsulate guests through dative bonds.⁵ Despite these successes, many MOFs lack framework charge or unoccupied sites, which prohibits the general applicability of these methods. Alternatively, guest molecules have been covalently bound to the organic linkers of the frameworks,¹⁵ but the loss of degrees of freedom for tethered homogeneous catalysts could lead to decreased activity or selectivity in catalytic applications.²¹

The incorporation of guest molecules in MOFs by diffusion is generally limited to guests that are smaller than the MOF aperture size.¹⁹ This limitation commonly leads to guest molecule leaching, which is particularly problematic for catalytic applications.

Retaining guests in the cavity of MOFs by pursuing strategies that incorporate guests larger than the MOF aperture size could circumvent this problem. Two strategies for this are the ship-in-a-bottle assembly of the guest within the pore subunits and the *de novo* encapsulation of the guest during MOF crystal growth.^{18,22} The ship-in-a-bottle approach is challenging for the assembly of guest molecules that require multiple post-synthetic operations. The *de novo* encapsulation approach does not have this limitation, but it requires that guest molecules not perturb MOF crystal growth and be compatible with conditions used for MOF synthesis.

2.2 A new approach to encapsulate guests: dissociative linker exchange

We introduce here a new concept for incorporating larger and more diverse guest molecules into MOFs (Figure 2-1). In this approach, we take advantage of linker exchange reactions to “open” part of the framework of the pre-synthesized MOF crystals. Expanded apertures created by the linker exchange process allow large guest molecules to diffuse into the MOF pore. After guest incorporation, association of the linker closes the large aperture, trapping the guest molecule in the MOF pore. This new approach to guest incorporation is expected to be general because framework linker exchange has been carried out under various conditions and exists in a large number of MOFs with diverse metal nodes.^{16,17,23-30} An additional practical advantage of decoupling encapsulation and MOF synthesis is that MOF production can be scaled-up independently of guest loading, which is especially relevant since several MOFs, such as ZIF-8, Fe-BTC, HKUST-1, and MIL-53(Al), have become commercially available.

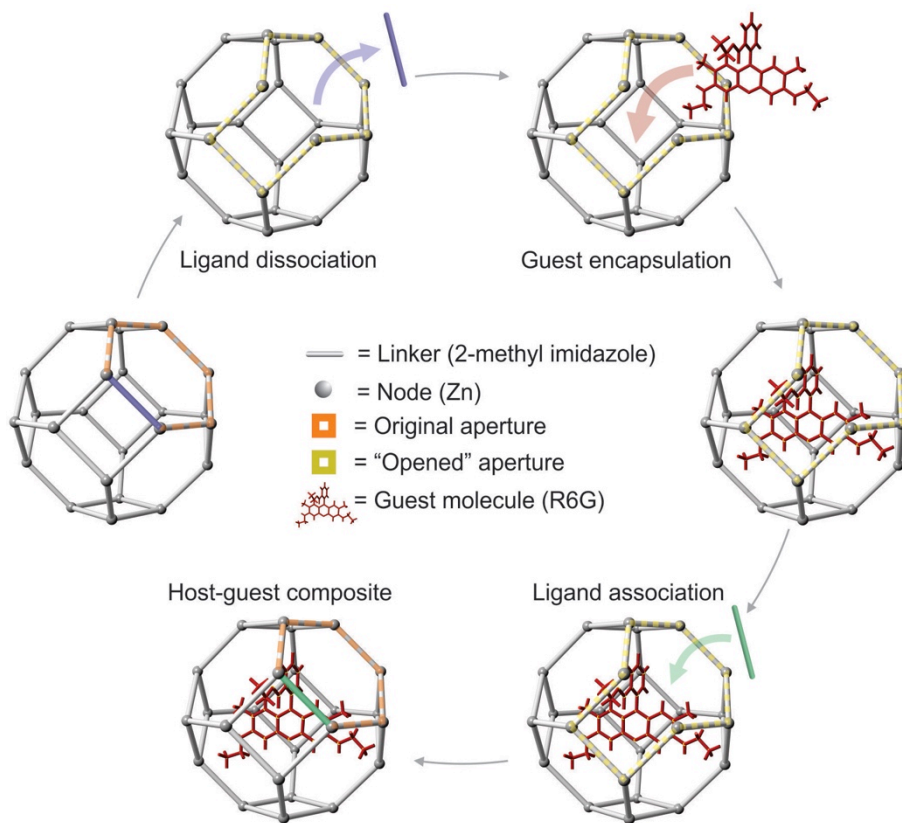


Figure 2-1. Molecular encapsulation of a large organic guest into the pores of ZIF-8 through dissociative linker exchange

It has been reported that the bridging organic linkers in MOF crystals can be exchanged with compatible but chemically distinct linkers without disrupting the underlying MOF crystal structure and morphology. This phenomenon was first reported by Choe for pillared porphyrin paddlewheel frameworks²⁸ and has been optimized by several groups.^{24,25} The linker exchange process has become extremely popular for the diversification of MOFs and is most commonly referred to as solvent-assisted linker exchange (SALE)²⁴ or ligand-based postsynthetic exchange (PSE).²⁵ In order to avoid confusion between MOF bridging ligands and ligands for metals generally, we have

chosen to refer to the framework bridging ligand as a “linker” in all cases. The two terms are equally popular in the MOF literature.

The ability for ligands to exchange between metal centers is ubiquitous in coordination chemistry, where the two limiting pathways for ligand substitution reactions are associative or dissociative mechanisms. In a MOF, the metals are typically coordinatively saturated, a property that we reasoned would make a dissociative mechanism more likely. If dissociative linker substitution occurs in MOFs, we hypothesized the existence of short-lived linker vacancies, which would momentarily expand the pore aperture size to allow the passage of larger guests into the framework. Subsequent reincorporation of the dissociated linker reassembles the MOF with an aperture size that is smaller than the incorporated guest.

2.3 Encapsulation of Rhodamine 6G into ZIF-8 under linker exchange conditions

As a proof of principle, we used the commercially available zeolitic imidazolate framework ZIF-8³² as a model MOF. We also identified two criteria that would be most appropriate for a suitable guest molecule. First, to maximize guest retention, the guest molecule should be larger than the MOF aperture size. For encapsulation in ZIF-8, this requirement makes the ideal guest size between ~ 3.4 and 11.6 \AA , the aperture and pore sizes of ZIF-8, respectively. Second, in order to better quantify the loading, we initially targeted guest molecules that could be easily detectable by UV-Vis spectroscopy. Rhodamine 6G (R6G) was selected as an ideal candidate that meets both criteria outlined above: it is a fluorescent dye ($\lambda_{\text{max}} = 530 \text{ nm}$) with a molecular diameter of $11.3 - 13.7 \text{ \AA}$ (Figure 2-2). The amounts of encapsulated R6G were determined by UV-Vis spectroscopy after acid digestion of the ZIF-8 crystals in methanol.

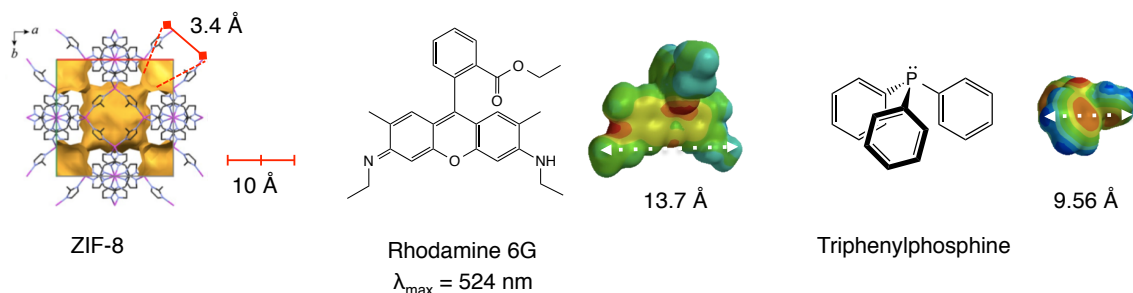


Figure 2-2. The molecular dimensions of the guest molecules (Rhodamine 6G and triphenylphosphine) compared to the pore dimensions of the host material (ZIF-8).

To test whether linker exchange can facilitate guest incorporation, R6G was incubated with ZIF-8 in the presence of 2-methylimidazole as an exogenous linker in butanol at 100 °C for 7 days (Figure 2-3). Exchange of the 2-methylimidazole linker in ZIF-8 with imidazole has been reported under these conditions.¹⁷ After the reaction, the material, henceforth referred to as R6G@ZIF-8, took on a cloudy light pink hue. The structure of the guest encapsulation products was characterized by transmission electron microscopy (TEM) and powder X-ray diffraction (PXRD). Both techniques show no apparent differences after guest encapsulation, suggesting that the guest loading method was not destructive (Figures 2-4 and 2-5).

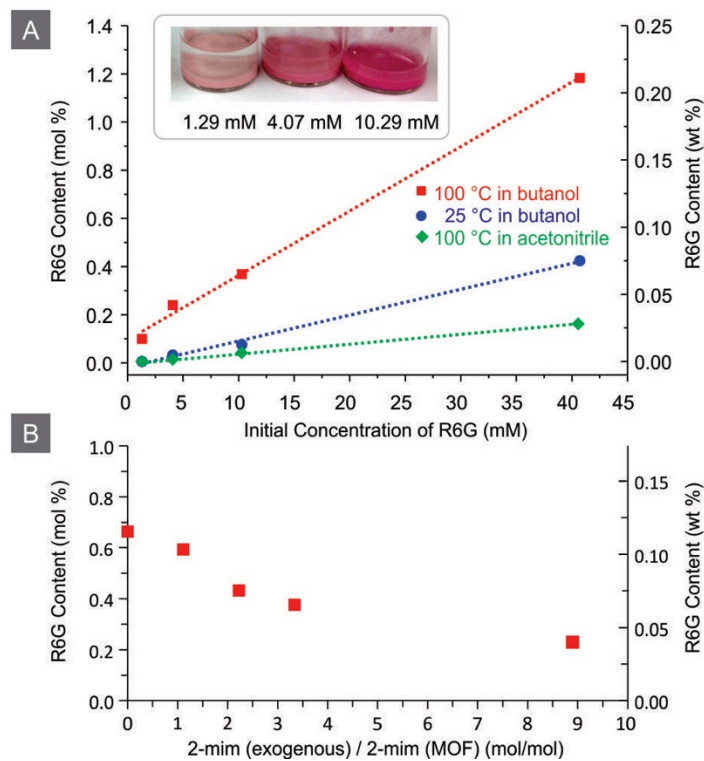


Figure 2-3. Rhodamine 6G encapsulation through ZIF-8 linker exchange. (7 days) (A) R6G loading versus [R6G] at 100 °C (red) and 25 °C (blue) in *n*-butanol and at 100 °C in acetonitrile (green). Inset image shows ZIF-8 after R6G loading at various [R6G] during linker exchange at 100 °C in *n*-butanol. (B) Dependence of R6G encapsulation on the [2-methylimidazole] exogenous linker. Conditions: 10.29 mM of R6G at 100 °C in *n*-butanol for 7 d.

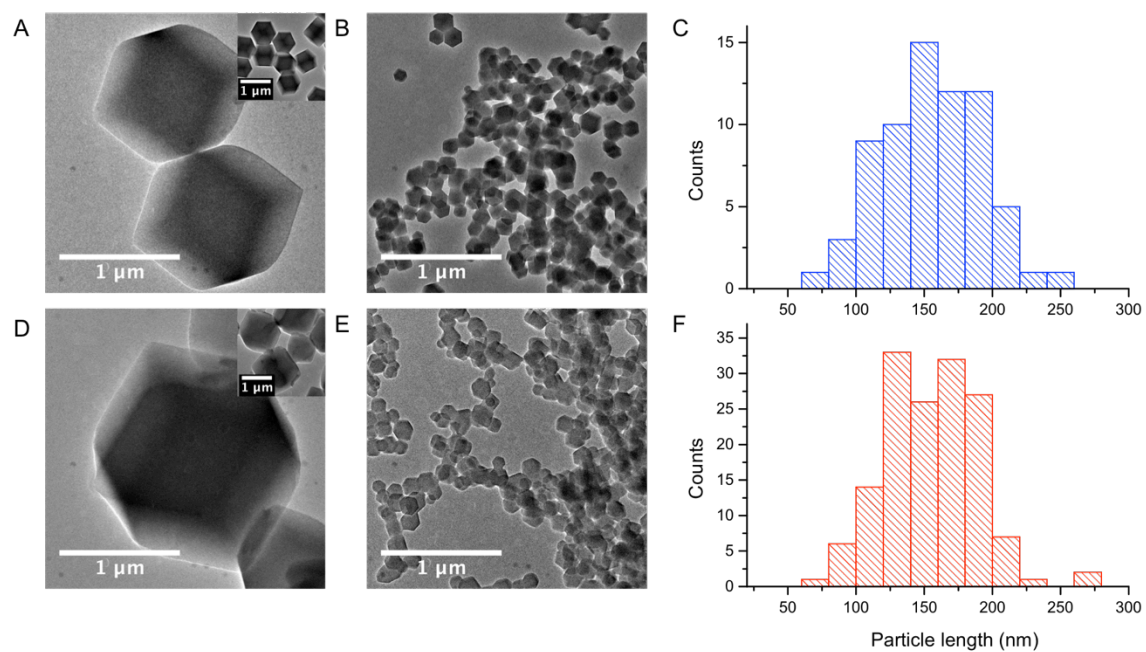


Figure 2-4. Transmission electron microscope (TEM) images and particle size distributions (PSDs) of ZIF-8 crystals (A) as synthesized (micron-sized), (B) as synthesized (nano-sized), (C) PSD of as synthesized (nano-sized), (D) after R6G loading (micron-sized), (E) after R6G loading (nano-sized), and (F) PSD of after R6G loading (nano-sized). The loading was carried out with 10.3 mM R6G at 100 °C for 7 days in *n*-butanol.

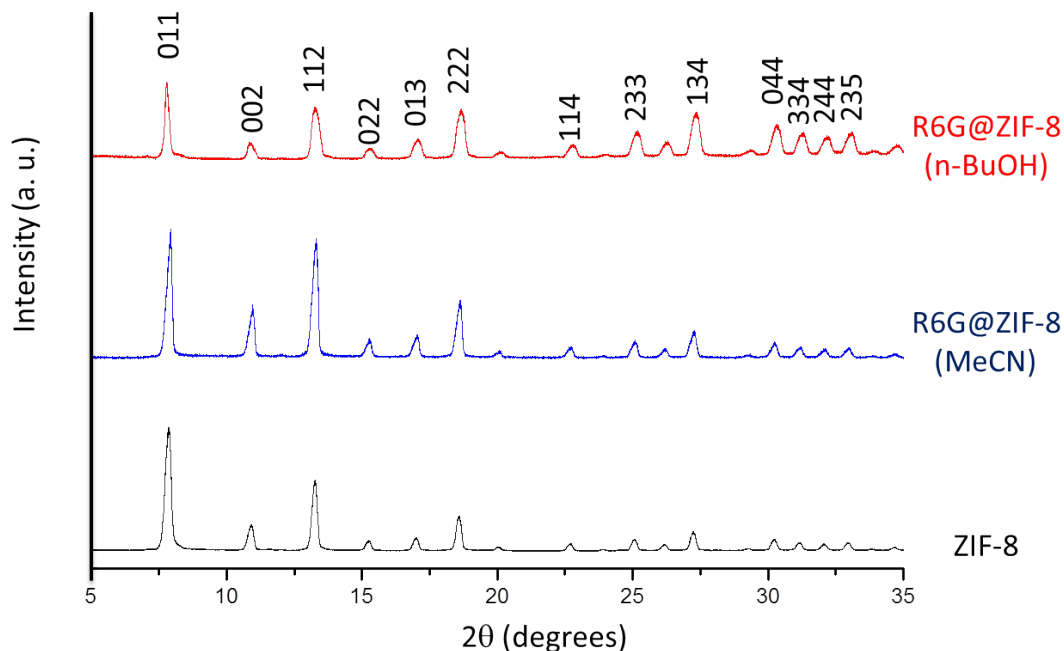


Figure 2-5. Powder X-ray diffraction patterns of R6G@ZIF-8. The R6G loading was carried out with 10.3 mM R6G at 100 °C for 7 days in *n*-butanol (red) and in MeCN (blue). The pattern for pure ZIF-8 crystals (black) is given for reference at bottom.

2.4 Evidence of encapsulation

To confirm that the R6G is indeed incorporated in ZIF-8 instead of attaching to its surface, a method to remove the surface bound R6G in all samples prior to UV-Vis analysis was sought out. The affinity of R6G for ZIF-8 likely arises from its ester and amine functional groups, which can interact with the hydrophilic external surfaces of ZIF-8. We have discovered that briefly exposing ZIF-8 to R6G at room temperature led to the coloration of the MOF, despite linker exchange not occurring to an appreciable extent (Figure 2-6). To remove surface bound R6G from ZIF-8, the samples were washed with methanolic solutions of polyvinylpyrrolidone (PVP), a polar polymer with poly-

ketone functional groups that interact strongly with MOF crystals due to the polyvalency effect.³¹ Due to its large size, PVP cannot penetrate the interior of ZIF-8. Therefore, any R6G that remains associated with ZIF-8 after PVP washing is likely trapped in the pores of ZIF-8 rather than on its surface. As expected, repeated washings of R6G@ZIF-8 with PVP led to the liberation of some R6G, but after repeated PVP washings, the pink color of R6G@ZIF-8 remained (Figure. 2-7a,b). Analysis of the PVP washed R6G@ZIF-8 by UV-Vis allowed for the encapsulation efficiency of R6G in R6G@ZIF-8 to be quantitatively determined. A similar PVP washing procedure carried out under conditions where linker exchange does not occur led to full removal of R6G from the ZIF-8 crystals (Figure 2-7c).

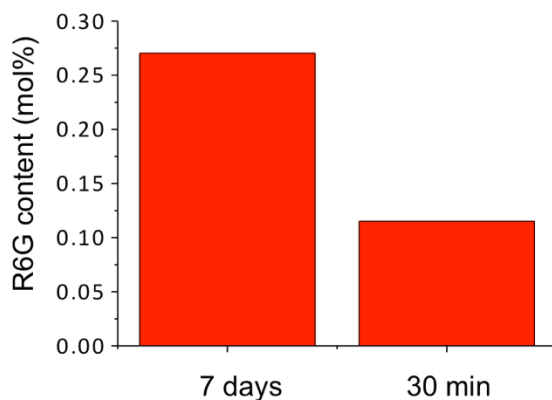


Figure 2-6. ZIF-8 surface interaction experiments. Loading of R6G for 7 days and 30 minutes. All other R6G loading parameters were the same (10.3 mM R6G, *n*-butanol, 25 °C).

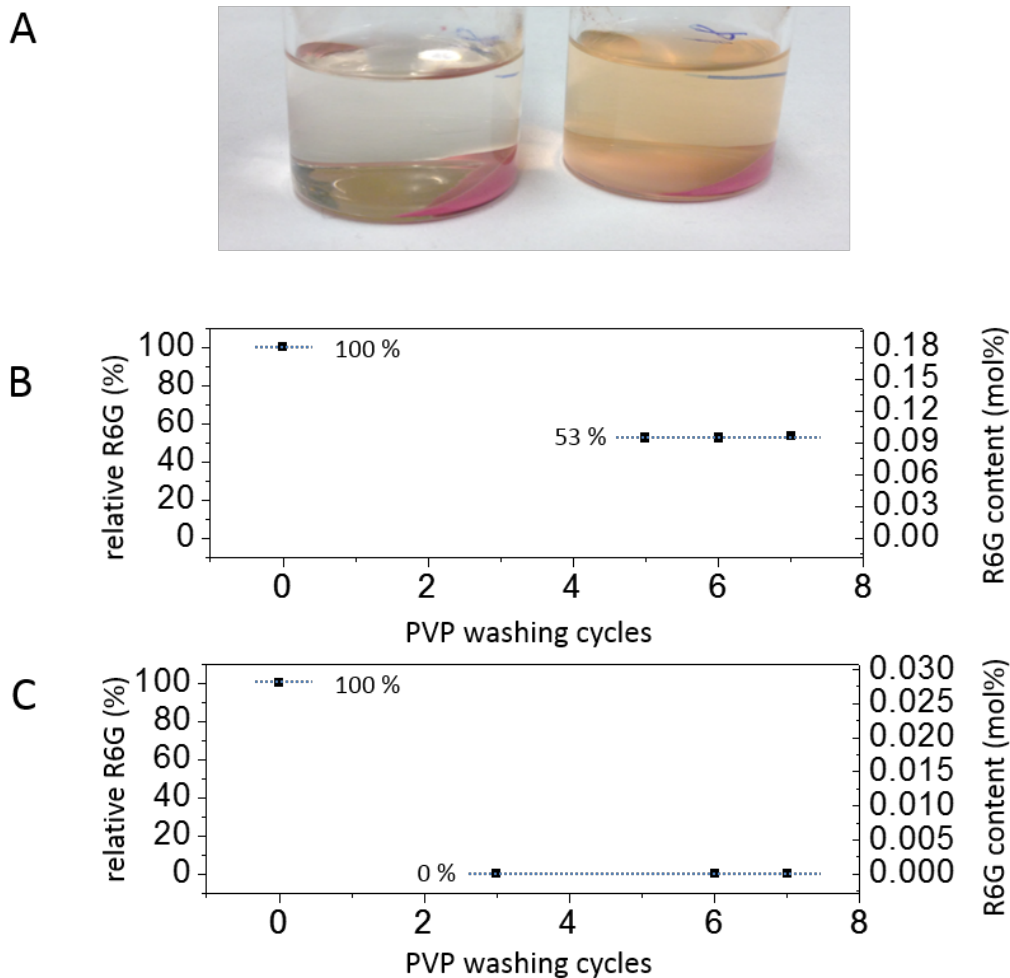


Figure 2-7. PVP washing experiments. a) Digital photograph of R6G@ZIF-8 precipitates and supernatants after centrifugation: (left) as synthesized R6G@ZIF-8 after 5 times methanol washing and (right) methanol-washed R6G@ZIF-8 after exposure to 1.4 wt. % PVP/methanol solution. Surface bound R6G was washed with PVP solution. In B) and C), R6G content tracking by absorbance after PVP washing cycles. The R6G loading was carried out with 1.29 mM R6G in *n*-butanol at (B) 100 °C for 7 days, and (C) 25 °C for 10 min.

2.5 The effect of temperature and solvent on guest encapsulation

After R6G was removed from the surface, the effects of temperature, solvent, and initial concentration of R6G on R6G encapsulation in ZIF-8 were studied (Figure 2-3). This study indicated that guest loading was temperature and solvent dependent. Higher encapsulation was observed at higher temperatures due to increased linker exchange rates. Likewise, guest loading in acetonitrile is low because linker exchange is slower in acetonitrile compared to *n*-butanol (See Chapter 3). As expected for diffusion-controlled guest incorporation, R6G loading was found to be directly proportional to the initial concentration of R6G (Figure 2-3a). Re-subjecting R6G@ZIF-8 to the linker exchange reaction conditions without exogenous R6G led to diffusion of the dye into solution (Table 2-1). Thus, the guests appear to be kinetically trapped. Importantly, leaching can be prohibited when R6G@ZIF-8 is subjected to conditions that do not promote linker exchange (Table 2-1).

Sample	Preparation	Loading (mol %)
Original R6G@ZIF-8	10.29 mM R6G, 2.2 mmol MeImH, BuOH, 100 °C, 7 d	0.370
Linker exchange conditions	2.2 mmol MeImH, BuOH, 100 °C, 7 d	0.027
Non-linker exchange condition	2.2 mmol MeImH, MeOH, 20 °C, 1 month	0.340

Table 2-1. Leaching experiments.

2.6 Fluorescence experiments to distinguish encapsulated versus surface-bound R6G

To further confirm that R6G is encapsulated in ZIF-8 during linker exchange, we have compared the fluorescence intensities of R6G@ZIF-8 (prepared by linker exchange in *n*-butanol with R6G), surface bound R6G (prepared by brief exposure of ZIF-8 to R6G), and free R6G in solution (Table 2-2). After normalization, a dramatic decrease in fluorescence intensity was observed for R6G@ZIF-8 and surface bound R6G compared to free R6G in solution. Moreover, the normalized intensity for surface bound R6G (0.10) was more than double than R6G@ZIF-8 (0.04). The origin of the lower intensity observed in R6G@ZIF-8 compared to surface bound R6G is likely due to dye encapsulation in R6G@ZIF-8, which is expected to alter light absorption and/or emission due to differing interactions between the guest molecule and the framework. Regardless of the specific rationale, the difference in fluorescence intensity observed for R6G@ZIF-8 compared to surface bound R6G provides further support that R6G is encapsulated in ZIF-8 during the linker exchange instead of bound to the external ZIF-8 surface. Picosecond time-resolved fluorescence measurements were made to determine if encapsulation in ZIF-8 had any effect on the fluorescence lifetime (τ) of R6G, however no appreciable difference was seen between the τ values of the encapsulated samples and those of the surface only control (Table 2-2).

Sample	wt. % R6G	τ (ns)	I / A (a.u.)	I / A normalized
R6G	-	2.84 ± 0.14	18800 ± 100	1.0
Surface only control	0.023	3.63 ± 0.10	1800 ± 40	0.096
R6G@ZIF-8 + MeImH	0.024	3.50 ± 0.03	790 ± 6	0.042
R6G@ZIF-8 no exog.	0.064	3.79 ± 0.02	195 ± 3	0.010

Table 2-2. Fluorescence lifetime and fluorescence intensity measurements. R6G@ZIF-8 samples prepared with 147 mM 2-methylimidazole exogenous linker (+ MeImH) and without any exogenous linker (no exog.) in *n*-butanol. Both R6G@ZIF-8 samples were PVP washed to remove surface bound dye as described in the manuscript. The “surface only control” was prepared by exposing ZIF-8 particles to R6G in a methanolic solution for 10 min, followed by extensive (5 ×) washing with methanol. In previous control experiments we found that PVP washing of a sample prepared this way led to complete removal of the dye (see figure 2-7c), demonstrating that dye loading is solely on the surface. The fluorescence intensities were normalized by the amount of the R6G loading measured by absorption after the ZIF-8 particles were digested by acid. The R6G standard consisted of R6G dissolved in methanol with a UV-Vis absorbance of 0.3.

2.7 The effect of exogenous linker concentration on dye encapsulation

In order to gain a better understanding of the guest encapsulation process, the effect that the exogenous 2-methylimidazole linker concentration had on guest loading was explored next. Somewhat surprisingly, R6G loading was inversely proportional to the concentration of exogenous linker (Figure 2-3b). In fact, the highest loading of R6G was observed when reactions were carried out without any exogenous 2-methylimidazole

linker. Although unexpected, this result could be rationalized by a dissociative linker substitution mechanism where dissociation of 2-methylimidazole from ZIF-8 led to the formation of a linker-deficient “open” state (Figure 2-1). Under low concentrations of free imidazole, the “open” state is not as readily arrested by free linker, which allows more time for the guest to diffuse into the pores of the MOF. Consequently, higher guest loadings are observed at lower concentrations of exchanging linker.

2.8 Kinetic measurements of linker exchange to test the hypothesis of a dissociative mechanism

To test the hypothesis that linker substitution is dissociative, we examined the kinetics of the linker exchange reaction under pseudo-first order conditions by varying the initial concentration of exogenous imidazole linker (for details see the experimental section). Observed rate constants (k_{obs}) for the linker exchange reaction could be obtained by using the method of initial rates (< 10 % conversion). Powder XRD indicated that the crystal structure of ZIF-8 was not perturbed under these conditions. By plotting k_{obs} versus [imidazole], we observed a linear correlation with a non-zero slope and intercept (k_{obs} vs. [ImH] in Figure 2-8, representative $^1\text{H-NMR}$ spectra in Figure 2-9, conv. vs. t plots in Figure 2-10, and k_{obs} values in Table 2-3). These data suggest that there is a competition between associative and dissociative linker substitution reactions with the slope of this line ($m = 38.6 \times 10^{-6} \text{ M}^{-1} \text{ s}^{-1}$) being the second order rate constant for associative exchange, and the intercept ($b = 3.37 \times 10^{-6} \text{ s}^{-1}$) being the first order rate constant for dissociative exchange. Under the empirically determined conditions employed for linker exchange ([imidazole] = 147 mM), the apparent rate constant for associative linker substitution ($k_{app} (\text{s}^{-1}) = k_a[\text{imidazole}]$) is $5.67 \times 10^{-6} \text{ s}^{-1}$, which is on par

with the first order rate constant for dissociative linker exchange. Importantly, under the conditions that worked best to maximize guest incorporation ($[\text{imidazole}] = 0$), the associative exchange mechanism was completely shut down. Indeed, the lower guest incorporation that we see at higher linker concentrations may be due to a competing associative exchange process that precludes the formation of an “open” state for guest incorporation.

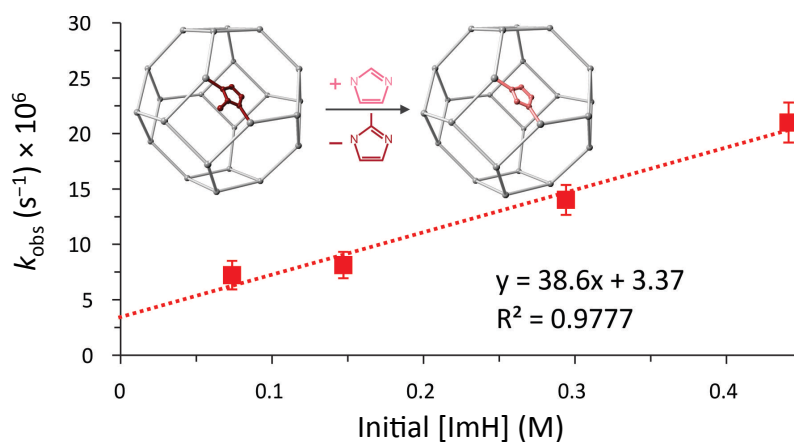


Figure 2-8. Observed rate constants (k_{obs}) for exchange of ZIF-8 with imidazole at different initial concentrations of imidazole.

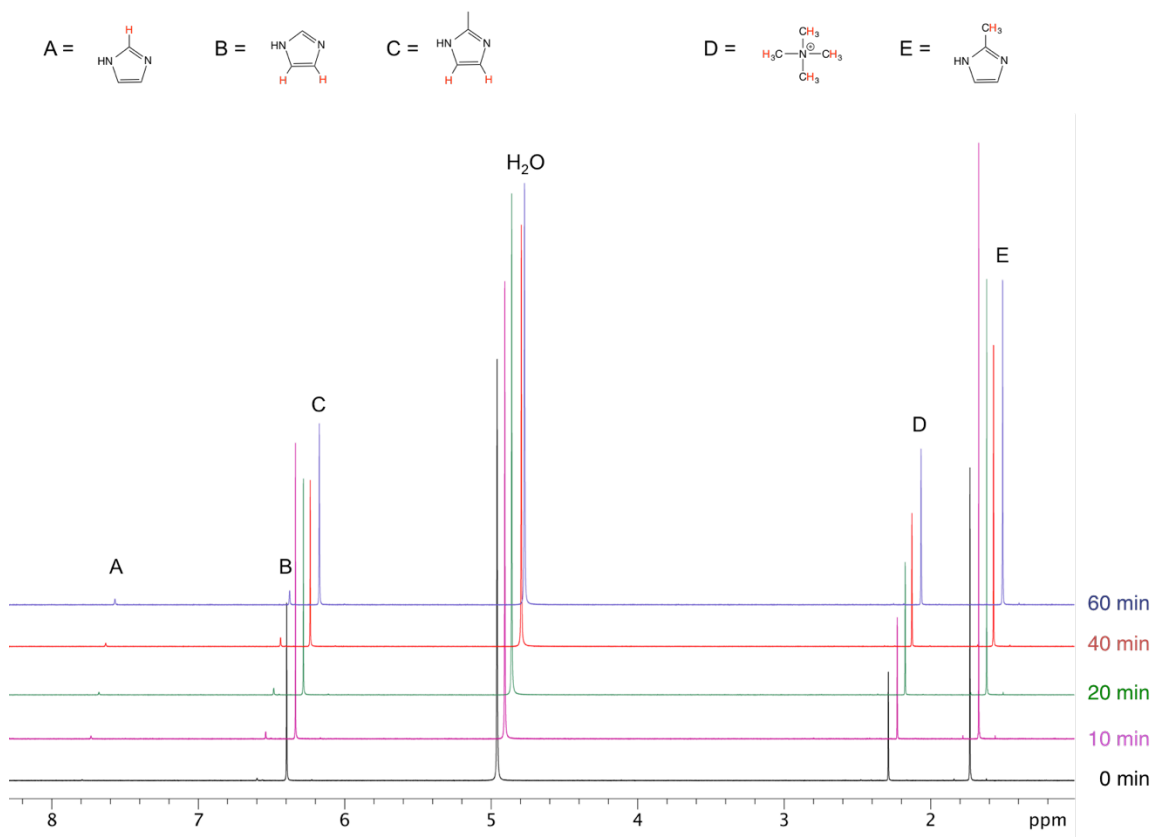


Figure 2-9. Representative $^1\text{H-NMR}$ spectra of acid-digested $\text{Zn}(\text{MeIm})_{2-x}(\text{Im})_x$ over the course of the exchange reaction for the series with $\text{im}/\text{mim} = 30$.

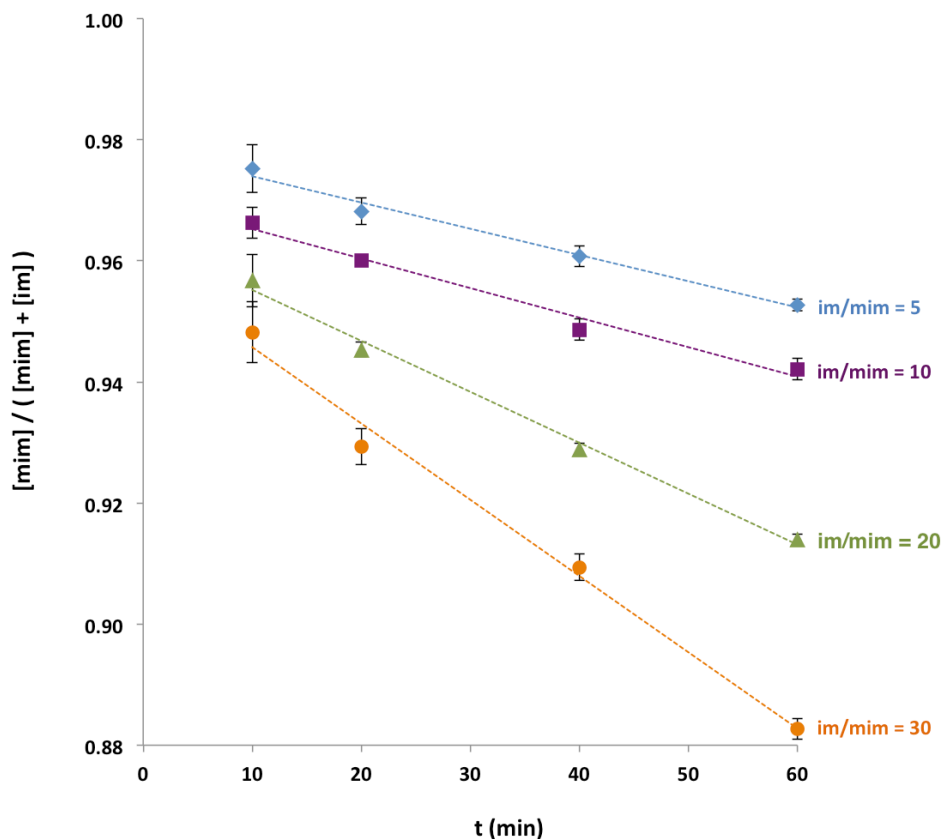


Figure 2-10. Plot of conversion vs. time of the $\text{Zn}(\text{MeIm})_2$ to $\text{Zn}(\text{MeIm})_{2-x}(\text{Im})_x$ exchange reaction at varying concentrations of imidazole, the exogenous linker, with conversion expressed as the disappearance of 2-methylimidazole from the framework as a molar fraction of the total imidazolate linker content of the solid. Least squares linear regressions are shown.

ImH/MeIm^- (mol/mol)	$[\text{ImH}]$ (M)	k_{obs} (s^{-1})	R^2
5	0.0735	$7.2 (\pm 1.3) \times 10^{-6}$	0.98622
10	0.147	$8.1 (\pm 1.2) \times 10^{-6}$	0.98121
20	0.249	$14.0 (\pm 1.3) \times 10^{-6}$	0.99413
30	0.441	$21.0 (\pm 1.8) \times 10^{-6}$	0.99036

Table 2-3. The observed rate constants (k_{obs}) determined by the method of initial rates (k_{obs} = slope m) from the conversion vs. time plots in Figure 2-10, with the coefficients of determination (R^2) for each linear fit.

2.9 Encapsulation of the ligand triphenylphosphine

Finally, to probe the generality of the methodology, encapsulation of a ligand suitable for incorporating transition metal complexes in ZIF-8 was targeted. Because it is ubiquitous in organometallic catalysis and has the appropriate molecular size (Figure 2-2), triphenylphosphine (PPh_3) (molecular diameter = 9.56 Å) was chosen as the initial guest ligand. The same method used for dye encapsulation was adopted to encapsulate PPh_3 in ZIF-8 (henceforth referred to as $\text{PPh}_3@ZIF-8$) using initial $[\text{PPh}_3]$ of 165 mM and 220 mM. Elemental analysis of the product obtained with an initial $[\text{PPh}_3]$ of 220 mM indicated a PPh_3 loading of 2 wt. % (Figure 2-11). PXRD analysis indicates that the structure of ZIF-8 was preserved during the encapsulation of PPh_3 (Figure 2-12), as was observed for R6G.

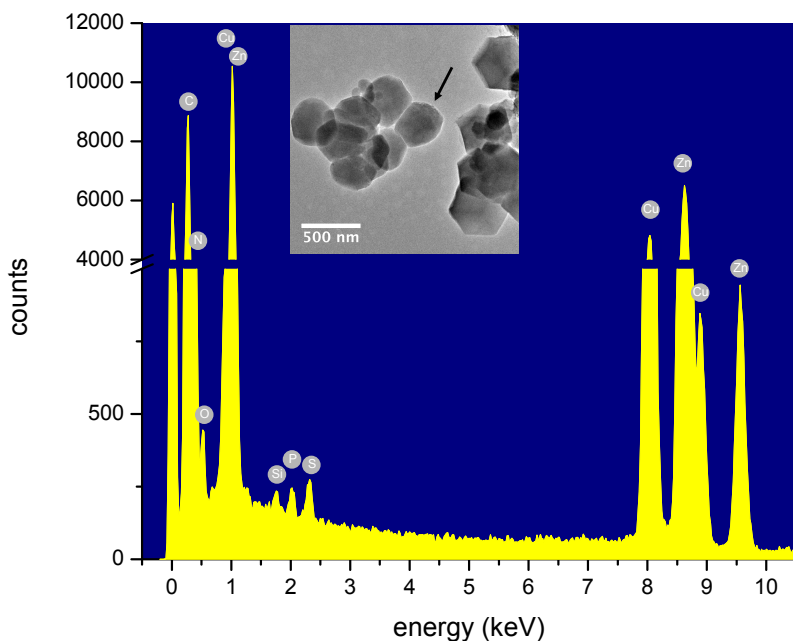


Figure 2-11. A representative energy dispersive X-ray spectrum of $\text{PPh}_3@ZIF-8$ loaded with initial $[\text{PPh}_3]$ of 220 mM. Inset shows the TEM image of the area used for analysis, with the focused particle indicated by an arrow. The 10 % pore loading of PPh_3 was estimated by

multiplying the P/Zn atomic ratio of 0.016 by 6 (the number of unique Zn atoms per sodalite cage of ZIF-8).

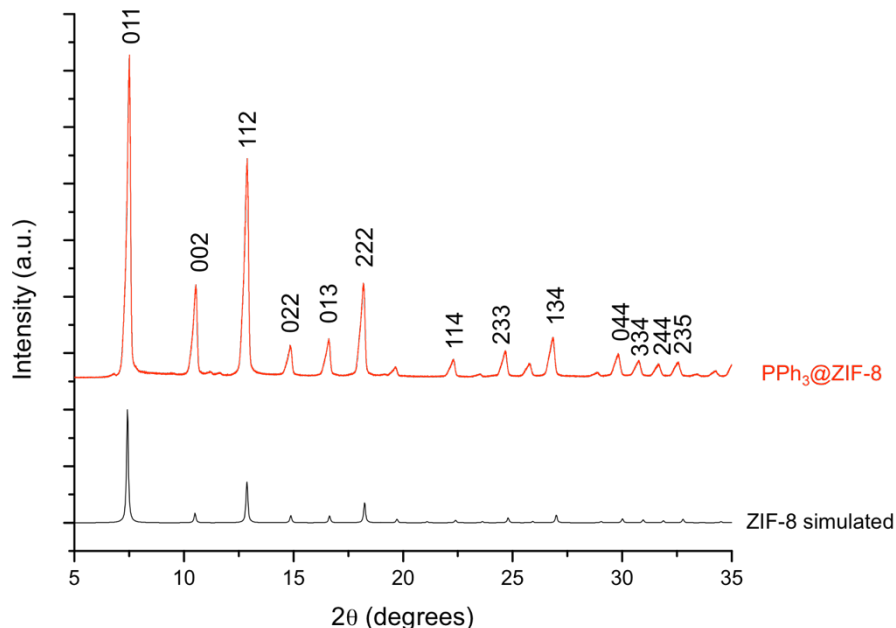


Figure 2-12. Powder X-ray diffraction patterns of $\text{PPh}_3@ZIF-8$ (top, red) and ZIF-8 simulated from the crystal structure (bottom, black) for reference. The loading was carried out with 220 mM PPh_3 in *n*-butanol for 7 days at 100 °C.

To demonstrate that the PPh_3 was mainly encapsulated within the pores of ZIF-8 and not on its external surface, N_2 adsorption data were collected at 77 K on the two loadings of $\text{PPh}_3@ZIF-8$ and the commercial source of ZIF-8 with a high resolution of points in the micropore adsorption region (Figure 2-13). Saturation of the micropore volume with N_2 occurred for the reference ZIF-8 material at 485 cm^3/g , and the BET surface area was calculated to be 1554 m^2/g using a P/P_0 range of 5×10^{-4} to 5×10^{-3} (before gating) or 1885 m^2/g with a range of 5×10^{-4} to 10^{-2} (after gating). These surface areas are in agreement with ZIF-8 values from the literature.³² For the $\text{PPh}_3@ZIF-8$

samples, micropore saturation occurred at $459 \text{ cm}^3/\text{g}$ for the sample exchanged with 165 mM PPh_3 and at $405 \text{ cm}^3/\text{g}$ for that with 220 mM PPh_3 , which is 5 % and 16 % lower compared to ZIF-8. This decrease in the micropore adsorption capacity was in excess of the decrease anticipated from the weight gain upon loading (only 2 %) and was consistent with guests occupying some pores of the MOF. From these data, we estimated that approximately one in every 10 pores in ZIF-8 was occupied by a triphenylphosphine ligand. Such loadings are only possible by the linker exchange process that facilitates incorporation of the large ligand guest.

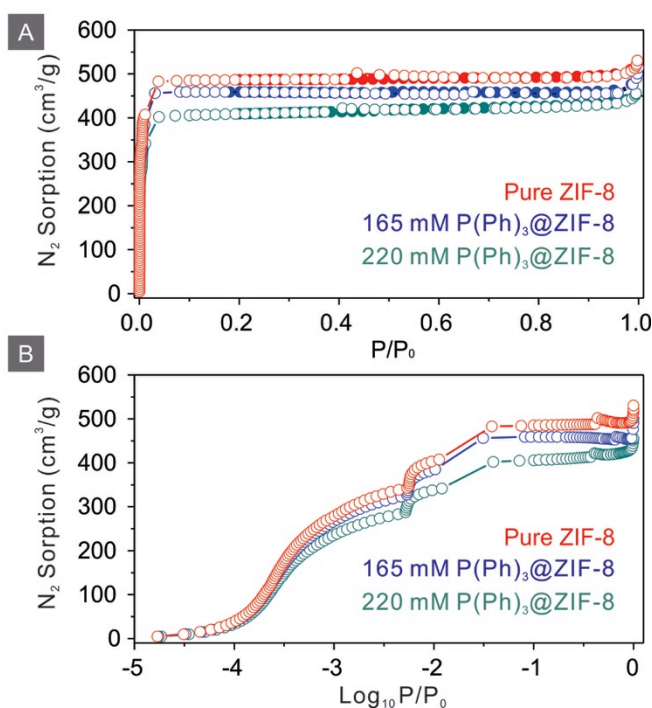


Figure 2-13. (A) N_2 absorption (filled symbols) and desorption (open symbols) isotherms of ZIF-8 (red), 165 mM triphenylphosphine@ZIF-8 (blue) and 220 mM triphenylphosphine@ZIF-8 (green). (B) Log_{10} scale of P/P_0 to show the detailed N_2 sorption under low pressure.

2.10 Conclusion

In summary, we have developed a method for the postsynthetic encapsulation of large guests (PPh₃, R6G) with molecular diameters that exceed the framework aperture size in ZIF-8 nanocrystals beyond what could be explained by framework flexibility. The approach capitalizes on the existence of linker exchange reactions, which our kinetic studies show proceed by a competition between associative and dissociative exchange mechanisms. Maximum guest encapsulation was observed under conditions where the dissociative mechanism predominates because the dissociation of at least one aperture-defining 2-methylimidazole linker facilitates the formation of a short-lived “open” state in the pore with an expanded pore aperture size. Compared to other encapsulation strategies, this approach does not require any specific electrostatic interaction between the guest and the MOF host, which may significantly expand the scope of molecular guests and MOF hosts suitable for forming host-guest composites. In addition to the impact that these findings have on the ability to incorporate large guests in MOFs, important insight into the mechanism for linker exchange processes in MOFs was garnered. Such processes have already been exploited for the synthesis of novel MOF architectures,²⁸ useful catalyst species,²⁶ and sophisticated nanocomposite materials.²⁹ Future investigations will look at the application of these findings to other classes of MOFs, as well as the utilization of the new encapsulation methodology for the development of useful catalysts that take advantage of the size-selective capabilities of MOFs.

Experimental methods

General considerations: Unless otherwise stated, all the reactions were carried out in the air without taking any precaution to protect reactions from oxygen or moisture. Zinc nitrate hexahydrate (Aldrich, 99%), 2-methylimidazole (Aldrich, 99%), imidazole (Alfa Aesar, 99%), Basolite Z1200 (ZIF-8, Aldrich, produced by BASF), *n*-butanol (Alfa Aesar, $\geq 99.4\%$), acetonitrile (Aldrich, 99.8%), Rhodamine 6G (Acros, dye content $\sim 95\%$), triphenylphosphine (Aldrich), sodium hydroxide (VWR), polyvinylpyrrolidone (PVP, $M_w \sim 29,000$, Aldrich), deuterium oxide (Aldrich, 99.9 atom % D), and sulfuric acid- d_2 solution (96-98 wt. % in D_2O , 99.5 atom % D) were purchased from the indicated sources and used without further purification.

Characterization: Transmission electron microscope (TEM) images were obtained on JEOL JEM2010F operated at 200 kV. The powder x-ray diffraction patterns (PXRD) were collected on a Bruker AXS diffractometer with Cu $K\alpha$ radiation ($\lambda = 1.5418 \text{ \AA}$). 1H NMR spectra obtained for the kinetic experiments were recorded on a Varian (Agilent) (600 MHz) spectrometer. The line listing for the NMR spectra are reported as chemical shift in ppm. The nitrogen gas adsorption-desorption was carried out on Micromeritics ASAP 2020 provided by the University of Massachusetts Boston. Visible light absorption spectra were measured on a Thermo Scientific NanoDrop 2000c.

Dye loading via linker exchange: Variable amounts (9.3 mg/0.02 mmol, 29.2 mg/0.06 mmol, 73.9 mg/0.15 mmol, and 292.4 mg/0.61 mmol) of Rhodamine 6G (R6G) were placed in a 20 mL glass scintillation vial. 2-methylimidazole (MeImH) (181 mg, 2.2 mmol) and activated ZIF-8 crystals (75 mg, 0.33 mmol $Zn(MeIm)_2$) were added to the vial with the guest molecules. Next, *n*-butanol or acetonitrile (15 mL) was added to the

vial, and the solids were suspended by sonication for 10 minutes. The vial was capped and placed in an isothermal oven at 100 °C for 7 d. The guest-loaded ZIF-8 was collected by centrifugation at 5000 rpm for 10 minutes. The solid precipitate was triturated by decanting the methanol supernatant then re-suspended into fresh methanol (10 mL). The centrifugation and trituration steps were repeated at least 5 times until the supernatant was completely transparent. The residual solvent was removed from the isolated solids in a vacuum oven at 100 °C overnight. The mass recovery of the product was 92%.

Photophysical measurement: To measure the fluorescence lifetimes (τ) of the dye loaded ZIF-8 samples, we used picosecond time-resolved fluorescence spectroscopy performed on a custom system centered around a Coherent Libra HE Ti: Sapphire Amplifier System.³³ Samples were pumped with 450 nm monochromatic light and recorded by a streak camera at 550 nm with a long-pass filter cutting off wavelengths below 480 nm to eliminate the strong scattering peak caused by the solid particles. The amount of solid was held constant at 15 mg, which was dispersed into 3 mL of methanol. In the fluorescence intensity measurement, we used the ratio of the fluorescence emission intensity to the UV-Vis absorbance (I/A) to establish normalized intensity. Steady state emission spectra were recorded using an Agilent Cary Eclipse spectrophotometer with a Xe flash lamp. Acquisition parameters were held constant for all samples, which necessitated diluting the free R6G in methanol solution used for UV-Vis by a factor of 26 for the fluorescence measurement, due to its vastly higher I/A values.

PPh₃ loading via linker exchange: Variable amounts of PPh₃ (866 mg/3.3 mmol and 649 mg/2.5 mmol) were placed in a 20 mL scintillation vial. 2-methylimidazole (181 mg, 2.2 mmol) and activated ZIF-8 crystals (75 mg, 0.33 mmol Zn(MeIm)₂) were added to the

vial with the guest molecules. Next, *n*-butanol (15 mL) that had been sparged with Ar gas for 30 min to remove dissolved O₂ was added to the vial. The vial was capped and the solids were suspended by sonication for 10 minutes. The vial was placed in an isothermal oven at 100 °C for 7 days. The guest-loaded ZIF-8 was collected by centrifugation at 5000 rpm for 10 minutes. The solid precipitate was triturated by decanting the methanol supernatant then re-suspended into fresh methanol (10 mL). The centrifugation and trituration steps were repeated at least 5 times. The residual solvent was removed from the isolated solids in a vacuum oven at 100 °C overnight. The mass recovery of the product was 92%.

Leaching experiment: The dried R6G@ZIF-8 (15 mg) and 2-methylimidazole (36.2 mg, 0.44 mmol) were placed in a 5 mL scintillation vial. *n*-butanol (3 mL) was added to the vial and the solids were suspended by sonication for 10 minutes. The vial was capped and placed in an isothermal oven at 100 °C for 7 days. The product was collected by centrifugation at 5000 rpm for 10 minutes. The residual solvent was removed from the isolated solids in a vacuum oven at 100 °C overnight. The guest leaching experiment in methanol was carried out at the same condition in *n*-butanol except 20 °C for 1 month.

The effect of exogenous linker concentration: R6G (73.9 mg, 0.15 mmol) and activated ZIF-8 crystals (75 mg, 0.33 mmol Zn(MeIm)₂) were placed in a 20 mL scintillation vial. Variable amounts (0 mg, 60.3 mg/0.73 mmol, 120.6 mg/1.47 mmol, 181.0 mg/2.21 mmol, and 482.4 mg/5.88 mmol) of 2-methylimidazole were added to the vial with the guest and ZIF-8 mixture. Next, *n*-butanol (15 mL) was added to the vial, and the solids were suspended by sonication for 10 minutes. The vial was capped and placed in an isothermal oven at 100 °C for 7 days. The guest-loaded ZIF-8 was collected by

centrifugation at 5000 rpm for 10 minutes. The solid precipitate was triturated by decanting the methanol supernatant then re-suspended into fresh methanol (10 mL). The centrifugation and trituration steps were repeated at least 5 times until the supernatant was completely transparent. The residual solvent was removed from the isolated solids in a vacuum oven at 100 °C overnight.

Synthesis of micron-sized ZIF-8: The synthesis of micron-sized ZIF-8 followed a published procedure.³¹ A 25 mM solution of $\text{Zn}(\text{NO}_3)_2 \cdot 6\text{H}_2\text{O}$ in methanol (0.125 mmol, 5 mL) was combined with a 25 mM solution of 2-methylimidazole (0.125 mmol, 5 mL) in a 20 mL scintillation vial. The reaction was carried out at room temperature for 24 hours without stirring. The product was collected by centrifugation at 5000 rpm for 10 minutes. The solid precipitate was triturated by decanting the methanol supernatant then re-suspended with fresh methanol (10 mL). The centrifuging and trituration steps were repeated 3 times. The residual solvent was removed from the isolated solids in a vacuum oven at 100 °C overnight. The yield of ZIF-8 was 8.4%.

Synthesis of nano-sized ZIF-8: The synthesis of nano-sized ZIF-8 is based on a previous procedure with some modifications.³⁴ $\text{Zn}(\text{NO}_3)_2 \cdot 6\text{H}_2\text{O}$ (150 mg, 0.504 mmol) and 2-methylimidazole (330 mg, 4.02 mmol) were weighed and transferred to a 30 mL glass jar and 20 mL scintillation vial, respectively. The solids were dissolved in methanol (7.15 mL each). The glass jar was then equipped with a magnetic stir bar, and placed on a stir plate. Next, under vigorous stirring, the 2-methylimidazole solution was poured into the jar and the mixture was stirred at room temperature for 6 hours. The product was collected by centrifugation at 7000 rpm for 10 minutes. The solid precipitate was triturated by decanting the methanol supernatant then re-suspended with fresh methanol

(10 mL). The centrifuging and trituration steps were repeated 3 times. The residual solvent was removed from the isolated solids in a vacuum oven at 100 °C overnight. The yield of ZIF-8 was 83%.

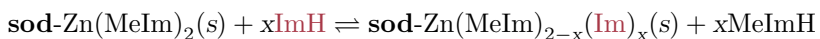
Visible light absorption spectroscopy: Dried R6G@ZIF-8 (10 mg) was digested in a 1 wt. % hydrochloric acid/methanol solution (2 mL). After stirring for 1 min, the resulting solution was transferred to a glass cuvette to measure the visible light absorption spectrum at 530 nm on a Thermo Scientific NanoDrop 2000c. The amount of R6G loading was determined by calibration curve between absorbance of light at 530 nm and R6G concentration ($\epsilon = 0.0934 \mu\text{M}^{-1}\text{cm}^{-1}$ at 530 nm).

PVP washing: Dried R6G@ZIF-8 (15 mg) was suspended in a 1.4 wt. % PVP/methanol solution (10 mL) by sonication for 10 min. The solid precipitate was collected by trituration after centrifugation at 5000 rpm for 10 min. The isolated solid was then re-suspended with fresh 1.4 wt. % PVP/methanol (10 mL), and the centrifugation and trituration steps were repeated at least 5 times until R6G content was constant as determined by UV-Vis absorption spectroscopy. The PVP-washed product was then re-suspended with 10 mL methanol to remove any excess PVP, and the final product was collected by centrifugation at 5000 rpm for 10 minutes and decanting of the supernatant. The solid was then dried overnight in vacuum oven at 100 °C to remove any residual solvent. The mass recovery was 66 %.

Molecular size calculations: The molecular sizes of R6G and triphenylphosphine were estimated by using the Spartan 10 software package to minimize structures using the Hartree-Fock method with the basis set 3-21G. The greatest interatomic distances for each molecule are given as the effective molecular sizes in Figure 2-2.

Linker exchange kinetics:

The kinetics of exchange of Zn(MeIm)₂ (ZIF-8) with exogenous imidazole (ImH) to yield Zn(MeIm)_{2-x}(Im)_x (SALEM-2) were followed using a modified procedure based on literature precedence.¹⁷ Due to the heterogeneous nature of the exchange reaction, accurate sampling could not be guaranteed, and thus, for the kinetics experiment, each point shown in Figure 2-10 is the result of independent measurements carried out at different reaction times. Generally, each reaction was repeated three times, the average of which is used for the kinetic fits.



Dried ZIF-8 (5.0 mg, 0.022 mmol Zn(MeIm)₂) was placed in a 3 mL glass serum vial. Solids were suspended by sonication in an appropriate volume of *n*-butanol (tabulated below) before the reaction was initiated with exogenous linker. A 588 mM solution of imidazole in *n*-butanol was added in an appropriate volume (see table below), and vials were immediately sealed with PTFE-lined aluminum crimp caps, shaken manually for 5 s, and placed into the aluminum heating blocks of a Labmate synthesizer thermostated at 70 °C. The reactions were incubated at 70 °C with 450 rpm shaking for a predetermined amount of time, as indicated in Figure 2-10.

im/mim (mol/mol)	5	10	20	30
Vol. <i>n</i> -butanol (mL)	2.625	2.250	1.500	0.750
Vol. 588 mM ImH (mL)	0.375	0.750	1.500	2.250

At the end of the allocated time, the vials were removed and immediately immersed in a water bath held at 0 °C. Suspended solids were transferred quickly into 3 mL of methanol chilled at 0 °C in a 15 mL centrifuge tube and centrifuged at 3300 rpm for 5 min. The solid precipitate was triturated by decanting the supernatant, and the product was re-suspended in fresh methanol (6 mL). The centrifugation and trituration was repeated 3 times with 6 mL of methanol each time. The isolated solids were transferred to pre-weighed glass vials and the residual solvent was removed in a vacuum oven at 100 °C overnight. Dried samples were weighed and then digested in a solution of 0.900 mL deuterium oxide and 0.100 mL 98% d_2 -sulfuric acid in D_2O along with tetramethylammonium bromide (0.7 mg) that was used as an internal standard for analysis by 1H -NMR spectroscopy.

The spin-lattice relaxation times (T_1) of each proton in solution were determined by the inversion recovery method and are detailed in Table 2-4. In light of the measured relaxation times 1H -NMR spectra were acquired using an acquisition time (at) of 18 s and an interpulse delay (d1) of 54 s, in order to make (at + d1) $\sim 5 \times$ the longest T_1 . A pulse angle of 90 ° was used and 16 transients were taken per acquisition.

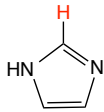
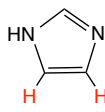
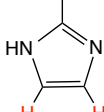
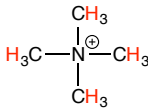
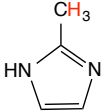
proton (in red)				HDO		
δ (ppm)	7.85	6.66	6.45	4.94	2.35	1.79
T_1 (s)	13.74 ± 0.28	12.06 ± 0.21	9.72 ± 0.26	3.01 ± 0.11	5.65 ± 0.12	4.44 ± 0.32

Table 2-4. The spin-lattice relaxation times (T_1) determined for each proton in the acid-digested solutions of the $Zn(MeIm)_{2-x}(Im)_x$ products, which were used to choose the 1H -NMR acquisition parameters.

The quantity of imidazole and 2-methylimidazole in solution were determined using the formulae:

A_P = area determined by integration of peak (P), as defined in Figure 2-9

$$\left(A_A \times \frac{[\text{TMA}^+]}{A_D} \times \frac{12 \text{ protons}}{1 \text{ protons}} \right) + \left(A_B \times \frac{[\text{TMA}^+]}{A_D} \times \frac{12 \text{ protons}}{2 \text{ protons}} \right) = 2[\text{im}]$$

$$\left(A_C \times \frac{[\text{TMA}^+]}{A_D} \times \frac{12 \text{ protons}}{2 \text{ protons}} \right) + \left(A_E \times \frac{[\text{TMA}^+]}{A_D} \times \frac{12 \text{ protons}}{3 \text{ protons}} \right) = 2[\text{mim}]$$

$$\frac{[\text{mim}]}{[\text{im}] + [\text{mim}]} = \text{conversion}$$

From the ¹H-NMR data, plots of conversion versus time could be made at each concentration, using the average deviation to estimate error (Figure 2-10). To obtain the observed rate constants (k_{obs}) used in Figure 2-8, linear regression analysis of the data collected at time points from 10 minutes to 60 minutes was carried out, with the slope m being k_{obs} . Values of k_{obs} and the accompanying R² values for the linear fits are outlined in Table 2-3. In order to estimate the error in the k_{obs} values that we obtained from the conversion vs. time plots in Figure 2-10, we considered two outlying cases, both high and low, using the bound limits (from average deviation) of the conversion values at 10 and 60 min. For the high estimate of k_{obs} , we obtain a linear regression of a four-point plot of (1) the upper bound for the 10 min point, (2) the average value for the 20 min point, (3) the average value for the 40 min point, and (4) the lower bound for the 60 min point. For the low estimate, we use the low bound for the 10 min point, the upper bound for the 60 min point, keeping the other two points the same.

References

- (1) Horcajada, P.; Chalati, T.; Serre, C.; Gillet, B.; Sebrie, C.; Baati, T.; Eubank, J. F.; Heurtaux, D.; Clayette, P.; Kreuz, C.; Chang, J.-S.; Hwang, Y. K.; Marsaud, V.; Bories, P.-N.; Cynober, L.; Gil, S.; Ferey, G.; Couvreur, P.; Gref, R. Porous metal–organic–framework nanoscale carriers as a potential platform for drug delivery and imaging. *Nat. Mater.* **2010**, *9*, 172–178.
- (2) Rimoli, M. G.; Rabaioli, M. R.; Melisi, D.; Curcio, A.; Mondello, S.; Mirabelli, R.; Abignente, E. Synthetic zeolites as a new tool for drug delivery. *J. Biomed. Mater. Res. A* **2008**, *87A*, 156–164.
- (3) Yanai, N.; Kitayama, K.; Hijikata, Y.; Sato, H.; Matsuda, R.; Kubota, Y.; Takata, M.; Mizuno, M.; Uemura, T.; Kitagawa, S. Gas detection by structural variations of fluorescent guest molecules in a flexible porous coordination polymer. *Nat. Mater.* **2011**, *10*, 787–793.
- (4) McGilvray, K. L.; Chretien, M. N.; Lukeman, M.; Scaiano, J. C. A simple and smart oxygen sensor based on the intrazeolite reactions of a substituted anthraquinone. *Chem. Commun.* **2006**, 4401–4403.
- (5) Talin, A. A.; Centrone, A.; Ford, A. C.; Foster, M. E.; Stavila, V.; Haney, P.; Kinney, R. A.; Szalai, V.; El Gabaly, F.; Yoon, H. P.; Leonard, F.; Allendorf, M. D. Tunable electrical conductivity in metal-organic framework thin-film devices. *Science* **2014**, *343*, 66–69.
- (6) Cardin, D. J. Encapsulated Conducting Polymers. *Adv. Mater.* **2002**, *14*, 553–563.

- (7) Müller, M.; Devaux, A.; Yang, C. H.; De Cola, L.; Fischer, R. A. Highly emissive metal–organic framework composites by host–guest chemistry. *Photochem. Photobiol. Sci.* **2010**, *9*, 846–853.
- (8) Calzaferri, G.; Huber, S.; Maas, H.; Minkowski, C. Host-guest antenna materials. *Angew. Chem. Int. Ed.* **2003**, *42*, 3732–3758.
- (9) Martínez-Martínez, V.; Furukawa, S.; Takashima, Y.; López Arbeloa, I.; Kitagawa, S. Charge Transfer and Exciplex Emissions from a Naphthalenediimide- Entangled Coordination Framework Accommodating Various Aromatic Guests. *J. Phys. Chem. C* **2012**, *116*, 26084–26090.
- (10) Wang, J. L.; Wang, C.; Lin, W. B. Metal–Organic Frameworks for Light Harvesting and Photocatalysis. *ACS Catalysis* **2012**, *2*, 2630–2640.
- (11) Son, H. J.; Jin, S. Y.; Patwardhan, S.; Wezenberg, S. J.; Jeong, N. C.; So, M.; Wilmer, C. E.; Sarjeant, A. A.; Schatz, G. C.; Snurr, R. Q.; Farha, O. K.; Wiederrecht, G. P.; Hupp, J. T. Light-Harvesting and Ultrafast Energy Migration in Porphyrin-Based Metal–Organic Frameworks. *J. Am. Chem. Soc.* **2013**, *135*, 862–869.
- (12) Dutta, P. K.; Severance, M. Photoelectron Transfer in Zeolite Cages and Its Relevance to Solar Energy Conversion *J. Phys. Chem. Lett.* **2011**, *2*, 467–476.
- (13) Corma, A.; Garcia, H. Supramolecular Host-Guest Systems in Zeolites Prepared by Ship-in-a-Bottle Synthesis. *Eur. J. Inorg. Chem.* **2004**, *2004*, 1143–1164.
- (14) Fletcher, A. J.; Thomas, K. M.; Rosseinsky, M. J. Flexibility in metal-organic framework materials: Impact on sorption properties. *J. Solid State Chem.* **2005**, *178*, 2491–2510.

- (15) Costa, J. S.; Gamez, P.; Black, C. A.; Roubeau, O.; Teat, S. J.; Reedijk, J. Chemical Modification of a Bridging Ligand Inside a Metal–Organic Framework while Maintaining the 3D Structure. *Eur. J. Inorg. Chem.* **2008**, 1551–1554.
- (16) Kim, M.; Cahill, J. F.; Fei, H.; Prather, K. A.; Cohen, S. M. Postsynthetic Ligand and Cation Exchange in Robust Metal–Organic Frameworks. *J. Am. Chem. Soc.* **2012**, *134*, 18082–18088.
- (17) Karagiari, O.; Lalonde, M. B.; Bury, W.; Sarjeant, A. A.; Farha, O. K.; Hupp, J. T. Opening ZIF-8: A Catalytically Active Zeolitic Imidazolate Framework of Sodalite Topology with Unsubstituted Linkers. *J. Am. Chem. Soc.* **2012**, *134*, 18790–18796.
- (18) Li, B.; Zhang, Y.; Ma, D.; Ma, T.; Shi, Z.; Ma, S. Metal-Cation-Directed de Novo Assembly of a Functionalized Guest Molecule in the Nanospace of a Metal–Organic Framework. *J. Am. Chem. Soc.* **2014**, *136*, 1202–1205.
- (19) Alkordi, M. H.; Liu, Y.; Larsen, R. W.; Eubank, J. F.; Eddaoudi, M. Zeolite-like metal-organic frameworks as platforms for applications: on metalloporphyrin-based catalysts. *J. Am. Chem. Soc.* **2008**, *130*, 12639–12641.
- (20) Larsen, R. W.; Wojtas, L. Photoinduced inter-cavity electron transfer between Ru(II)tris(2,2'-bipyridine) and Co(II)tris(2,2'-bipyridine) Co-encapsulated within a Zn(II)-trimesic acid metal organic framework. *J. Mater. Chem. A* **2013**, *1*, 14133–14139.
- (21) Lee, J.; Farha, O. K.; Roberts, J.; Scheidt, K. A.; Nguyen, S. T.; Hupp, J. T. Metal-organic framework materials as catalysts. *Chem. Soc. Rev.* **2009**, *38*, 1450–1459.
- (22) Zhuang, J.; Kuo, C.-H.; Chou, L.-Y.; Liu, D.-Y.; Weerapana, E.; Tsung, C.-K. Optimized Metal–Organic-Framework Nanospheres for Drug Delivery: Evaluation of Small-Molecule Encapsulation. *ACS Nano* **2014**, *8*, 2812–2819.

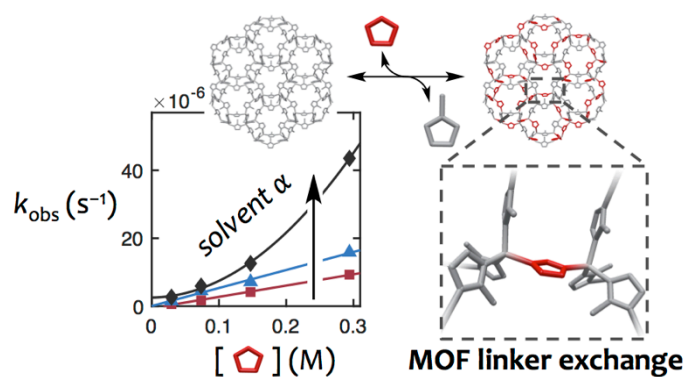
- (23) Fei, H.; Cahill, J. F.; Prather, K. A.; Cohen, S. M. Tandem Postsynthetic Metal Ion and Ligand Exchange in Zeolitic Imidazolate Frameworks. *Inorg. Chem.* **2013**, *52*, 4011–4016.
- (24) Karagiari, O.; Bury, W.; Sarjeant, A. A.; Stern, C. L.; Farha, O. K.; Hupp, J. T. Synthesis and characterization of isostructural cadmium zeolitic imidazolate frameworks via solvent-assisted linker exchange. *Chem. Sci.* **2012**, *3*, 3256–3260.
- (25) Kim, M.; Cahill, J. F.; Su, Y.; Prather, K. A.; Cohen, S. M. Postsynthetic ligand exchange as a route to functionalization of ‘inert’ metal–organic frameworks. *Chem. Sci.* **2012**, *3*, 126–130.
- (26) Pullen, S.; Fei, H.; Orthaber, A.; Cohen, S. M.; Ott, S. Enhanced Photochemical Hydrogen Production by a Molecular Diiron Catalyst Incorporated into a Metal–Organic Framework. *J. Am. Chem. Soc.* **2013**, *135*, 16997–17003.
- (27) Deria, P.; Mondloch, J. E.; Tylianakis, E.; Ghosh, P.; Bury, W.; Snurr, R. Q.; Hupp, J. T.; Farha, O. K. Perfluoroalkane Functionalization of NU-1000 via Solvent-Assisted Ligand Incorporation: Synthesis and CO₂ Adsorption Studies. *J. Am. Chem. Soc.* **2013**, *135*, 16801–16804.
- (28) Burnett, B. J.; Barron, P. M.; Hu, C.; Choe, W. Stepwise Synthesis of Metal–Organic Frameworks: Replacement of Structural Organic Linkers. *J. Am. Chem. Soc.* **2011**, *133*, 9984–9987.
- (29) Takaishi, S.; DeMarco, E. J.; Pellin, M. J.; Farha, O. K.; Hupp, J. T. Solvent-assisted linker exchange (SALE) and post-assembly metallation in porphyrinic metal–organic framework materials. *Chem. Sci.* **2013**, *4*, 1509–1513.

- (30) Bury, W.; Fairen-Jimenez, D.; Lalonde, M. B.; Snurr, R. Q.; Farha, O. K.; Hupp, J. T. Control over Catenation in Pillared Paddlewheel Metal–Organic Framework Materials via Solvent-Assisted Linker Exchange. *Chem. Mater.* **2013**, *25*, 739–744.
- (31) Lu, G.; Li, S.; Guo, Z.; Farha, O. K.; Hauser, B. G.; Qi, X.; Wang, Y.; Wang, X.; Han, S.; Liu, X.; DuChene, J. S.; Zhang, H.; Zhang, Q.; Chen, X.; Ma, J.; Loo, S. C. J.; Wei, W. D.; Yang, Y.; Hupp, J. T.; Huo, F. Imparting functionality to a metal–organic framework material by controlled nanoparticle encapsulation. *Nat. Chem.* **2012**, *4*, 310–316.
- (32) Park, K. S.; Ni, Z.; Côté, A. P.; Choi, J. Y.; Huang, R. D.; Uribe-Romo, F. J.; Chae, H. K.; O’Keeffe, M.; Yaghi, O. M. Exceptional chemical and thermal stability of zeolitic imidazolate frameworks. *PNAS* **2006**, *103*, 10186–10191.
- (33) Powers, D. C.; Anderson, B. L.; Nocera, D. G. Two-Electron HCl to H₂ Photocycle Promoted by Ni(II) Polypyridyl Halide Complexes. *J. Am. Chem. Soc.* **2013**, *135*, 18876–18883.
- (34) Venna, S. R.; Jasinski, J. B.; Carreon, M. A. Structural Evolution of Zeolitic Imidazolate Framework-8. *J. Am. Chem. Soc.* **2010**, *132*, 18030–18033.

3.0 CHAPTER 3

Understanding the Solvent-Dependence of MOF Linker Exchange

Kinetics in the Reaction of ZIF-8 with Imidazole



A significant portion of the work described in this chapter will be published in:

Morabito, J. V.; Li, Z.; Byers, J. A.; Tsung, C.-K. On the Solvent-Dependence of MOF Linker Exchange Kinetics in the Reaction of ZIF-8 with Imidazole. In preparation.

3.1 Introduction

Exchange reactions have enabled a new level of control in the rational, stepwise preparation of metal-organic framework (MOF) materials.^{1,2} However, their full potential is limited by a lack of understanding of the molecular mechanisms by which they occur. MOFs are a class of coordination network solids³ with applications across a variety of technologies,⁴ including molecular separation and storage,⁵ catalysis,⁶ and drug delivery.⁷ For a MOF to be stable and self-assemble with minimal defects, it must possess thermodynamically favorable metal-ligand bonds⁸ that are also kinetically reversible.⁹⁻¹³ The kinetic reversibility (i.e., substitutional lability) of the metal-ligand bonds—a prerequisite for self-assembly of the molecular precursors into frameworks with long-range order—can also be exploited after synthesis (Figure 3-1). Following the initial assembly of a MOF, the bound components (organic linkers and metal ions) of the framework can be replaced by free components from solution in a stepwise manner without dissolution of the solid.^{1,2,14} These solid-liquid exchange reactions¹⁵ (eq. (3-1)) ultimately yield a crystal identical to the starting one, except for the swapped components.



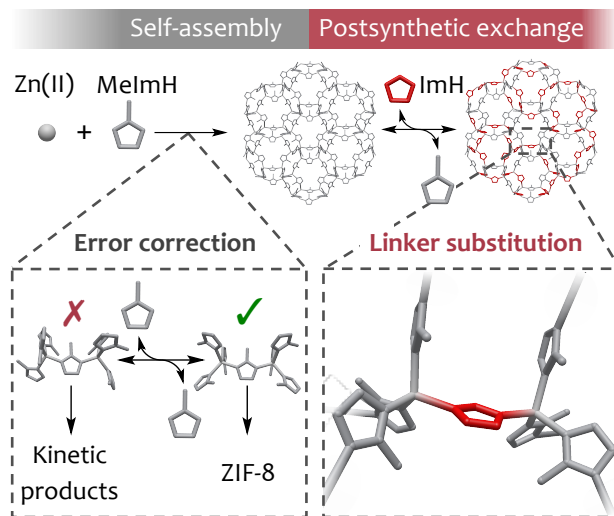


Figure 3-1. The important roles of MOF metal-ligand bond reversibility in two contexts: (1) during synthesis, correcting errors in connectivity that occur in the course of MOF self-assembly, and (2) after synthesis, introducing new function through substitution reactions.

These postsynthetic exchange reactions have become a powerful tool for MOF synthesis, as they have enabled researchers to introduce new functionality,¹⁶ access novel MOF structures,¹⁷ generate chemical robustness,^{16l-m} and encapsulate guest molecules.¹⁸⁻²⁰ While examples that demonstrate the power of exchange reactions for MOF synthesis continue to amass, remarkably little attention has been paid to the molecular mechanisms of substitution. This oversight is especially surprising as a vast body of knowledge exists around the substitution mechanisms of simpler complexes,²¹ which are fundamentally important to many areas of chemistry.^{10,22-32} This knowledge about complexes, which has been accumulated over many years through careful measurements of reaction kinetics under controlled conditions, has informed everything from the synthesis of new complexes²³ to understanding the function of metalloenzymes.²⁵ We anticipate that similar gains could come out of mechanistic study of MOF exchange reactions. Such

gains would not only advance the development of rational, stepwise approaches to MOF synthesis, but would also deepen our understanding of the related reactions involved in MOF self-assembly³³ and may lead to future applications.³⁴ For our contribution, we have chosen to undertake the mechanistic study of organic linker exchange in MOFs, which will complement the burgeoning mechanistic work on metal ion exchange.³⁵

Burnett et al. were the first to demonstrate the utility of linker exchange reactions for stepwise MOF synthesis through their exchange of the dipyrridyl linkers in a MOF containing $\text{Zn}_2(\text{COO})_4$ paddlewheel nodes.^{17a} Subsequent work¹⁶⁻²⁰ demonstrated that linker exchange occurs in a broad array of MOFs, regardless of the type of metal nodes and organic linkers. Researchers have even observed linker exchange in MOFs previously considered particularly robust^{16c-d} or kinetically inert.^{16h,17e} Despite the widespread use and synthetic utility of MOF linker exchange, little is known about the substitution mechanism(s).^{1,36} Hupp, Farha, and co-workers uncovered that linker exchange in many MOFs is highly dependent on the solvent,^{16a-b} leading these researchers to term the process *solvent-assisted linker exchange* (SALE).^{14d,16a} Likewise, Cohen and co-workers observed similar effects in UiO-66, which is based on completely different metal nodes and organic linkers than ZIF-8.^{16c} The solvent effects observed in these reports and others^{16u,16w} led us to identify the solvent-dependence of MOF linker exchange kinetics as a particularly important mechanistic aspect to investigate. Although several studies have focused on some aspects of the reaction mechanism,^{16a,16c,16d,16g,16m,16n,17c} none involved quantitative measurements of substitution rates, from which the kinetic rate law can be deduced.

We therefore set out to develop a systematic protocol for the mechanistic study of MOF linker exchange that featured quantitative measurements of linker substitution rates. We chose commercially available ZIF-8³⁷ to establish this protocol because ZIF-8 has shown great potential across various applications,^{5c,38} and the linker exchange of ZIFs has been a subject of academic^{16b,16e,16o,16u,16j,16i,16v,16q,16w,36,39} and industrial⁴⁰ interest. For the incoming linker, we chose the well-established reaction of ZIF-8 with imidazole (ImH)⁴¹ that yields a material termed SALEM-2.^{16b} We ultimately adopted a protocol that included the development of a reliable way to measure quantitative kinetic rate constants of the exchange reaction and a way to assess the contribution of diffusion to these rate constants. When reaction conditions led to rates too slow to be reliably measured in reasonable time frames, we complimented the quantitative kinetic method with small dye molecule encapsulation experiments, which provided valuable mechanistic understanding for reactions in this kinetic regime. The strength of this protocol became evident from our analysis of the solvent-dependence of linker exchange in ZIF-8. Our quantitative rate constants collected at various concentrations of entering linker revealed changes in reaction order between the solvents, which would have been difficult to detect by a less quantitative method. By analyzing the observed behavior in the light of the known behavior of simpler complexes, we were able to formulate a mechanism that rationalized the empirical kinetic and structural data. This mechanism involves three competing reaction pathways, whose contribution to the overall linker substitution rate varies depending on the solvent. We anticipate that this mechanism could be useful in predicting how the linker exchange kinetics in ZIF-8 will respond to new conditions (i.e. different solvent and entering linker). In addition to providing detailed mechanistic information for

linker exchange in ZIF-8, the protocol we have established is a step towards better understanding the general features of linker exchange reactions that occur in MOFs regardless of the type of metal nodes and organic linkers.

3.2 The ZIF-8 Structure as it relates to Linker Exchange Kinetics

An understanding of the kinetics of a linker substitution reaction must begin with an assessment of the number of chemically distinct linkers and thus the number of anticipated rate processes. The 2-methylimidazolate (MeIm^-) linkers of ZIF-8 (**sod**- $\text{Zn}(\text{MeIm})_2$) have only one coordination environment in the crystal bulk⁴² due to the high symmetry of the sodalite (**sod**) topology.⁴³ Thus, the exchange of these linkers with imidazole can be thought of as the reaction of many chemically equivalent *subunit complexes* (Figure 3-2) in a solid solution.⁴⁴ This reduction of complexity in going from a 3D extended framework to a molecular species, which is enabled by the high symmetry of ZIF-8, greatly simplifies the resulting kinetic analysis.

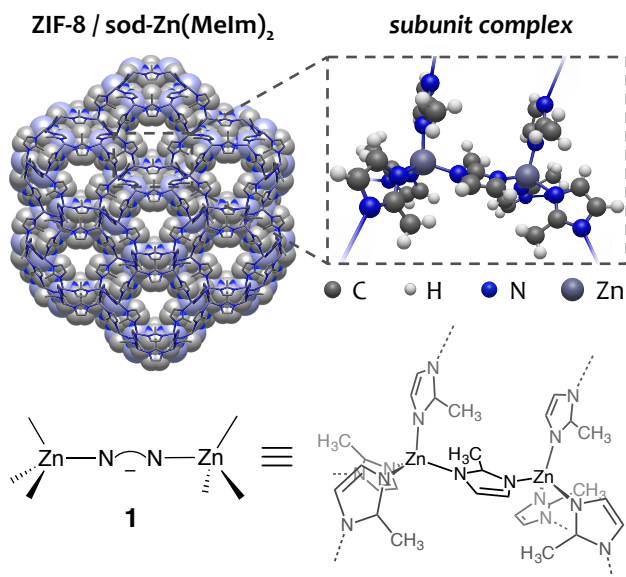


Figure 3-2. The structure of ZIF-8/*sod*-Zn(MeIm)₂ reduced to a subunit complex for the purpose of drawing reaction schemes. The simplest representation depicts just the linker to be exchanged and its two associated tetrahedral Zn(II) nodes.

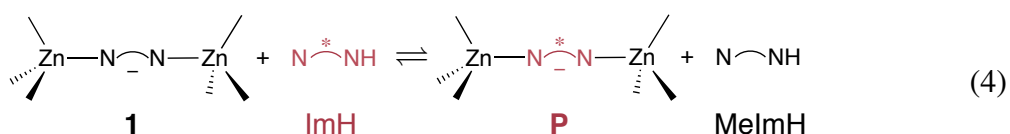
3.3 Kinetics Method and Mechanism

The rate of the overall solid-liquid exchange reaction (eq. (3-2)) will therefore be some function of the concentration of imidazole, [ImH], (eq. (3-3)) that can be related back to the molecularity of reaction steps in the molecular pathway(s) that lead to linker exchange at one *subunit complex*.⁴⁵ Our kinetics method¹⁸ (see experimental section) consists of measuring the initial rates⁴⁶ of the linker exchange reaction of ZIF-8 with imidazole at various initial concentrations of imidazole, [ImH₀], from which we can deduce empirical reaction orders and the corresponding kinetic rate laws. We tracked the progress of the reaction with an *ex situ* digest ¹H-NMR method, using separate batch reactions for each time point.



$$rate = k\{\mathbf{1}\} [\text{ImH}]^n \quad (3-3)$$

For a pathway to lead from starting material **1** to product **P** (eq. (3-4)), it must involve (1) dissociation of 2-methylimidazolate, (2) association of imidazole, and (3) deprotonation of imidazole to form imidazolate. However, the sequence of these steps and the co-reactants involved is unknown. By working backwards from empirical reaction orders, we can rule out hypothetical pathways until we reach the set that are consistent with the observed behavior.⁴⁷



For example, consider the two hypothetical pathways shown in Figure 3-3. The first, which involves imidazole associating in a late step after the rate-determining dissociation of 2-methylimidazole, would have a rate that is independent of $[\text{ImH}_0]$ (i.e., zero-order in imidazole). The second, in which imidazole associates in an irreversible first step, would have a rate with linear dependence on $[\text{ImH}_0]$ (i.e., first-order in imidazole).

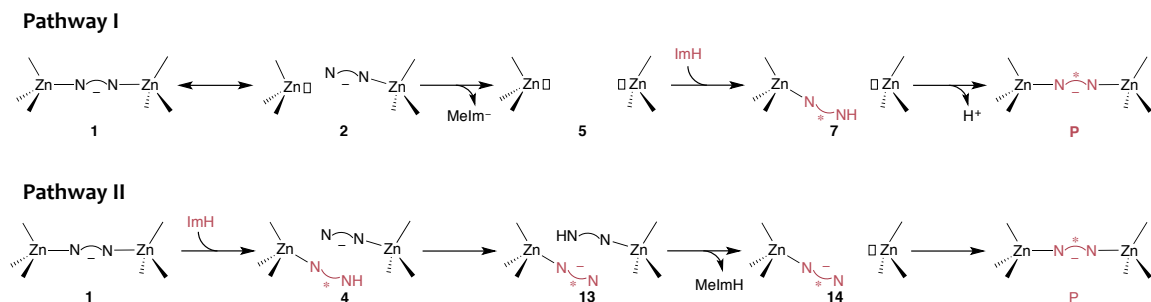


Figure 3-3. Two hypothetical pathways for linker exchange of sod-Zn(MeIm)₂ with imidazole:

(I) zero-order in imidazole and (II) first-order in imidazole.

To distinguish plausible hypothetical reaction pathways from implausible ones, we must be able to differentiate between them based on their kinetic behavior.⁴⁷ This will not be possible if, for instance, the observed reaction orders are from some process other than the chemical reaction of linker exchange with imidazole. In particular, for solid-liquid reactions in porous materials, diffusion can influence the rate in ways that disguise the true reaction order.⁴⁸

3.4 Experiments to Rule out Rate Control by Diffusion

If diffusion is rate controlling for a solid-liquid reaction in a porous material (i.e., the diffusion of a liquid-phase reactant is much slower than the rate of chemical reaction), the reaction will appear first-order in the reactant regardless of its true kinetic order.⁴⁸ This happens because diffusion is proportional to the concentration gradient. Due to this complication, we needed first to find a way to ensure that diffusion is not rate controlling.

The test that we used is simple in concept. It relies on the fact that, for a diffusion-controlled reaction, the rate is proportional to the exposed area of unreacted solid and therefore will always get slower with increasing particle sizes.⁴⁹ Conversely, if diffusion is much faster than the chemical reaction, and thus the chemical reaction is rate

controlling, the rate will be independent of particle size.⁵⁰ In an intermediate range, when diffusion and reaction occur on similar timescales, the reaction rate will be constant for an initial range of small particle sizes and will decrease thereafter (Figure 3-4).⁵¹

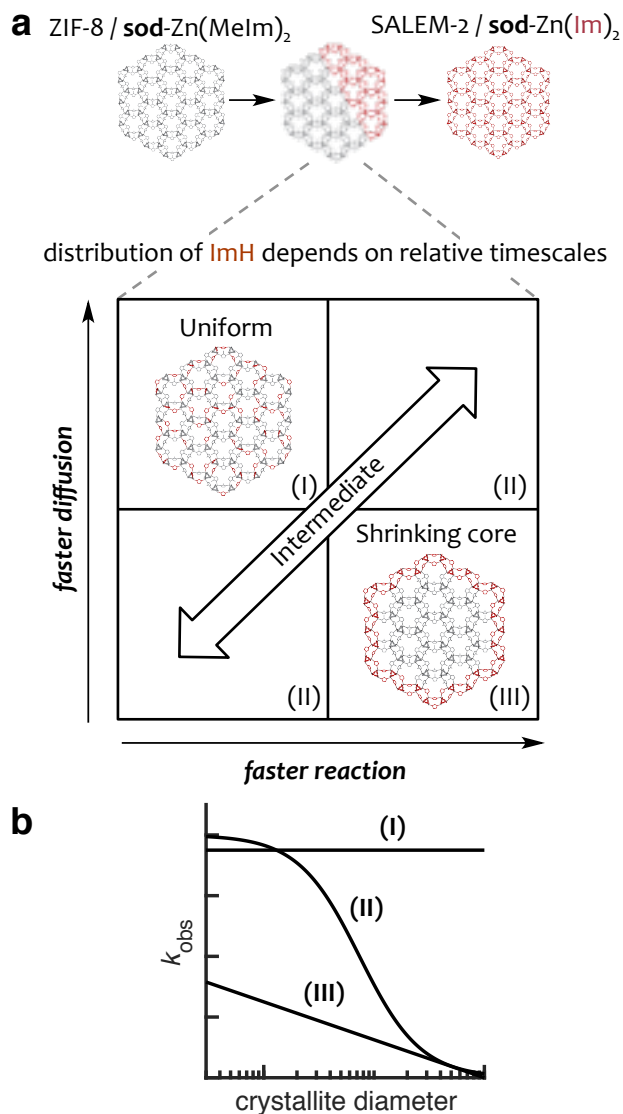


Figure 3-4. The structural basis for kinetic experiments to rule out rate control by diffusion: (a) the spatial relationship between conversion and reaction product distribution means that the relative timescale of diffusion and reaction can be identified from (b) the shapes of the observed rate constant, k_{obs} , versus particle size plots. The three regimes are (I) reaction control, (II) intermediate, or (III) diffusion control.

Our measured rate constants (k_{obs}) of linker exchange (Figure 3-5) obtained from size-controlled ZIF-8 samples that ranged from 80 nm to 10 μm in average diameter (TEM-derived size distributions in Figure 3-6) clearly indicate that diffusion is not rate controlling. This is evident from the existence of a range of particle sizes for which the reaction rate is independent of particle size, which suggests that diffusion and reaction occur on similar timescales (regime II in Figure 3-4). We conducted reactions at both low (0.0735 M, Figure 3-5a) and high (0.294 M, Figure 3-5b) $[\text{ImH}_0]$ and found that diffusion was not rate controlling for either concentration.

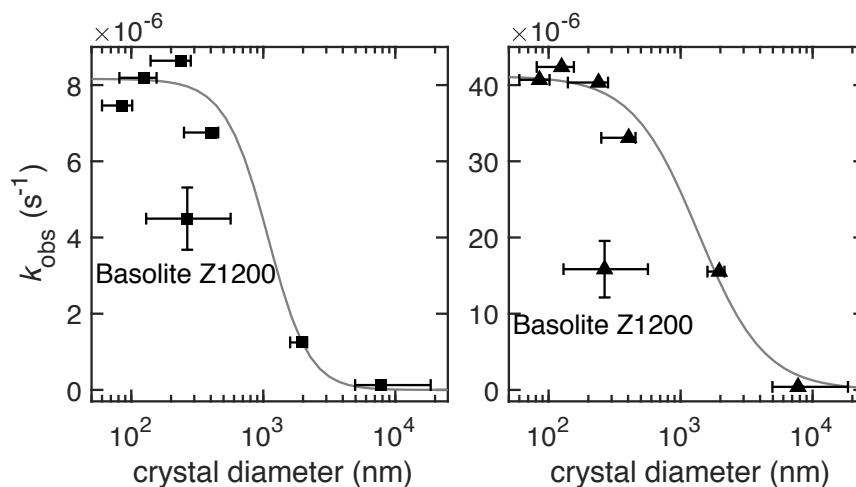


Figure 3-5. The dependence of linker exchange kinetics on ZIF-8 crystal size as measured in *n*-butanol at 70 °C with (a) 0.0735 M and (b) 0.294 M imidazole. Data are plotted for size-controlled (filled symbols) and commercially obtained (open symbols) ZIF-8.⁵⁶ Crystal diameter values come from statistical analysis of transmission electron micrographs, scaling the number distribution of grain diameters to a volume (weight) distribution. The *x*-values are the mass median diameters (D_{50}) of the crystal grain size distribution, and *x*-error bars represent the span of the distribution from 10 % (D_{10}) to 90 % (D_{90}) of the distribution by weight (Figure 3-6, Table 3-1). The lines are meant to guide the eye and do not represent a mathematical fit to the data. Uncertainty in k_{obs} for Basolite Z1200 indicates the 99 % confidence interval.

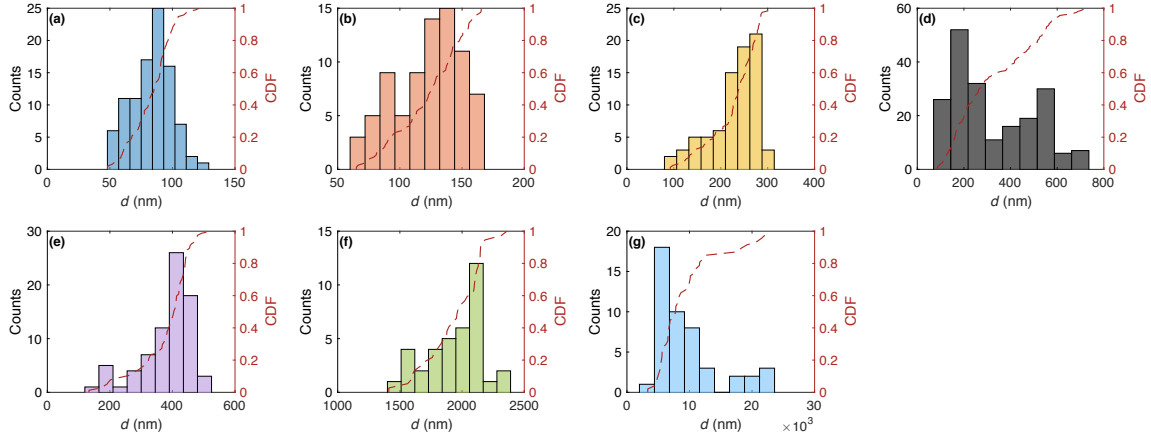


Figure 3-6. Particle size distributions obtained from TEM imaging of size-controlled ZIF-8 particles shown as counts versus grain diameter, d , in nm for (a) 1.26 mL, (b) 1.008 mL, (c) 0.504 mL, (d) Basolite Z1200, (e) 0.252 mL, (f) 1.96 μm . CDF = cumulative distribution function of the particle volume distribution (equal to weight for constant density). The individual measurements of d are shown in Appendix IV.

Sample	d_{ave} (nm)	Std Dev (nm)	D10 (nm)	D50 (nm)	D90 (nm)	$k_{\text{obs}} (\text{s}^{-1}) \times 10^6$ at 0.0735 M	y-int	$k_{\text{obs}} (\text{s}^{-1}) \times 10^6$ at 0.294 M	y-int
(a) M	83	± 16	60	85	102	7.06	0.928	40.7	0.928
(b) L	123	± 27	81	125	155	7.82	0.943	42.4	0.939
(c) XL	229	± 51	140	239	282	8.30	0.967	40.3	0.959
(d) Basolite Z1200	324	± 173	130	265	565	4.50	0.973	15.8	0.966
(e) XXL	382	± 82	251	404	455	6.50	0.979	33.1	0.978
(f) 2 μm	1946	± 224	1598	1963	2149	1.25	0.979	11.9	0.968
(g) 10 μm	9485	± 5151	4960	7755	18528	0.133	0.993	0.402	0.990

Table 3-1. The parameters obtained from the particle size distributions in Figure S3-6. Average grain diameter, d_{ave} , is the mean of the number distribution of grain diameters. D10, D50, and D90 are the corresponding d values of the mass-weighted cumulative distribution functions in Figure 3-6 at CDF = 0.1, 0.5, and 0.9 respectively. In other words, 10 % of the particles have grain diameters less than D10, 50 % are smaller than D50, and 90 % are smaller than D90. D50 is also referred to as the mass median diameter.

Whereas other studies have found intraparticle diffusion to be a major factor in linker exchange kinetics,^{16g,16x} including in a recent study in ZIF-8,³⁶ our avoidance of these effects seems to come from unique aspects of our methodology. Our methodology used initial rates early on in the linker exchange process (< 10 %),⁵² which stops the reaction before the product layer can become too thick, making transport through it rate limiting.⁵¹

We also observed features in the conversion vs. time plots used to determine the above k_{obs} values (Figures AI-7 and AI-8) that confirm our prior claim¹⁸ that rapid surface ligand exchange (above surface)^{16j,53} is a constant that does not interfere with accurate measurement of the rate of the much slower linker exchange in the bulk (below surface). The y-intercepts in these plots varied from 1 % (for 8 μm) to 7 % (for 85 nm), which correlate linearly with our expected values calculated from the density of groups at the external surface of ZIF-8 (Figure 3-7, see Appendix II for calculations). These changing y-intercepts have no effect on the k_{obs} values, which are obtained from the slopes in these plots. Hence, the much greater external crystal surface area of MOF nanoparticles did not interfere with accurate measurement of the bulk linker exchange rate by our initial rates method.

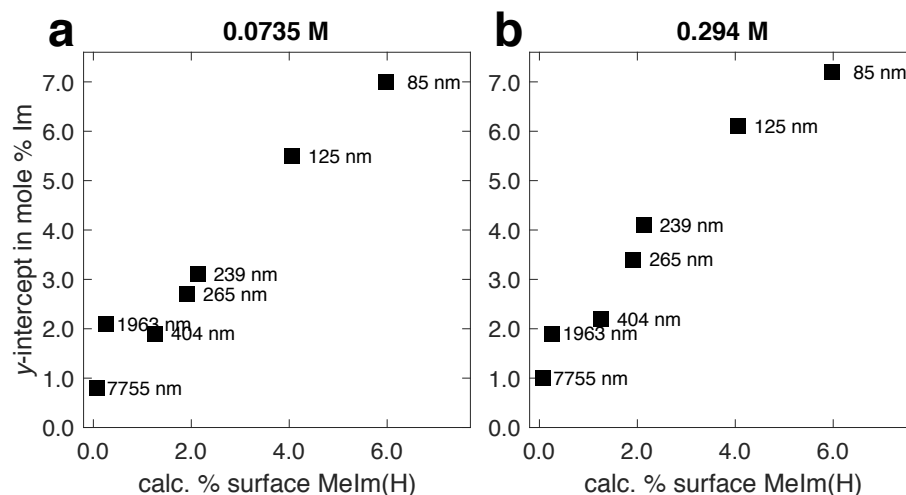


Figure 3-7. The correlation between ZIF-8 crystal size and the y-intercept in conversion vs. time plots for (a) 0.0735 M and (b) 0.294 M imidazole in *n*-butanol at 70 °C. The experimental y-intercepts are from data in Figures AI-3, AI-7, and AI-8. Calculated % surface MeIm(H) is shown for the {100} surface upper bound (dangling RImH + framework RIm⁻). See Appendix II for calculations.

Having established that our method allowed us to obtain kinetics of the chemical reaction (rather than of diffusion), we moved on to examine how these kinetics depended on the solvent. Importantly, our particle size-dependence study was conducted in the solvent 1-butanol (BuOH), which has the largest molecular size of all the solvents tested in this study (Table AV-5), and is therefore the solvent most likely to lead to mass transport limitations.⁵⁴⁻⁵⁵ For these solvent-dependence studies, we used the 265 nm diameter ZIF-8 particles (Basolite Z1200), which are small enough to avoid a large contribution from diffusion. Additionally, Basolite Z1200 is a standard material that is available in large scale, which is important for the material-intensive *ex situ* digestion method of tracking the reaction progress that we employed.

3.5 The Solvent-Dependence of Linker Exchange Kinetics in ZIF-8

We next investigated the solvent-dependence of linker exchange kinetics in ZIF-8 using our methodology. Study of this effect is important, as solvent choice appears to be a primary lever of control to direct MOF linker exchange reactions to a desired outcome. The solvent has been found to affect both the rate and success of linker exchange in MOFs.^{16b-c,u} The solvent-dependence of the ligand substitution kinetics of simpler complexes has been studied,⁵⁷ and this knowledge forms a basis from which we can understand the behavior in MOFs. The exchange of imidazole into ZIF-8 (eq. (3-2)) is advantageous for a solvent-dependence study, as imidazole is highly soluble in a wide array of solvents including water. We chose solvents that represented a wide array of solvent properties, including some that are known to facilitate ZIF-8 synthesis—methanol⁵⁸ (MeOH), ethanol^{33c} (EtOH), 1-butanol^{33c} (BuOH), and water^{33a}—and some that are not—dimethyl sulfoxide (DMSO) and acetonitrile (MeCN). Importantly, none of these solvents can form the **sod** phase of Zn(Im)₂ from Zn(II) and imidazole in solution (in fact no direct synthesis of **sod**-Zn(Im)₂ has been reported^{16b}). This means that we can use PXRD to ensure that imidazole in the product was incorporated by linker exchange rather than by dissolution-recrystallization, as in the latter case we would observe a new crystalline phase. In all cases **sod** was the only phase present in all the exchanged samples used for kinetics analysis (See Figures AIII-1 to AIII-6), indicating that imidazole was incorporated into the structure via linker exchange and not dissolution-recrystallization in all cases.⁵⁹

[imidazole]	0.0294 M		0.0735 M		0.147 M		0.294 M	
Solvent	k_{obs}	$t_{1/2}$	k_{obs}	$t_{1/2}$	k_{obs}	$t_{1/2}$	k_{obs}	$t_{1/2}$
DMSO	0.61 ± 0.04	13 d	1.7 ± 0.1	5 d	4.2 ± 0.1	46 h	9.3 ± 0.4	21 h
Ethanol	0.74 ± 0.05	11 d	3.4 ± 0.1	57 h	5.0 ± 0.1	39 h	12.8 ± 0.3	15 h
1-Butanol	1.52 ± 0.08	5 d	4.5 ± 0.3	43 h	7.2 ± 0.2	27 h	16 ± 1	12 h
Acetonitrile	— ^b	—	1.3 ± 0.1	6 d	5.8 ± 0.4	33 h	30 ± 2	6 h
Methanol	2.7 ± 0.2	3 d	5.9 ± 0.3	32 h	13 ± 1	15 h	44 ± 4	4 h
Water ^c	20 ± 2	9 h	58 ± 7	3 h	176 ± 14	66 min	500 ± 30	23 min

^aUncertainty in k_{obs} is expressed as the standard deviations of the slopes obtained from linear regressions of $c_{2\text{-MeIm}}$ versus time plots. ^bThe rate was too slow to be accurately measurable by our methodology, as indicated by a non-linear initial rate plot (Figure AI-4) and very low (11 % conv.) imidazole incorporation even after 10 d reaction (Table 3-3). ^cRate measurements in water come from reactions at 4 °C, and the kinetics parameters for exchange in deuterium oxide with 0.147 M imidazole are $k_{\text{obs}} = 114 \pm 11$ and $t_{1/2} = 101$ min.

Table 3-2. Experimental Rate Constants (k_{obs} in $\text{s}^{-1} \times 10^{-6}$) and Calculated Half-lives of Ligand Exchange of ZIF-8/**sod**-Zn(MeIm)₂ with Imidazole^a

We measured the initial rates of linker exchange in the five organic solvents at 70 °C. We observed extremely fast exchange rates in water, which required that we make measurements in that solvent at 4 °C instead. The results of our extensive kinetics measurements in these solvents are compiled in Table 3-2 and in plots of k_{obs} versus $[\text{ImH}_0]$ in Figure 3-8 (Note: each point in Figure 3-8 comes from an entire set of ≥ 12 separate batch reactions run to different times, plots in Appendix I). Rates of linker exchange varied widely even within one solvent. For example, for the MOF to get to 5 % exchange in DMSO (beyond the 2 % contribution from surface ligand exchange) took 20

h at the lowest $[\text{ImH}_0]$ but only 1 h at the highest $[\text{ImH}_0]$. The wide variation in rates between solvents confirmed our expectation that MOF linker exchange is highly solvent-dependent. At the highest $[\text{ImH}_0]$, 5 % conversion (1 h in DMSO) took 20 min in MeOH and only 2 min in water.

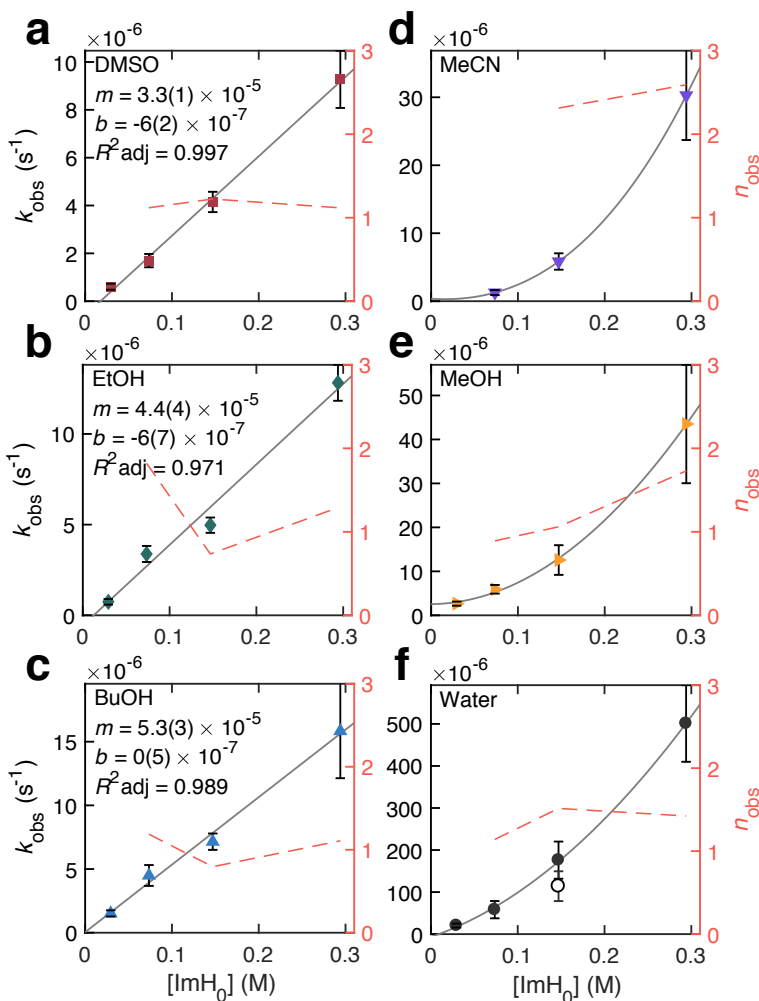
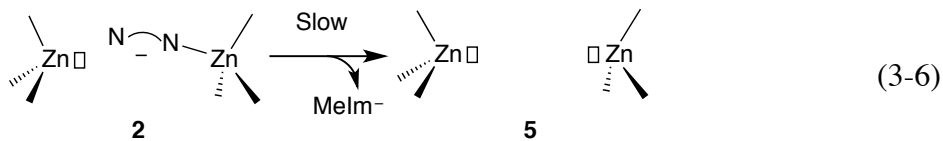
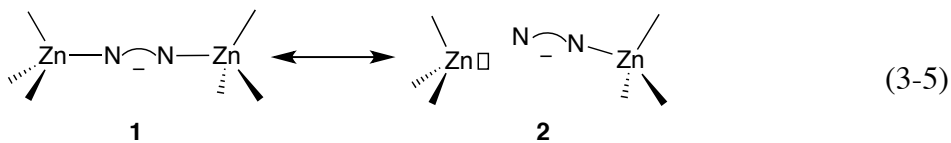


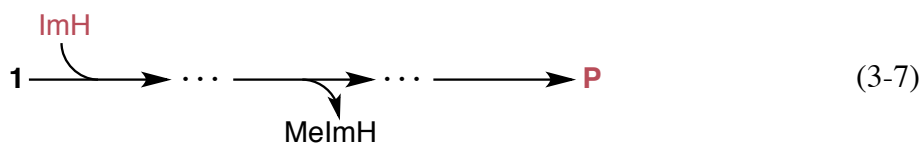
Figure 3-8. Plots of observed initial rate constant, k_{obs} , versus free concentration of imidazole, $[\text{ImH}_0]$, for (a) dimethyl sulfoxide, (b) ethanol, (c) 1-butanol, (d) acetonitrile, (e) methanol, and (f) water (filled) and deuterium oxide (open). Error bars indicate the 95 % confidence interval. Calculated empirical reaction orders in imidazole, n_{obs} , are plotted on the right y-axes.

The first notable feature in the plots in Figure 3-8 is that the solvents can be split into two groups, those that display roughly linear dependence on $[\text{ImH}_0]$ (DMSO, EtOH, and BuOH) and those with significant polynomial character (MeCN, MeOH, and water). The polynomial curvature of the second group indicates empirical reaction orders in imidazole, n_{obs} , that are greater than 1, and these calculated values, plotted on the right y-axes in Figure 3-8, vary from 1–2 for MeOH and water to > 2 for MeCN. The observed greater than first-order dependence in imidazole could come from the involvement of multiple imidazole molecules in steps in or prior to the rate determining step. The fractional (non-integer) empirical reaction orders—meaningless for a reaction that occurs in a single elementary step—are, for a multistep reaction, the result of either multiple processes contributing to the overall rate or reversible steps in a single pathway.⁴⁷ The solvents in the second group, with $n_{\text{obs}} > 1$, generally had faster rates at all $[\text{ImH}_0]$ than those in the first group, with $n_{\text{obs}} \sim 1$. The notable exception to this trend was acetonitrile, which began as the slowest solvent for exchange at low $[\text{ImH}_0]$ but became the third fastest at the highest $[\text{ImH}_0]$.

The second striking feature in the rate data in Figure 3-8 is that, for all solvents, k_{obs} increases with $[\text{ImH}_0]$ through the whole range of $[\text{ImH}_0]$, never reaching a limiting value. This is reflected also in the n_{obs} values that are ≥ 1 in all solvents for the full range of $[\text{ImH}_0]$. This finding is significant because it excludes sole contribution to the overall rate from pathways that involve the rate-determining dissociation of 2-methylimidazolate in an early step (i.e., eq. (3-5) to (3-6)). The rate from such pathways can exhibit first-order dependence on entering ligand at low $[\text{ImH}_0]$, when the reverse reaction **5**→**2** is kinetically relevant, but would saturate to a limiting rate at high $[\text{ImH}_0]$.²¹



Instead, our results suggest involvement of an imidazole molecule in an early step before the dissociation of 2-methylimidazole (i.e., the general case eq. (3-7)).



The standard interpretation of this behavior would be a mechanism in which imidazole associates to Zn(II) prior to 2-methylimidazole leaving.²¹ This interpretation is problematic for several reasons though. First, associative reactions are generally accelerated in solvents that are good donors for the metal,⁶⁰ and yet we observed the slowest rates in DMSO, the solvent with the strongest coordinating power for Zn(II),⁶¹⁻⁶² and moderate rates in the weakest donor, MeCN.⁶³ Second, this interpretation fails to provide a rationale for the observed second-order in imidazole dependence in the second group of solvents. Finally, we would intuitively expect the bulky environment of methyl groups around Zn(II) (Figure 3-2) to hinder access to all but the smallest nucleophile. And we would also expect that the strain from rearrangement of the tetrahedral site in the solid to accommodate a fifth coordinating group would be energetically unfavorable compared to removal of a coordinating group by linker dissociation. This structural

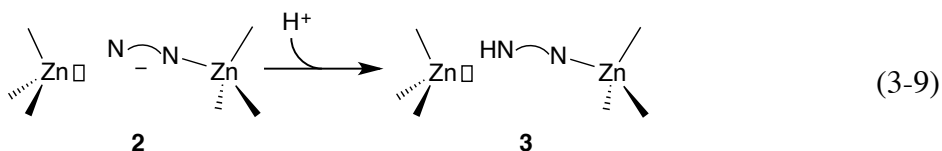
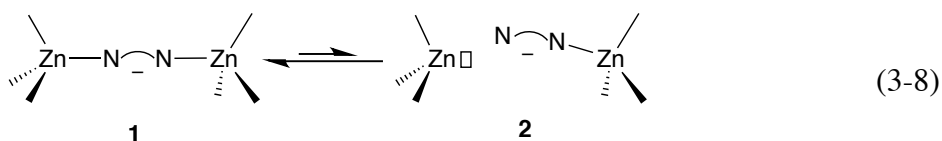
reasoning, together with the empirical trends across solvents that run counter to our expectations for an associatively activated exchange pathway, lead us to conclude that there is likely a different mechanism behind the observed first-order and higher dependence in imidazole.

3.6 Rationalization of the Solvent Trends from the Kinetic Behavior of Complexes in Solution

A key motivation for our work was to determine if the known kinetic behavior of complexes in solution could be used to rationalize the kinetic behavior observed for linker exchange reactions in solid MOFs. This unified view, which relates the kinetics of larger metal–ligand assemblies with that of simpler complexes has led to significant insight for many materials^{10,26a,26b,30f,31d,31f} and natural phenomena.^{25d,27f,27k} Consistent with this view, our consideration of the known kinetic behavior of ligand substitution in Zn²⁺ and chelate complexes led us to formulate a mechanism that can rationalize all of the seemingly inconsistent trends in our observed kinetics data.

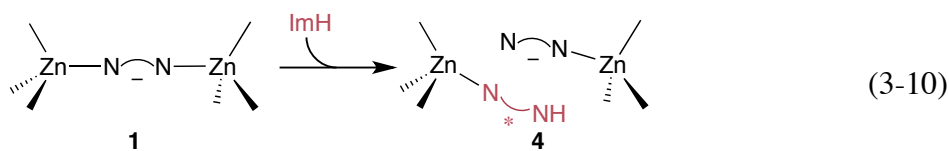
The first realization was that, in studies of ligand exchange in Zn(II) complexes,^{64–73} tetrahedral complexes with two or more anionic ligands (such as 2-methylimidazolate) invariably follow dissociative mechanisms,⁷³ as do those with bulky ligands.⁷⁴ These two effects can be easily understood as an excess of electron density or steric bulk around the metal disfavoring association by a nucleophile. The second was that, for chelate complexes, including those of Zn(II),⁷² *proton-assisted* or *acid-catalyzed* dissociation of the first binding group of the chelate⁷⁵ is frequently rate-determining.^{72,76–78} We can illustrate the reason for this second effect by using the reaction in ZIF-8 as a specific example. In the step shown in eq. (3-8) the reverse rate constant k_{21} is expected to

greatly exceed the forward rate constant k_{12} , meaning that **2** is short-lived. This is because the dissociated N of the linker has both a high *effective concentration*, due to the other N still being attached to the framework, and also the perfect orientation to react and re-coordinate to Zn(II). If, however, a proton can intercept the dissociated N (eq. (3-9)), it will be less able to re-coordinate to Zn(II). Furthermore the remaining Zn–N bond will be weakened by the protonation and thus more likely to dissociate.

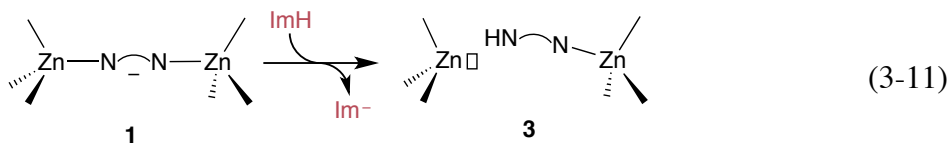


3.7 The Proton-Assisted Dissociation Pathway

Our hypothesis is that most of the observed first-order or greater dependence in imidazole for all solvents through the entire range of $[\text{ImH}_0]$, comes not from rate-determining association of imidazole in a first step (eq. (3-10)),



but rather from proton transfer from imidazole to **1** in the first step (eq. (3-11)), consistent with the behavior of chelate complexes in solution.



These two types of pathways would give identical empirical reaction orders and thus an analysis based on n_{obs} alone in a single solvent could not distinguish between them. However, by comparing trends in the magnitudes of k_{obs} and n_{obs} across solvents we concluded that the second pathway is more likely the first.

The first trend that supports this hypothesis of a *proton-assisted dissociation pathway* is the trend in exchange rates with the coordinating ability of the solvent. Associative reactions such as eq. (3-10) are generally accelerated in solvents that are good Lewis basic donors for the metal because the solvent can associate as a ligand in a pathway that ends in ligand substitution; for example, rates of ligand exchange in Pt(II) square planar complexes that vary in the order MeOH < water << DMSO.⁶⁰ For linker exchange in the MOF, however, we observed rates in the order DMSO < MeOH << water, which breaks with the order of coordinating power for Zn(II), which instead is MeOH < water < DMSO.⁶¹ The poor donor MeCN, with the lowest coordinating power for Zn(II) of all six solvents is nevertheless the third fastest solvent for exchange at high $[\text{ImH}_0]$, which also contradicts what would be expected for an associative pathway.

A step that generates an imidazolate anion (eq. (3-11)) would clearly be facilitated in solvents that are good hydrogen bond donors (HBD) and thus can stabilize and solvate anions (Figure 3-9b and Table AV-2). The rapid exchange kinetics in the good HBD solvents MeOH and water are therefore consistent with this hypothesis of *proton-assisted dissociation pathway*. Also consistent is the fact that exchange in water was not somewhat, but significantly faster than exchange in MeOH. Water could stabilize the imidazolate anion particularly well by both hydrogen bonding and by favorable acid-base equilibria in solution (eq. (3-12)). Furthermore, water can facilitate rapid proton transfer

by acting as a proton shuttle.⁷⁹ It was initially less clear how the poor HBD solvent MeCN could support rapid linker exchange by the same mechanism.



By examining the known behavior of imidazole in MeCN, we were able to not only rationalize how this solvent could facilitate rapid exchange by the *proton-assisted dissociation pathway*, but also make sense of the initially surprising pronounced second-order in imidazole dependence in MeCN, which was the highest of any solvent tested. While MeCN is a poor HBD solvent, and thus does not hydrogen bond with the N of imidazole or stabilize the imidazolate anion like MeOH and water, its moderate polarity (Table AV-1) combined with its lack of strong donor or acceptor properties make it suited to facilitate hydrogen bonding among solutes. Imidazole speciation has been measured previously in various solvents,⁸⁰ and MeCN was found to support the formation of hydrogen-bonded imidazole dimers, (ImH)₂ (Table AV-4), whereas in the same experiments such dimers were undetectable in DMSO or MeOH. Involvement of these hydrogen bonded imidazole dimers could explain the pronounced second order in imidazole kinetics in MeCN (Figure 3-9a). Indeed, kinetic behavior with second order dependence in exchanging ligand is exceedingly rare for soluble complexes, but it has been observed occasionally for ligands with the capability to form intermolecular hydrogen bonds.^{271,81}

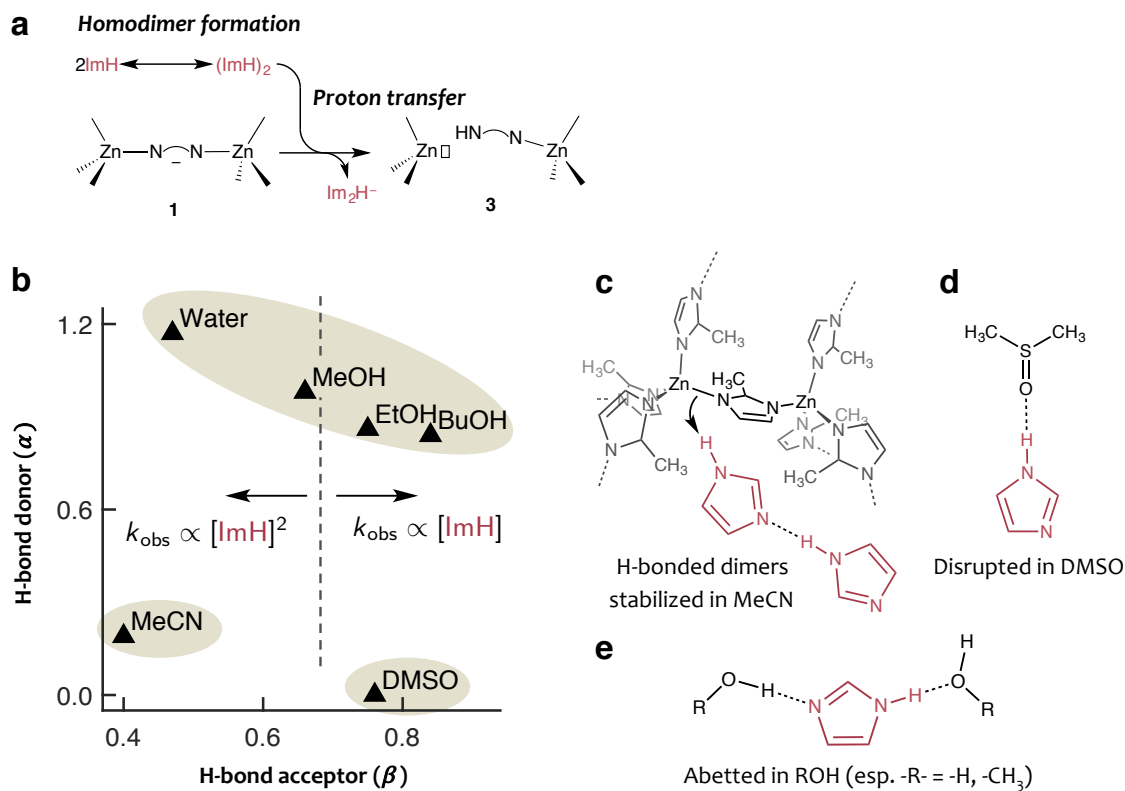


Figure 3-9. Hypothesis that second-order in imidazole kinetics could be a consequence of imidazole dimers playing a key role in a first step, rate-determining proton transfer to the 2-methylimidazolite linker.

This dimer-driven mechanism for MeCN could explain why linker exchange in MeCN is initially so slow compared to the other two $n_{\text{obs}} > 1$ solvents (MeOH and water) at low $[\text{ImH}_0]$. Good hydrogen bond donors such as MeOH and water can facilitate proton donation by imidazole directly, by participating in a hydrogen bond and also by stabilizing the resulting anion (Figure 3-9e). Meanwhile, MeCN promotes proton donation by imidazole indirectly, by not interfering with imidazole's natural tendency to hydrogen bond with itself (Figure 3-9c). Thus, at low $[\text{ImH}_0]$ in MeCN, where dimer formation is rare, there is no suitable proton donor to break the linker bridge (eq. (3-9)). At higher $[\text{ImH}_0]$, imidazole forms dimers that function as better proton donors than

imidazole acting alone, and that serve as Brønsted-Lowry acids in the *proton-assisted dissociation pathway*. In other words, the kinetically relevant proton donor in MeOH and water is either ImH or (ImH)₂, whereas in MeCN it is the dimer (ImH)₂ only. This explanation could account for the fact that the n_{obs} values were between 1 and 2 in MeOH and water, whereas they were consistently ~ 2 in MeCN.

DMSO, with the lowest HBD capability of any of the solvents tested (Figure 3-9b) would, like MeCN, not tend to promote the acidity of the N-H proton in imidazole by hydrogen bonding to the basic N, which begs the question of why it would not, as another polar aprotic solvent, support second order kinetics by the imidazole dimer mechanism. Two related experimental facts about DMSO easily rationalize this trend. First, anions are notoriously poorly stabilized in DMSO (hence the high Bordwell pK_a values for acids that generate anions).⁸² Second, DMSO disrupts hydrogen-bonded networks due to its high HBA basicity (Figure 3-9d) and very low HBD acidity.⁸²

A final experiment that supports the importance of proton transfer in or prior to the rate-determining step comes from deuterium kinetic isotope studies in water. We observed 33 % slower reaction rates in D₂O compared to H₂O at a moderate [ImH₀] of 0.147 M (Table 3-2, Figure 3-8f, Figure AI-6, $k_{\text{obs}} = 1.14 \times 10^{-4} \text{ s}^{-1}$ at 4 °C and [ImH₀] = 0.147 M), which corresponds to a normal solvent kinetic isotope effect of 1.5. This finding is consistent with proton transfer events being in or prior to the rate-determining step.^{46,83} The slowed rates in D₂O could be a result of either rate-limiting proton transfer by water/hydronium or imidazole or both, as the N-H proton in imidazole rapidly exchanges with deuterium before the exchange reaction begins.

At present, the anomalously slow linker exchange kinetics for EtOH are confusing in light of our proposed *proton-assisted dissociation pathway*. However the anomaly is a useful one, as the faster linker exchange kinetics in BuOH than EtOH at every [ImH₀] measured (90–95 % confidence) effectively rules out the possibility of rate control by diffusion. EtOH has a diffusivity 5 orders of magnitude faster than that of BuOH in ZIF-8 at 70 °C.⁵⁵ A possible reason for the faster exchange in BuOH could come from the strong adsorption of BuOH compared to the shorter alcohols in ZIF-8,⁸⁴ but more experiments would be needed to distinguish this possibility from others. A related open question on the solvent-dependence of linker exchange kinetics in ZIF-8 is the role of the solvent in shifting the initial and final thermodynamic energy of MOF,^{85,86} rather than just the kinetic barriers.

3.8 Dye encapsulation experiments to probe linker exchange at low free ligand concentration

Having gathered a large amount of kinetic data on the solvent dependence of linker exchange in ZIF-8, we turned to reinvestigate our previously reported *guest encapsulation by dissociative linker exchange* method (Chapter 2),¹⁸ to both understand this useful approach to guest encapsulation^{19–20} in light of new evidence, and to complement our kinetic studies by providing (1) indirect evidence of an intermediate in the hypothesized *proton-assisted dissociation pathway* and (2) insight into the mechanism(s) at low concentration of free ligand, where we cannot directly measure rates of linker exchange.

In Chapter 2, we demonstrated that the encapsulation of molecules larger than the pore aperture size in the cage-like MOF ZIF-8 occurred more readily in the absence of

free ligand.¹⁸ This tendency was explained by the formation of temporary linker vacancies that were created as a result of dissociative linker exchange. These temporary linker vacancies enlarge the pore apertures in the MOF and allow large guest molecules to diffuse into the pore (Figure 3-10). In the present study, we measured the solvent dependence of guest encapsulation in ZIF-8 by this method to complement our kinetic rate data in two ways. First, such experiments can further test the validity of our *proton-assisted dissociation* mechanism, as this pathway involves the *missing-linker intermediate*, **5**, that is necessary for guest encapsulation (Figure 3-11). Second, these dye uptake measurements provide insight into which mechanism(s) are most significant at low concentration of free ligand, where we cannot directly measure rates of linker substitution.

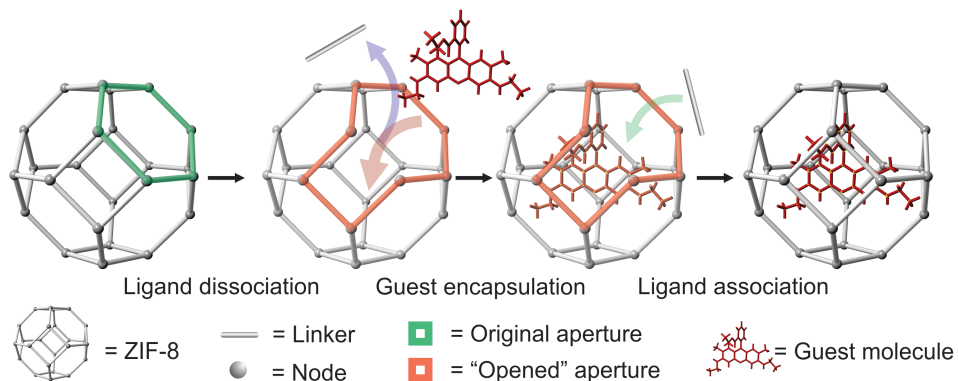


Figure 3-10. Encapsulation of a large organic dye by a dissociative linker exchange pathway in ZIF-8/*sod*-Zn(MeIm)₂.

Using our previous methodology (Chapter 2),¹⁸ we measured the amount of Rhodamine 6G (R6G) dye (~11 Å in diameter) that was encapsulated in ZIF-8 (pore aperture size 3.4–4.2 Å, pore size 11.6 Å)^{37,87} after one week at 100 °C in same solvents

that were used for the kinetic measurements. We measured dye loadings resulting from reactions both in the absence of free ligand in solution and at a moderate concentration (0.147 M) of the native ligand, 2-methylimidazole. In the resulting dye loadings in Figure 3-11a, three main features stand out. First, the highest amount of dye encapsulation by far occurred in protic solvents, and the order (water > EtOH ~ MeOH > BuOH > MeCN ~ DMSO) generally follows the solvents' order of HBD strength. Second, the addition of free MeImH caused a decrease in the amount of dye encapsulated in all solvents. Third, water alone sustains high amounts of dye encapsulation at moderate [MeImH], which makes water again unique among the solvents.

The dye encapsulation results in Figure 3-11a provide additional support for our hypothesis of a *proton-assisted dissociation pathway*. They also suggest that DMSO does not follow this pathway even at low concentration of free ligand, and furthermore point to some unique aspects of water as a solvent for linker exchange in ZIF-8. The support for the *proton-assisted dissociation pathway* is evident from the close correlation between dye encapsulation amount and the Kamlet-Taft α parameters for solvent HBD acidity (Table AV-2 and Figure 3-9b).

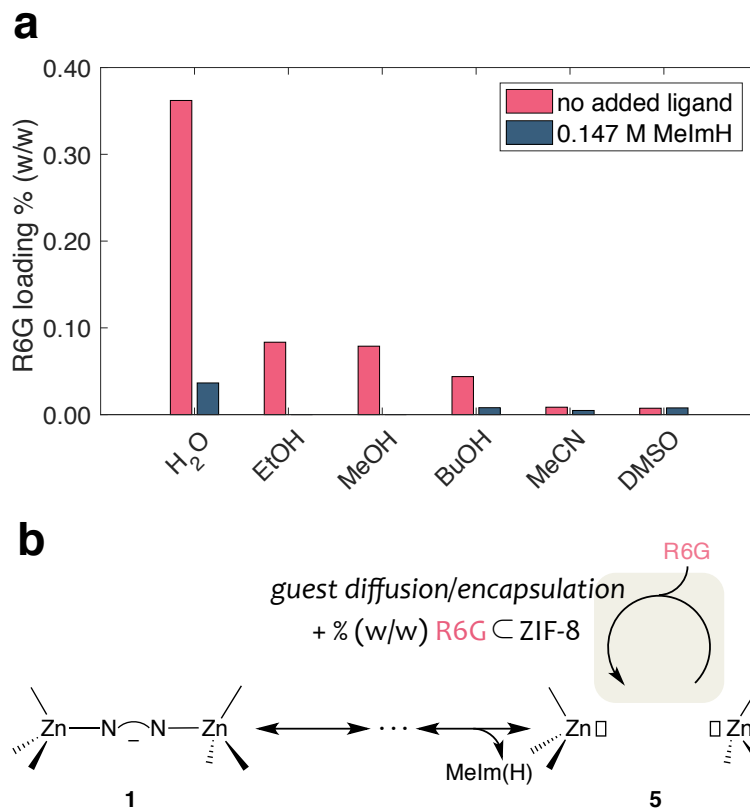


Figure 3-11. (a) Loadings of Rhodamine 6G (R6G) dye guest into ZIF-8 as determined by digestion UV/vis. (b) Proposed molecular pathway for dye encapsulation.

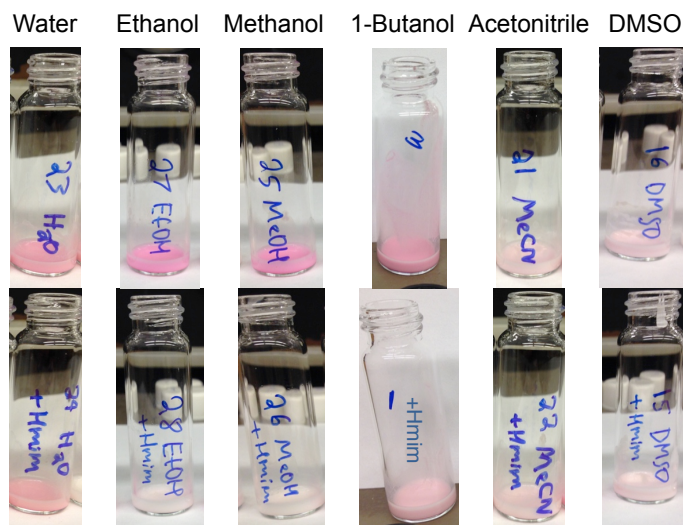


Figure 3-12. Photographs of the solvent dependent encapsulation of Rhodamine 6G dye encapsulation in ZIF-8, both without (top row) and with (bottom row) free ligand.

With no free ligand around, the HBD solvents (BuOH, EtOH, MeOH, and water) could assist linker dissociation by stabilizing the dissociated linker anion (eq. (3-6)). This role is similar but distinct from the role we proposed for these solvents in facilitating proton transfer in the presence free imidazole (eq. (3-11)). Whether by facilitating proton transfer (at high $[\text{ImH}_0]$) or by stabilizing an anion via hydrogen bond donation (with no free ligand), the HBD solvents promote linker dissociation by involvement of a proton. Hence, we have collectively labeled these related processes the *proton-assisted dissociation pathway*.

While we hypothesized that linker exchange in MeCN follows the same *proton-assisted dissociation pathway*, the extremely low uptake of dye in this solvent with no free ligand (as opposed to the HBD solvents) still makes sense in light of our proposed mechanism. In our proposed pathway, MeCN depends on imidazole dimers as the proton donor. Therefore, linker dissociation cannot occur to a significant extent in the absence of free imidazole. The low dye uptake in MeCN at moderate $[\text{MeImH}]$ is consistent with what was observed for MeOH and EtOH (and to a lesser extent BuOH). This decrease in dye uptake in the presence of free ligand is consistent with a mechanism in which free MeIm(H) and the dye molecule compete for the intermediate **5** (Figure 3-11b).

Two phenomena then remain to be explained. Why is water uniquely able to facilitate high amounts of dye encapsulation in the presence of free ligand? And why does DMSO lead to such low encapsulation?

Putting aside our mechanistic model, we would expect guest encapsulation to occur most readily in a solvent that can stabilize the open Zn(II) sites in **5**, thus “leaving the window open” (Figure 3-10) for diffusion of R6G. While the order of water > MeOH

agrees with this expectation, DMSO, with the strongest donor power for Zn(II), is again an outlier. In the context of our other findings, though, this seeming discrepancy can be resolved. DMSO, a non-HBD solvent, solvates anions poorly and thus cannot support the *proton-assisted dissociation pathway* that leads to encapsulation. The fact that this behavior pervades even at low concentration of free ligand suggests that exchange in DMSO occurs through a different pathway, rather than by the same pathway as the other solvents at a slower rate. Drastic changes in reaction medium can often affect mechanism rather than just changing kinetic parameters.⁵⁷ Saving the discussion of water's anomalous behavior for a later section, we will briefly address this alternative pathway in DMSO.

3.9 An *Eigen-Wilkins pathway* for DMSO

Having arrived at a mechanism, the *proton-assisted dissociation pathway*, that is consistent with all the experimental observations—the solvent ordering in k_{obs} and dye encapsulation, the unique behavior of MeCN, the pronounced second-order in imidazole dependence for some solvents, the rapid kinetics in water, and the normal solvent kinetic isotope effect—we are left to consider that that DMSO, a non-HBD solvent, does not likely follow the same pathway. Two experimental observations support this conclusion of a distinct mechanism for DMSO. First, DMSO was the worst solvent for guest encapsulation, despite the fact that it should be an exceptional solvent to stabilize **5**. Second, when we ran linker exchange reactions for extended reaction times (10 d at 70 °C), DMSO was the only solvent to not result in a crystalline phase change from **sof** to the dense **zni** phase at any [ImH₀] (summarized in Table 3-3 and Figure 3-13, PXRD patterns in Figures AIII-10 to AIII-15, and discussion on pp 144–151). The crystalline

phase change occurred for all $[ImH_0]$ in water and MeOH at these extended, 10 d, reaction times, causing us to question if it is an inevitable consequence of a rapid exchange rate. However, from our quantitative rate data, we can see that exchange occurred in DMSO at $[ImH_0] = 0.294$ M at a rate 13 and 3 times faster than conditions that led to the **sod** to **zni** crystalline phase change (in EtOH and MeOH, respectively, both at 0.0294 M). Thus, the tendency for a solvent to result in a crystalline phase change at long reaction times is not *rate dependent* so we concluded that it must be *mechanism dependent*.

[ImH] (M)	DMSO		Ethanol		1-Butanol		Acetonitrile		Methanol	
	conv. (%)	phase	conv. (%)	phase	conv. (%)	phase	conv. (%)	phase	conv. (%)	phase
0.0294 M	14.0	SOD	21.4	SOD/zni	23.4	SOD	11.0	SOD	54.0	zni/SOD
0.0735 M	24.5	SOD	83.3	zni/SOD	43.5	SOD	26.0	SOD/zni	82.4	zni
0.147 M	38.1	SOD	94.4	zni	73.3	SOD/zni	90.9	zni	85.6	zni
0.294 M	59.8	SOD	94.0	zni	95.8	zni	94.5	zni	90.2	zni

Table 3-3. Values for conversion and phases observed for 10-day reactions at 70 °C.

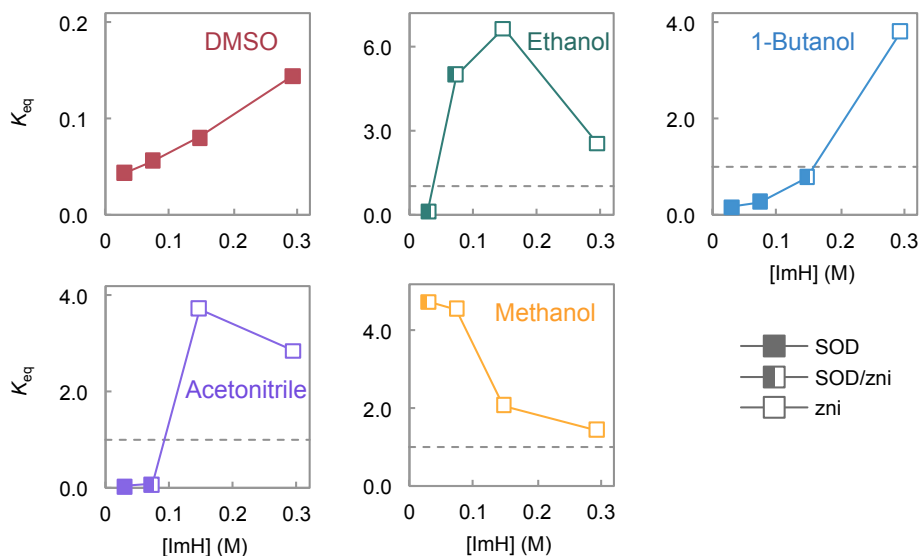
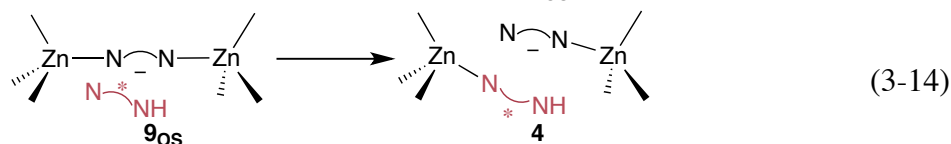
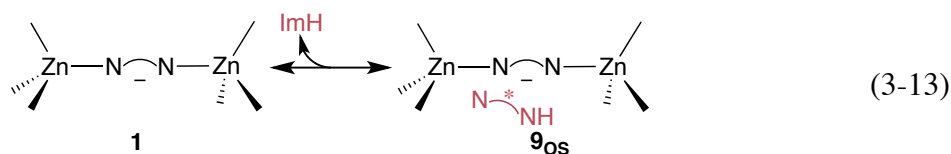


Figure 3-13. Equilibrium constant versus initial [ImH] for 10-day reactions at 70 °C. Shading of the data points indicates qualitatively the relative amount of each phase observed in PXRD (patterns in Figures AIII-10 to AIII-14). $K_{eq} = 1$ (thermoneutral) is indicated with dashed lines.

A mechanistic pathway that could rationalize the above trends is an *Eigen-Wilkins pathway*, as is common for the substitution of octahedral complexes.⁸⁸ The distinguishing feature of this pathway is the rapid formation an encounter complex of imidazole in the secondary coordination sphere of Zn(II) with the correct orientation for reaction (eq. (3-13)) before subsequent interchange of the ligands between the first and second coordination spheres (eq. (3-14)).



This mechanism is consistent with the observed kinetics, as it could lead to the first-order dependence in imidazole up to high [ImH₀] provided the equilibrium constant in the first step is small.⁸⁹ The second feature that makes it attractive for interpreting our results is that such a mechanism allows imidazole to “search” for the correct orientation prior to reaction, which could explain why linker exchange in DMSO is so resistant to crystalline phase changes at long reaction times. Unlike for the *proton-assisted dissociation pathway*, in which the intermediate **5** has “lost all memory” of the

orientation of the departed linker,^{88c} the *Eigen-Wilkins pathway* may involve many collisions that fail to result in reaction before the “correct” orientation is obtained, leading to exchange of the linkers with preservation of the **sod** topology.

Questions remain as to the nature of activation in the interchange step,⁸⁸ however these are not kinetically distinguishable by our experiments.⁹⁰ Thus we will not speculate on rigorous classification at the expense of the main goal, which is to understand the *kinetic properties*^{88c} of ZIF-8 linker exchange in DMSO. These are (1) a rate that is first-order in imidazole at all [ImH₀], (2) evidence against the existence of a missing linker intermediate, despite DMSO’s ability to stabilize Zn(II), and (3) a unique ability (among the solvents tested) to preserve the **sod** topology at long reaction times even with moderately rapid rates of exchange at high [ImH₀]. The *Eigen-Wilkins pathway* proposed above satisfactorily accounts for these empirical observations. The generality of this mechanism means that it could likely occur for other solvents; however, by the electrical circuit analogy to chemical reactions,⁹² exchange in those solvents will likely prefer to follow the “path of least resistance”, which is the faster *proton-assisted dissociation pathway*.

3.10 Insight into the unique behavior of water

Finally, the most striking discovery in this study was the remarkable rate enhancement that we observed for linker exchange in water. To get a better sense for the magnitude of these rate enhancements, we needed to get rate constants for a different solvent at 4 °C. The slow rates observed in solvents other than water at 4 °C precluded direct measurement at these temperatures. Therefore, we calculated k_{obs} for linker exchange reactions in BuOH at 4 °C by extrapolating from an Eyring plot obtained in

BuOH at $[\text{ImH}_0] = 0.0735 \text{ M}$ (Figure 3-14).⁹³ Compared to linker exchange rates in water ($k_{\text{obs}} = 5.8 \times 10^{-5} \text{ s}^{-1}$ at 4 °C, $t_{1/2}$ of 3 h), the reaction rates in BuOH ($k_{\text{obs}} = 6.5 \times 10^{-7} \text{ s}^{-1}$ at 4 °C, $t_{1/2}$ of 12 d) are predicted to be over two orders of magnitude slower! This dramatic rate enhancement and the normal kinetic isotope effect of 1.5 are both consistent with the *proton-assisted dissociation pathway*, in which the linker exchange reaction benefits from anion stabilization and/or proton shuttling reactions, both of which are superior in water.

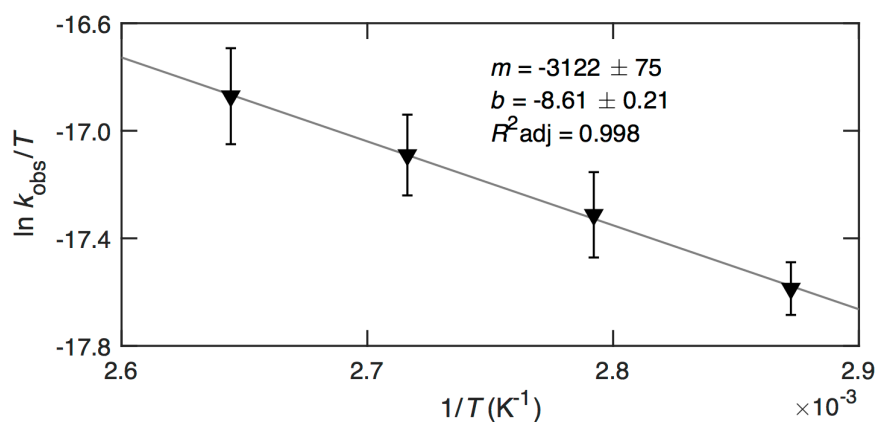
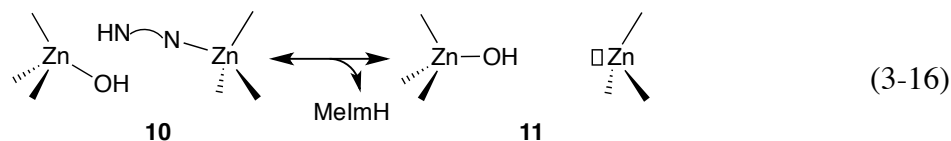
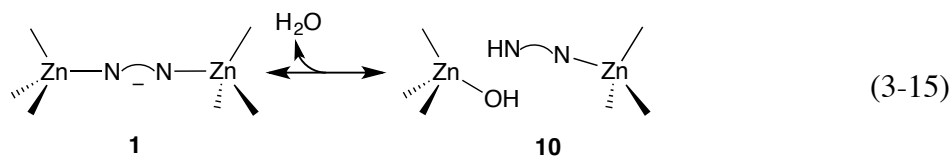


Figure 3-14. Eyring plot used to estimate k_{obs} at 4 °C in *n*-butanol with $[\text{ImH}_0]$ of 0.0735 M. Experimental rates were measured at 75–105 °C, and a linear fit was used to extrapolate to 4 °C. Error bars indicate the 99 % confidence interval. Uncertainty in the slope and y-intercept come from the standard error of the fitting coefficients in the least squares linear regression

The other noteworthy behavior of water in this study was the significant dye encapsulation that persisted even in the presence of free ligand, unlike for any other solvent. This behavior suggests that the *missing linker intermediate* necessary for encapsulation may be particularly stable in water. A compelling explanation for this effect comes from a variant on **5**, the *hydroxyl-terminated missing linker intermediate* (**11** in eq. 3-16)). This species, a point defect⁹⁴ formed from the hydrolysis of **1** in the bulk of the crystal (eq. (3-15) to (3-16)), has been spectroscopically observed following the

exposure of ZIF-8 to water.⁹⁵ It has also been computationally characterized,⁹⁶ and similar species have been invoked for the external crystal surface.⁹⁷ The apparent high stability of this species⁹⁶ means that it is likely to form during our reactions in water. The high stability of **11** could cause this intermediate to be exceptionally long-lived during linker exchange reactions compared to the less stable solvent-terminated **5**, thus allowing **11** to build up in concentration even at moderate [MeImH]. Consequently, this build up of **11** could explain the greater encapsulation of R6G in the pores of ZIF-8 in reactions in water.



Just because **11** can be observed, however, does not mean that it is kinetically relevant for the linker substitution reaction with imidazole. We cannot at present distinguish whether pathways involving **11** contribute much to the overall rate of linker exchange. Nevertheless, we bring up the pathway for two important reasons. First, a defect-driven mechanism (involving **11**) for MOF linker exchange in ZIFs was recently proposed by Zhang et al.,⁹⁶ a claim that we can now analyze in light of new experimental findings. Second, the hypothetical reaction pathway involving **11**, the *-OH missing linker defect pathway* (Figure 3-15), is striking because it involves entry of water in the first step and regeneration of water in the final step. In other words, it forms a catalytic cycle with water as the catalyst.

The catalytic character of the proposed *-OH missing linker defect pathway* for reactions in water along with the extremely rapid kinetics of linker exchange in water bring up an unsettling possibility: could catalytic amounts of water in the organic solvents be responsible for the observed kinetic behavior? Water is of course a common impurity in many organic solvents. To test this possibility, we measured linker exchange kinetics under anhydrous conditions in MeCN. We observed no difference within experimental uncertainty between the conversions obtained in anhydrous MeCN and the values used to obtain the k_{obs} vs. $[ImH_0]$ plots (Figure AI-4). Therefore, if the *-OH missing linker defect pathway*, is kinetically relevant to the overall rate, it requires some of the bulk properties of water, and not merely catalytic action by single water molecules. Consequently, we can conclude that trace quantities of water present in many of the organic solvents tested were not responsible for the observed kinetics; which furthermore suggests that, while the defect-driven mechanism⁹⁶ could be kinetically relevant for linker exchange of ZIFs in water, it is not kinetically significant for linker exchange reactions in organic solvents.

Linker substitution kinetics in these solvents can more coherently be understood in terms of the *proton-assisted dissociation pathway* for water, MeOH, EtOH, BuOH, and MeCN and the *Eigen-Wilkins pathway* for DMSO. Reaction schemes of these proposed pathways are given in Figure 3-15, along with the *-OH missing linker defect pathway* for water that is important for guest molecule encapsulation, but that is not necessarily kinetically relevant for linker substitution. While our mechanistic model, like all such models, is a simplified view of reality and must be subject to revision if conflicting empirical facts come to light, the hypothesized pathways in Figure 3-15 are consistent all

of our empirical kinetic and structural data for these reactions, and we anticipate that they will be useful in predicting the reactivity of linker exchange in ZIFs. Our deduction of this mechanistic model and, in particular, the resulting insights into the kinetic behavior of the MOF linker exchange reaction of ZIF-8 with imidazole, demonstrates the power of using quantitative rate data to study this important class of reactions.

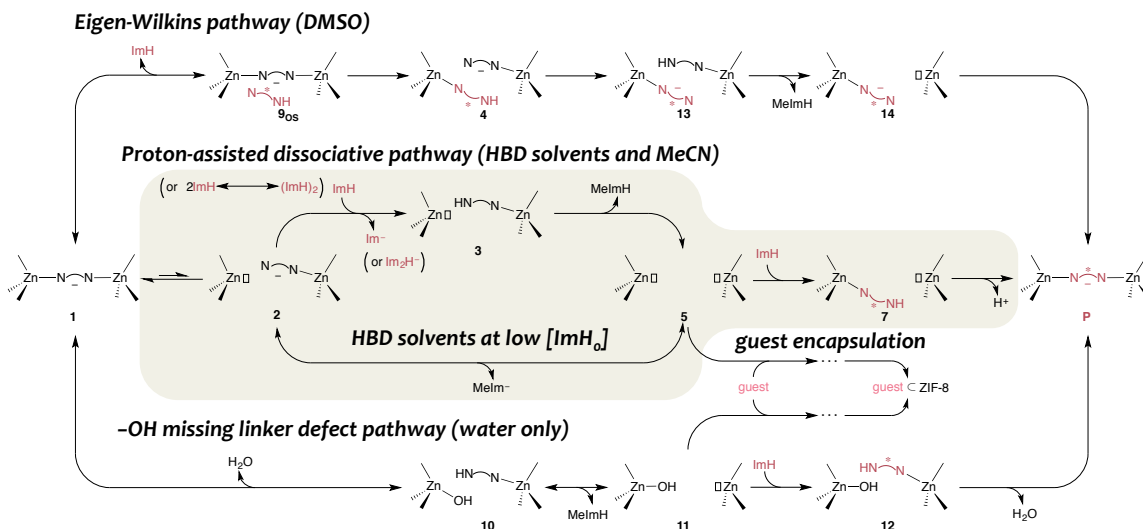


Figure 3-15. A three-pathway mechanism consistent with the experimental data on ZIF-8/*sod*-Zn(MeIm)₂ linker substitution with imidazole (ImH).

3.11 Conclusion

In this study, we have established a reliable protocol to study the kinetics of linker exchange reactions in MOFs. We propose a roadmap for future quantitative MOF ligand exchange studies based on what we have learned in this initial report: (1) ligand incorporation should be measured at long reaction times and at different temperatures to both ensure that conversion is high enough to satisfy the constraints of the method of initial rates and to check for phase transformations by powder XRD, (2) the rate of linker exchange should be measured for MOFs of various particle sizes to establish that

diffusion is not rate-controlling under the conditions. Under ideal circumstances, particles should be chosen for analysis in the range where the observed rate is independent of size and below the transition to diffusion controlled reactions, (3) kinetics for the linker exchange reaction can then be acquired varying the parameters of interest such as ligand concentration, solvent dependence, temperature dependence, etc.

After applying this kinetic methodology to understand the solvent dependence of the linker exchange reaction of ZIF-8 with imidazole, we were able to formulate a mechanism that is consistent with all of the obtained kinetic and structural data. Specifically, our hypothesized mechanism is as follows (Figure 3-15): Solvents that are good hydrogen bond donors (water and MeOH) and solvents that support intermolecular hydrogen bond formation among imidazole (MeCN) facilitate rapid linker substitution in ZIF-8 by opening up a pathway (*proton-assisted dissociation*) that allows for fast exchange. Strong electron pair donor solvents (DMSO) must instead proceed through the slower *Eigen-Wilkins pathway*. Both pathways exhibit at least first-order dependence in imidazole, but the *proton-assisted dissociation pathway* allows for second-order and higher dependence in imidazole. Regarding the exchange reactions at very low concentrations of free linker that allow for appreciable guest encapsulation using select solvents (water, MeOH, EtOH, and BuOH), it seems that this is the same *proton-assisted dissociation pathway* as at high $[\text{ImH}_0]$, but with the solvent molecules as hydrogen bond/proton donor rather than imidazole itself. Linker exchange via the *proton-assisted dissociation pathway* is more rapid, but the slower *Eigen-Wilkins pathway* seems better able to prevent structural rearrangement and crystalline phase change at long reaction times and high values of conversion.

Water is a unique solvent for linker substitution in ZIF-8 for several reasons. First, water supports rapid exchange rates, which are two orders of magnitude faster than BuOH at the same temperature and $[ImH_0]$. Second, water's high encapsulation of dye persists even with moderate concentrations of free ligand, unlike any other solvent tested. This behavior led us to propose a unique exchange pathway in water, the *-OH missing linker defect pathway*, which relies on the peculiar stability of a point defect in ZIF-8 that has been experimentally observed.⁹⁵ The ubiquity of trace water in common organic solvents made it important for us to know if the observed rates of exchange in the other solvents came from catalytic quantities of water in those solvents. Contrary to this notion, anhydrous experiments in MeCN displayed identical conversions to the wet solvent, which indicates that some bulk properties of water are needed to explain the rapid kinetics in that solvent.

Looking to the future of mechanistic studies of linker exchange reactions in MOFs, it will be difficult to get the large quantities of kinetic data required to generalize phenomena to a wide set of MOF types and linkers unless the laborious and material-intensive *ex situ* digestion method can be replaced by suitable *in situ* techniques. We were pleased to see some effort in this area with the recent use of solid-state 2D-¹H-NMR to study a linker exchange reaction in ZIF-8.³⁶ Other possible *in situ* methods include solid state ⁶⁷Zn-NMR^{42,64} and X-ray diffraction.⁹⁸ *Ex situ* analysis of MOF composition is, however, the most unambiguous method of confirming linker exchange, and it will likely continue to compliment the more rapid *in situ* methods. We anticipate that our use of a standard material that can readily be obtained in large quantities could allow our carefully collected set of rate data to be used as a *training set* to validate these more rapid *in situ*

methods. As our understanding of linker exchange reactions in MOFs evolves, linker exchange that arises from MOF metal-ligand bond dynamics may come to be seen as not only a valuable synthetic tool but also a *responsive materials property*, similar to the adsorbate-responsive *breathing* behavior that arises from MOF structural flexibility.⁹⁹ A recent example highlights how this could unfold for MOFs,^{34,100} and we can see clearly the power of metal-ligand bond dynamics for responsive behavior in other materials.^{26e-g,31} For all aspects of MOF research affected by metal-ligand bond dynamics—be it stepwise synthesis, understanding of self-assembly, or responsive properties—we anticipate that the understanding enabled by quantitative kinetics studies of linker exchange will help unleash their full potential in this fascinating class of coordination compounds.

Experimental Methods

General Considerations. Unless otherwise stated, all synthetic procedures were carried out under standard conditions in air on the bench. All solvents were ACS grade solvents, purchased from Fisher (MeOH, EtOH, and BuOH), Sigma Aldrich (MeCN and DMSO), or Cambridge Isotope Laboratories (D₂O, D 99.9 %) and were used without further purification except where specified. Commercial ZIF-8 (Basolite Z1200) was purchased from Aldrich and produced by BASF. Imidazole (99 %) was purchased from Alfa Aesar. 2-methylimidazole (99 %) was purchased from Sigma Aldrich. Methylsulfonylmethane (USP, pharmaceutical secondary standard) was purchased from Sigma Aldrich and produced by Fluka Analytical. Proton nuclear magnetic resonance spectroscopy (¹H-NMR) spectra were recorded on a Varian (Agilent) 600 MHz spectrometer. Powder XRD patterns were acquired on a Bruker D2 PHASER diffractometer.

Kinetic Measurements in Organic Solvents. The kinetic measurements were made using a modification to our previously published method.¹⁸ Stock solutions of 0.588 M imidazole in MeOH, EtOH, BuOH, MeCN, and DMSO were prepared at room temperature. ZIF-8 crystals (15 mg, 65.9×10^{-3} mmol Zn(2-MeIm)₂) were weighed into a 3 mL glass serum vial. An appropriate volume of pure solvent (2.850, 2.625, 2.250, or 1.500 mL, for 0.0294, 0.0735, 0.147, and 0.294 M imidazole, respectively) was added to the vial and solids were suspended by sonication. Upon adding an appropriate volume of 0.588 M imidazole stock solutions (0.150, 0.375, 0.750, or 1.500 mL, for 0.0294, 0.0735, 0.147, and 0.294 M imidazole, respectively), the vial was immediately capped with a PTFE-lined aluminum crimp seal vial, shaken manually, and placed in the aluminum heating block of a Labmate synthesizer thermostated at 70 °C. The reactions were incubated at 70 °C with 450 rpm shaking for a predetermined amount of time. Reactions were run in groups from 4 to 6 separate vials at a time. Conversion values are an average of 3 separate reactions. Reactions were repeated on different days using different stock solutions ensure reproducibility. At the end of the allocated time, the reactions were quenched by immersing the vials in either ice water (BuOH, MeOH, EtOH, and MeCN) or room temperature water (DMSO, to avoid freezing). Suspended solids were rapidly transferred into 15 mL centrifuge tubes and centrifuged at 3300 rpm for 5 min. The solid precipitate was triturated, and the product was re-suspended in fresh methanol (5 mL). The centrifugation and trituration was repeated 3 times with 5 mL of methanol each time. The isolated solids were transferred to pre-weighed glass vials and the residual solvent was removed in a vacuum oven at 100 °C overnight. Yields were not calculated due to losses during transfer steps, but mass recovery values were recorded to determine typical

values (ca. 85 %) and to signal if a given set of conditions fell below the typical values, indicating MOF dissolution. Kinetic measurements for Eyring analysis were carried out in BuOH following the general procedure above, using temperatures of 75, 85, 95, and 105 °C with 0.0735 M imidazole. Conversion was determined following the below procedure and results appear in Figure AI-9 and Table AI-7.

Kinetic Measurements in Water. Reactions in water were conducted at 4 °C in a thermostated cold room. All volumetric measurements were made at room temperature. Firstly, solid ZIF-8 crystals (0.015 g, 65.9×10^{-3} mmol) were weighed into a 1.5 dram glass vial. Then, at room temperature, a volume of deionized water (2.850, 2.625, 2.250, or 1.500 mL, for 0.0294, 0.0735, 0.147, and 0.294 M imidazole, respectively) was pipetted into the vial and the mixture was sonicated until the solid was evenly dispersed (~10 s). A volume of 0.588 M imidazole in water stock solution (0.150, 0.375, 0.750, or 1.500 mL, for 0.0294, 0.0735, 0.147, and 0.294 M imidazole, respectively) was pipetted into a separate small plastic centrifuge tube. The solutions were then transferred to the cold room and allowed to equilibrate at 4 °C for at least 15 min. Upon transferring the imidazole solution, the vials were capped, shaken manually, and placed in the aluminum heating block of a Labmate synthesizer that had equilibrated at 4 °C for at least 2 h. The reactions were incubated at 4 °C with 450 rpm shaking for a predetermined amount of time. To minimize time error, reactions run for less than or equal to 10 min were carried out with only two vials in parallel, while the rest of the reactions were carried out with 4 reactions in parallel. At the end of the allocated time, the reactions were quenched by transferring the suspended solids to 3 mL of methanol at 4 °C, and then washed as described for organic solvents, but with all steps performed at 4 °C. Conversion values

are an average of 3 separate reactions. Reactions were repeated on different days using different stock solutions to ensure reproducibility. The extent of linker incorporation was determined following the below procedure and results appear in Figure AI-6 and Table AI-6.

MOF Digestion and Quantitative ^1H NMR analysis. Methylsulfonylmethane (MSM) was chosen as the internal standard due to its strong resolvable peaks, ease of obtaining in analytical grade, and low hygroscopicity.¹⁰¹ Dried $\text{Zn}(2\text{-MeIm})_{2-x}(\text{Im})_x$ samples were weighed and dispersed in 0.630 mL of 30.0 mM MSM in D_2O to which was added 0.020 mL of 98 % D_2SO_4 leading to digestion of the solids. ^1H NMR (600 MHz, D_2O): δ 8.43 (s, 1H), 7.21 (s, 2H), 7.01 (s, 2H), 2.87 (s, 6H), 2.34 (s, 3H). Representative ^1H NMR spectra are shown in Figure 3-16 and 3-17. The spin-lattice relaxation times (T_1) of each proton in solution were determined by the inversion recovery method for representative samples (Table 3-4 and Figure 3-18) and are given in the order of their line listing: 4.16 (± 0.02) s, 4.25 (± 0.01) s, 3.88 (± 0.02) s, 3.3 (± 0.1) s, 2.81 (± 0.06) s. Changes in sample preparation from our previous study (Chapter 2)¹⁸ were made. Specifically, we used a higher concentration of digested solids, a lower concentration of acid, and MSM instead of tetramethylammonium bromide as internal standard, which resulted in shorter T_1 values, allowing for shorter acquisition parameters. On the basis of the measured T_1 values, spectra were acquired with acquisition time of 4.2 s and an interpulse delay of 16.8 s. The pulse angle was set at the corresponding Ernst angle of 90° and 16 transients were taken per acquisition. The peaks at 8.43 ppm for imidazole and at 2.44 ppm for 2-methylimidazole were least overlapped (Figure 3-16) and were used to calculate conversions, except for exchange in D_2O , where the peak at 7.21 ppm was used due to

H/D exchange at the 2-position of imidazole. The number of spectra per data set for each solvent is 52 (DMSO), 53 (ethanol), 50 (1-butanol), 62 (MeCN), 51 (methanol), and 48 (water). Representative $^1\text{H-NMR}$ spectra given below and all conversion versus time plots are given in Appendix I.

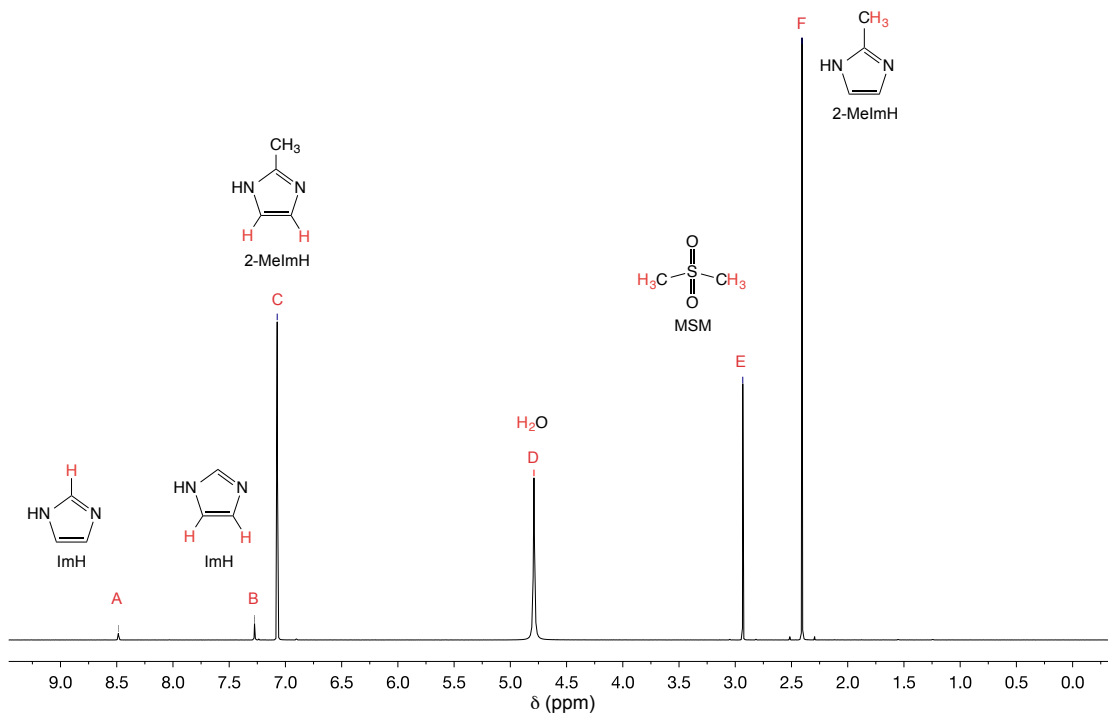


Figure 3-16. A representative $^1\text{H-NMR}$ spectrum from the kinetics measurements showing the peaks used for analysis. The sample shown was run in H_2O at 4°C with $[\text{ImH}] = 0.0735\text{ M}$ and stopped at 20 min.

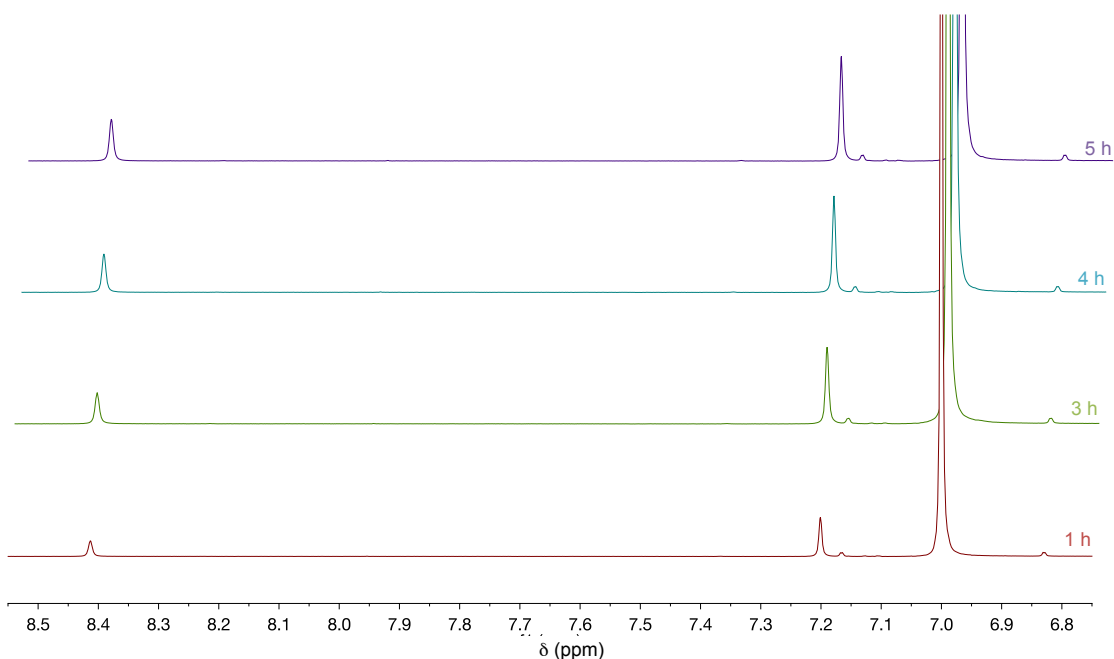


Figure 3-17. Detail of the imidazole protons in the ^1H -NMR spectra for representative samples in a kinetics run. Samples shown are from MeOH with $[\text{ImH}] = 0.0294 \text{ M}$.

T_1 Measurements. The spectra from a spin-lattice relaxation time, T_1 , measurement (entry 3 in Table 3-4) are shown in Figure 3-18. Three T_1 measurements were taken for samples with different values of conversion and are given in Table 3-4. In light of these measurements, the acquisition time (at) was set to 4.2 s and the interpulse delay (d1) was set to 16.8 s ($4 \times \text{at}$).

entry	T_1 values (s)					$\chi_{2-\text{MeIm}}$
	A (1H, Im) 8.5 ppm	B (2H, Im) 7.3 ppm	C (2H, MeIm) 7.1 ppm	E (6H, MSM) 2.9 ppm	F (3 H, MeIm) 2.4 ppm	
1	4.27 ± 0.09	4.7 ± 0.3	3.6 ± 0.2	3.1 ± 0.3	2.7 ± 0.2	0.9616
2	3.76 ± 0.7	4.0 ± 0.1	3.66 ± 0.07	3.2 ± 0.3	2.47 ± 0.04	0.9270
3	4.16 ± 0.02	4.25 ± 0.01	3.88 ± 0.02	3.3 ± 0.1	2.81 ± 0.06	0.9123

Table 3-4. Spin-lattice relaxation time, T_1 , values for samples of digested $\text{Zn}(2-\text{MeIm})_{2-x}(\text{Im})_x$ at various values of conversion.

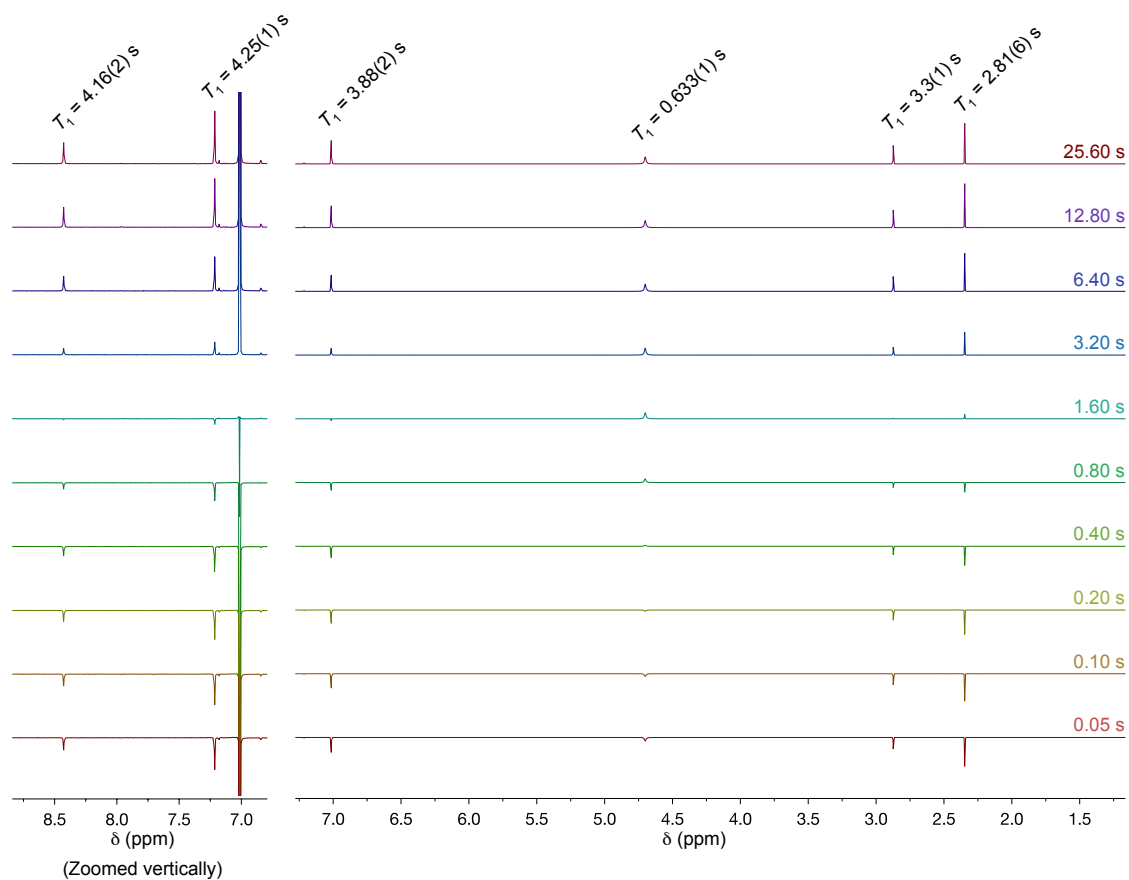


Figure 3-18. ^1H -NMR spectra from a T_1 measurement (entry 3 in Table 3-4) by the inversion recovery method.

Synthesis of R6G@ZIF-8 encapsulation compounds. To a mixture of 75 mg ZIF-8 (0.66 mmol 2-MeIm $^-$) and 79.9 mg (0.15 mmol) Rhodamine-6G (R6G) was added either 15 mL pure solvent or 11.25 solvent + 3.75 mL 0.588 M 2-methylimidazole in solvent for a total [2-methylimidazole] of 0.147 M. The mixture was sonicated, the vial capped, and placed in a 100 °C oven to incubate for 7 days. At the end of reaction, the pink solids were collected by centrifugation at 5k rpm for 10 min after which the supernatant was decanted. The solids were then washed 5 \times in dispersion/centrifugation cycles using 10 mL of 1.4 % (w/w) polyvinylpyrrolidone (MW~29,000) in methanol solution to wash

away surface-adsorbed dye (Chapter 2).¹⁸ The washed R6G@ZIF-8 products were dried in a vacuum oven overnight at 100 °C before weighing.

Digestion UV/Vis absorption measurements: To determine R6G dye loadings, we first digested 10 mg of R6G@ZIF-8 in 2 mL of 1 % (w/w) hydrochloric acid in methanol. The solutions were transferred to glass cuvettes and the absorbance values at 530 nm were converted by direct calibration with standards of R6G in HCl/methanol to wt. % loadings of R6G in ZIF-8.

Synthesis of 85, 125, 240, and 400 nm ZIF-8: The synthesis procedure was adapted from previous reports.^{102,103} A 1.32 M solution of 2-MeImH was prepared by adding 10.837 g MeImH to a volumetric flask and diluting to 0.100 L with deionized water. A 0.01 M cetyltrimethylammonium bromide (CTAB) solution was prepared by adding 0.3645 g of CTAB to a volumetric flask and diluting to 0.100 L with deionized water (dissolves slowly). A 0.024 M Zn(NO₃)₂ solution was prepared by adding 0.7140 g Zn(NO₃)₂·6H₂O to a volumetric flask and diluting to 0.100 L with deionized water. Reactions were carried out in stainless steel autoclaves (Parr) with 45 mL capacity PTFE liners. In a PTFE liner, 17.5 mL of the 1.32 M 2-MeIm solution was combined with variable amounts of the 0.01 M CTAB solution: 1.260 mL (85 nm), 1.008 mL (125 nm), 0.504 mL (240 nm), and 0.252 mL (400 nm). The solutions were then mixed by stirring at 500 rpm for 5 min followed by the addition of 17.5 mL of the 0.024 M Zn(NO₃)₂ solution. Stirring was continued for 5 min, after which the stirbar was removed and the PTFE liner was transferred into the stainless steel autoclave. All of the solutions became cloudy within 2 min after Zn(II) addition, with higher concentrations of CTAB resulting in delayed precipitation. The autoclaves were sealed and left in a 120 °C oven for 6 h.

After cooling, the ZIF-8 crystals and mother liquor were divided into two 45 mL centrifuge tubes to which was added 20 mL of methanol each. The crystals were then collected by centrifugation at 14k rpm for either 30 min (85 and 125 nm) or 15 min (240 and 400 nm). The supernatants were decanted and the solids were consolidated from two tubes into one tube per reaction with 20 mL of fresh methanol. This first wash was then collected by centrifugation at either 14k rpm for 20 min (85 and 125 nm) or 10k rpm for 15 min (240 and 400 nm) and the supernatants were decanted. The washing procedure was then repeated for a second wash with 20 mL fresh methanol. The resulting solids were left to soak overnight in 20 mL fresh methanol in a third wash to allow trapped species such as unreacted 2-MeImH to diffuse out of the microporous crystals. The next day, the particles were collected as before and the supernatants decanted. The products were dried at 70 °C in air. Yields were around 90 % for all four sizes, with representative product weights of 83.7 mg (85 nm), 86.5 mg (125 nm), 83.2 mg (240 nm), and 84.9 mg (400 nm).

Synthesis of 2 μm ZIF-8: The synthesis procedure was followed from our previous report (Chapter 3).¹⁸

Synthesis of 8 μm ZIF-8: The synthesis procedure was followed from a previous report.⁵⁵

References

- (1) Cohen, S. M. The Postsynthetic Renaissance in Porous Solids. *J. Am. Chem. Soc.* **2017**, *139*, 2855–2863.
- (2) Islamoglu, T.; Goswami, S.; Li, Z.; Howarth, A. J.; Farha, O. K.; Hupp, J. T. Postsynthetic Tuning of Metal–Organic Frameworks for Targeted Applications. *Acc. Chem. Res.* **2017**, *50*, 805–813.
- (3) Batten, S. R.; Champness, N. R.; Chen, X.-M.; Garcia-Martinez, J.; Kitagawa, S.; Öhrström, L.; O’Keeffe, M.; Suh, M. P.; Reedijk, J. Terminology of metal–organic frameworks and coordination polymers (IUPAC Recommendations 2013). *Pure Appl. Chem.* **2013**, *85*, 1715–1724.
- (4) (a) Allendorf, M. D. and Stavila, V. Crystal engineering, structure–function relationships, and the future of metal–organic frameworks. *CrystEngComm* **2015**, *17*, 229–246. (b) Czaja, A. U.; Trukhan, N.; Müller, U. Industrial applications of metal–organic frameworks. *Chem. Soc. Rev.* **2009**, *38*, 1284–1293. (c) Silva, P.; Vilela, S. M. F.; Tomé, J. P. C.; Almeida Paz, F. A. Multifunctional metal–organic frameworks: from academia to industrial applications. *Chem. Soc. Rev.* **2015**, *44*, 6774–6803.
- (5) (a) Li, J.-R.; Kuppler, R. J.; Zhou, H.-C. Selective gas adsorption and separation in metal–organic frameworks *Chem. Soc. Rev.* **2009**, *38*, 1477–1504. (b) Van de Voorde, B.; Bueken, B.; Denayer, J.; De Vos, D. Adsorptive separation on metal–organic frameworks in the liquid phase *Chem. Soc. Rev.* **2014**, *43*, 5766–5788. (c) Pimentel, B. R.; Parulkar, A.; Zhou, E.-k.; Brunelli, N. A. Lively, R. P. Zeolitic Imidazolate Frameworks: Next-Generation Materials for Energy-Efficient Gas Separations *ChemSusChem* **2014**, *7*, 3202–3240. (d) Seoane, B.; Coronas, J.; Gascon, I.; Benavides,

M. E.; Karvan, O.; Caro, J.; Kapteijn, F.; Gascon, J. Metal–Organic Framework Based Mixed Matrix Membranes: A Solution for Highly Efficient CO₂ Capture? *Chem. Soc. Rev.* **2015**, *44*, 2421–2454.

(6) (a) Gascon, J.; Corma, A.; Kapteijn, F.; Llabrés i Xamena, F. X. Metal Organic Framework Catalysis: Quo vadis? *Chem. Rev.* **2010**, *110*, 4606–4655. (b) Liu, J.; Chen, L.; Cui, H.; Zhang, J.; Zhang, L.; Su, C.-Y. Applications of metal–organic frameworks in heterogeneous supramolecular catalysis *Chem. Soc. Rev.* **2014**, *43*, 6011–6061.

(7) (a) Rocca, J. D.; Liu, D.; Lin, W. Nanoscale Metal–Organic Frameworks for Biomedical Imaging and Drug Delivery *Acc. Chem. Res.* **2011**, *44*, 957–968. (b) Sun, C.-Y.; Qin, C.; Wang, X.-L.; Su, Z.-M. Metal-organic frameworks as potential drug delivery systems *Expert Opin. Drug Delivery* **2013**, *10*, 89–101.

(8) (a) Hughes, J. T.; Bennett, T. D.; Cheetham, A. K.; Navrotsky, A. Thermochemistry of Zeolitic Imidazolate Frameworks of Varying Porosity *J. Am. Chem. Soc.* **2013**, *135*, 598–601. (b) Wu, D. and Navrotsky, A. Thermodynamics of metal-organic frameworks *J. Solid State Chem.* **2015**, *223*, 53–58.

(9) Structural bond reversibility is general to self-ordered systems (refs [10,11]), and its relevance to MOFs was recognized from the first proposal of these materials (p. 1547 in ref [12]). MOF self-assembly is not fully understood, but studies of it (refs [13]), confirm the importance of bond reversibility for error correction.

(10) Cook, T. R.; Zheng, Y.-R.; Stang, P. J. Metal–Organic Frameworks and Self-Assembled Supramolecular Coordination Complexes: Comparing and Contrasting the Design, Synthesis, and Functionality of Metal–Organic Materials *Chem. Rev.* **2013** *113*, 734–777.

- (11) Lehn, J.-M. From supramolecular chemistry towards constitutional dynamic chemistry and adaptive chemistry *Chem. Soc. Rev.* **2007**, *36*, 151–160.
- (12) Hoskins, B. F. and Robson, R. Design and Construction of a New Class of Scaffolding-like Materials Comprising Infinite Polymeric Frameworks of 3D-Linked Molecular Rods. A Reappraisal of the $\text{Zn}(\text{CN})_2$ and $\text{Cd}(\text{CN})_2$ Structures and the Synthesis and Structure of the Diamond-Related Frameworks $[\text{N}(\text{CH}_3)_4][\text{Cu}^{\text{I}}\text{Zn}^{\text{II}}(\text{CN})_4]$ and $\text{Cu}^{\text{I}}[4,4',4'',4'''\text{-tetracyanotetraphenylmethane}]\text{BF}_4 \cdot x\text{C}_6\text{H}_5\text{NO}_2$. *J. Am. Chem. Soc.* **1990**, *112*, 1546–1554.
- (13) (a) Staviski, E.; Goesten, M.; Juan-Alcañiz, J.; Martinez-Joaristi, A.; Serra-Crespo, P.; Petukhov, A. V.; Gascon, J.; Kapteijn, F. Kinetic Control of Metal–Organic Framework Crystallization Investigated by Time-Resolved In Situ X-Ray Scattering *Angew. Chem., Int. Ed.* **2011**, *50*, 9624–9628. (b) Wu, Y.; Breeze, M. I.; Clarkson, G. J.; Millange, F.; O'Hare, D.; Walton, R. I. Exchange of Coordinated Solvent During Crystallization of a Metal–Organic Framework Observed by In Situ High-Energy X-ray Diffraction *Angew. Chem. Int. Ed.* **2016**, *55*, 4992–4996. (c) Feng, D.; Wang, K.; Wei, Z.; Chen, Y.-P.; Simon, C. M.; Arvapally, R. K.; Martin, R. L.; Bosch, M.; Liu, T.-F.; Fordham, S.; Yuan, D.; Omary, M. A.; Haranczyk, M.; Smit, B.; Zhou, H.-C. Kinetically tuned dimensional augmentation as a versatile synthetic route towards robust metal–organic frameworks *Nat. Commun.* **2014**, *5*, 5723. (d) Cravillon, J.; Nayuk, R.; Springer, S.; Feldhoff, A.; Huber, K.; Wiebcke, M. Controlling Zeolitic Imidazolate Framework Nano- and Microcrystal Formation: Insight into Crystal Growth by Time-Resolved In Situ Static Light Scattering *Chem. Mater.* **2011**, *23*, 2130–2141. (e) Saha, S.; Springer, S.; Schweinefuß, M. E.; Pontoni, D.; Wiebcke, M.; Huber, K. Insight into Fast

Nucleation and Growth of Zeolitic Imidazolate Framework-71 by In Situ Time-Resolved Light and X-ray Scattering Experiments. *Cryst. Growth. Des.* **2016**, *16*, 2002–2010.

(14) (a) Deria, P.; Mondloch, J. E.; Karagiari, O.; Bury, W.; Hupp, J. T.; Farha, O. K. Beyond post-synthesis modification: evolution of metal–organic frameworks via building block replacement *Chem. Soc. Rev.* **2014**, *43*, 5896–5912. (b) Brozek, C. K. and Dincă, M. Cation exchange at the secondary building units of metal–organic frameworks *Chem. Soc. Rev.* **2014**, *43*, 5456–5467. (c) Han, Y.; Li, J.-R.; Xie, Y.; Guo, G. Substitution reactions in metal–organic frameworks and metal–organic polyhedra *Chem. Soc. Rev.* **2014**, *43*, 5952–5981. (d) Karagiari, O.; Bury, W.; Mondloch, J. E.; Hupp, J. T.; Farha, O. K. Solvent-Assisted Linker Exchange: An Alternative to the De Novo Synthesis of Unattainable Metal–Organic Frameworks *Angew. Chem. Int. Ed.* **2014**, *53*, 4530–4540.

(15) The historical term for this type of reaction in complexes is *substitution*, saving *exchange* to describe reactions where the entering and leaving group are the same (often isotopically labeled) ligand; however the use of the word *exchange* to describe these reactions in MOFs is already so widespread that a semiotic debate over the best term is likely counterproductive, and thus we will use the term here. The term *metathesis* has become popular (and for good reason) to describe metal-ion exchange reactions in MOFs because the reaction involves a change of partners between the linkers of the MOF and the ligands/anions coordinated to the free metal ion in solution: i.e., $\{M(L)_m\}_\infty + M^*(X)_n \rightarrow \{M^*(L)_m\}_\infty + M(X)_n$. For linker substitution reactions in MOFs, if the linker's free form in solution is protonated, then the reaction would also be accurately described as a metathesis reaction: i.e., $\{M(L)_m\}_\infty + HL^* \rightarrow \{M(L^*)_m\}_\infty + HL$. However, to remain consistent with the literature, and to avoid drawing an accurate but profitless distinction

between MOF linker substitution reactions with protonated ligands (e.g. imidazole) and those with neutral ligands (e.g. 4,4'-bipyridine), we will avoid coining any new terminology.

(16) (a) Karagiari, O.; Bury, W.; Sarjeant, A. A.; Stern, C. L.; Farha, O. K.; Hupp, J. T. Synthesis and characterization of isostructural cadmium zeolitic imidazolate frameworks via solvent-assisted linker exchange *Chem. Sci.* **2012**, *3*, 3256–3260. (b) Karagiari, O.; Lalonde, M. B.; Bury, W.; Sarjeant, A. A.; Farha, O. K.; Hupp, J. T. Opening ZIF-8: A Catalytically Active Zeolitic Imidazolate Framework of Sodalite Topology with Unsubstituted Linkers *J. Am. Chem. Soc.* **2012**, *134*, 18790–18796. (c) Kim, M.; Cahill, J. F.; Su, Y.; Prather, K. A.; Cohen, S. M. Postsynthetic ligand exchange as a route to functionalization of ‘inert’ metal–organic frameworks *Chem. Sci.* **2012**, *3*, 126–130. (d) Kim, M.; Cahill, J. F.; Fei, H.; Prather, K. A.; Cohen, S. M. Postsynthetic Ligand and Cation Exchange in Robust Metal–Organic Frameworks *J. Am. Chem. Soc.* **2012**, *134*, 18082–18088. (e) Fei, H.; Cahill, J. F.; Prather, K. A.; Cohen, S. M. Tandem Postsynthetic Metal Ion and Ligand Exchange in Zeolitic Imidazolate Frameworks *Inorg. Chem.* **2013**, *52*, 4011–4016. (f) Pullen, S.; Fei, H.; Orthaber, A.; Cohen, S.; Ott, S. Enhanced Photochemical Hydrogen Production by a Molecular Diiron Catalyst Incorporated into a Metal–Organic Framework *J. Am. Chem. Soc.* **2013**, *135*, 16997–17003. (g) Gross, A. F.; Sherman, E.; Mahoney, S. L.; Vajo, J. J. Reversible Ligand Exchange in a Metal–Organic Framework (MOF): Toward MOF-Based Dynamic Combinatorial Chemical Systems *J. Phys. Chem. A* **2013**, *117*, 3771–3776. (h) Szilágyi, P. Á.; Weinrauch, I.; Oh, H.; Hirscher, M.; Juan-Alcañiz, J.; Serra-Crespo, P.; de Respinis, M.; Trzeźniewski, B. J.; Kapteijn, F.; Geerlings, H.; Gascon, J.; Dam, B.;

Grzech, A.; van de Krol, R.; Geerlings, H. Interplay of Linker Functionalization and Hydrogen Adsorption in the Metal–Organic Framework MIL-101 *J. Phys. Chem. C* **2014**, *118*, 19572–19579. (i) Schweinefuß, M. E.; Springer, S.; Baburin, I. A.; Hikov, T.; Huber, K.; Leoni, S.; Wiebcke, M. Zeolitic imidazolate framework-71 nanocrystals and a novel SOD-type polymorph: solution mediated phase transformations, phase selection via coordination modulation and a density functional theory derived energy landscape *Dalton Trans.* **2014**, *43*, 3528–3536. (j) Liu, X.; Li, Y.; Ban, Y.; Peng, Y.; Jin, H.; Bux, H.; Xu, L.; Caro, J.; Yang, W. Improvement of hydrothermal stability of zeolitic imidazolate frameworks *Chem. Commun.* **2013**, *49*, 9140–9142. (k) Madrahimov, S. T.; Atesin, T. A.; Karagiari, O.; Sarjeant, A. A.; Farha, O. K.; Hupp, J. T.; Nguyen, S. T. Metal–Organic Frameworks Containing (Alkynyl)Gold Functionalities: A Comparative Evaluation of Solvent-Assisted Linker Exchange, de Novo Synthesis, and Post-synthesis Modification *Cryst. Growth Des.* **2014**, *14*, 6320–6324. (l) Liu, T. - F.; Zou, L.; Feng, D.; Chen, Y.-P.; Fordham, S.; Wang, X.; Liu, Y.; Zhou, H.-C. Stepwise Synthesis of Robust Metal–Organic Frameworks via Postsynthetic Metathesis and Oxidation of Metal Nodes in a Single-Crystal to Single-Crystal Transformation *J. Am. Chem. Soc.* **2014**, *136*, 7813–7816. (m) Park, J.; Feng, D. W.; Zhou, H.-C. Dual Exchange in PCN-333: A Facile Strategy to Chemically Robust Mesoporous Chromium Metal–Organic Framework with Functional Groups *J. Am. Chem. Soc.* **2015**, *137*, 11801–11809. (n) Liu, C.; Luo, T.-Y.; Feura, E. S.; Zhang, C.; Rosi, N. L. Orthogonal Ternary Functionalization of a Mesoporous Metal–Organic Framework via Sequential Postsynthetic Ligand Exchange *J. Am. Chem. Soc.* **2015**, *137*, 10508–10511. (o) Lalonde, M. B.; Mondloch, J. E.; Deria, P.; Sarjeant, A. A.; Al-Juaid, S. S.; Osman, O. L.; Farha, O. K.; Hupp, J. T. Selective

Solvent-Assisted Linker Exchange (SALE) in a Series of Zeolitic Imidazolate Frameworks *Inorg. Chem.* **2015**, *54*, 7142–7144. (p) Park, J.; Feng, D.; Zhou, H.-C. Structure-Assisted Functional Anchor Implantation in Robust Metal–Organic Frameworks with Ultralarge Pores *J. Am. Chem. Soc.* **2015**, *137*, 1663–1672. (q) Jiang, J.-Q.; Yang, C.-X.; Yan, X.-P. Postsynthetic ligand exchange for the synthesis of benzotriazole-containing zeolitic imidazolate framework *Chem. Commun.* **2015**, *51*, 6540–6543. (r) Denny, M. S.; Cohen, S. M. In Situ Modification of Metal-Organic Frameworks in Mixed-Matrix Membranes *Angew. Chem., Int. Ed.* **2015**, *54*, 9029–9032. (s) Fei, H.; Pullen, S.; Wagner, A.; Ott, S.; Cohen, S. M. Functionalization of robust Zr(IV)-based metal–organic framework films via a postsynthetic ligand exchange *Chem. Commun.* **2015**, *51*, 66–69. (t) Fei, H. H.; Cohen, S. M. Metalation of a Thiocatechol-Functionalized Zr(IV)-Based Metal–Organic Framework for Selective C–H Functionalization *J. Am. Chem. Soc.* **2015**, *137*, 2191–2194. (u) Marti, A. M.; Tran, D.; Balkus, K. J., Jr. Fabrication of a Substituted Imidazolate Material 1 (SIM-1) membrane using post synthetic modification (PSM) for pervaporation of water/ethanol mixtures *J. Porous Mater.* **2015**, *22*, 1275–1284. (v) Ban, Y.; Peng, Y.; Zhang, Y.; Jin, H.; Jiao, W.; Guo, A.; Wang, P.; Li, Y.; Yang, W. Dual-ligand zeolitic imidazolate framework crystals and oriented films derived from metastable mono-ligand ZIF-108 *Micro. Meso. Mater.* **2016**, *219*, 190–198. (w) Sadakiyo, M.; Kuramoto, T.; Kato, K.; Yamauchi, M. Introduction of an Amino Group on Zeolitic Imidazolate Framework through a Ligand Exchange Reaction. *Chem. Lett.* **2017**, DOI: 10.1246/cl.170323. (x) Takaishi, S.; DeMarco, E. J.; Pellin, M. J.; Farha, O. K.; Hupp, J. T. Solvent-assisted linker exchange (SALE) and post-assembly metallation in porphyrinic metal–organic framework

materials. *Chem. Sci.* **2013**, *4*, 1509–1513. (y) Miera, G. G.; Gómez, A. B.; Chupas, P. J.; Martín-Matute, B.; Chapman, K. W.; Platero-Prats, A. E. Topological Transformation of a Metal–Organic Framework Triggered by Ligand Exchange. *Inorg. Chem.* **2017**, *56*, 4576–4583.

(17) (a) Burnett, B. J.; Barron, P. M.; Hu, C.; Choe, W. Stepwise Synthesis of Metal–Organic Frameworks: Replacement of Structural Organic Linkers *J. Am. Chem. Soc.* **2011**, *133*, 9984–9987. (b) Li, T.; Kozłowski, M. T.; Doud, E. A.; Blakely, M. N.; Rosi, N. L. Stepwise Ligand Exchange for the Preparation of a Family of Mesoporous MOFs *J. Am. Chem. Soc.* **2013**, *135*, 11688–11691. (c) Karagiari, O.; Bury, W.; Tylianakis, E.; Sarjeant, A. A.; Hupp, J. T.; Farha, O. K. Opening Metal–Organic Frameworks Vol. 2: Inserting Longer Pillars into Pillared-Paddlewheel Structures through Solvent-Assisted Linker Exchange *Chem. Mater.* **2013**, *25*, 3499–3503. (d) Xu, Y.; Vermeulen, N. A.; Liu, Y.; Hupp, J. T.; Farha, O. K. SALE-Ing a MOF-Based “Ship of Theseus.” Sequential Building-Block Replacement for Complete Reformulation of a Pillared-Paddlewheel Metal-Organic Framework *Eur. J. Inorg. Chem.* **2016**, *27*, 4345–4348. (e) Szilágyi, P. Á.; Serra-Crespo, P.; Dugulan, I.; Gascon, J.; Geerlings, H.; Dam, B. Post-synthetic cation exchange in the robust metal–organic framework MIL-101(Cr) *CrystEngComm* **2013**, *15*, 10175–10178. (f) Karagiari, O.; Vermeulen, N. A.; Klet, R. C.; Wang, T. C.; Moghadam, P. Z.; Al-Juaid, S. S.; Stoddart, J. F.; Hupp, J. T.; Farha, O. K. Functionalized Defects through Solvent-Assisted Linker Exchange: Synthesis, Characterization, and Partial Postsynthesis Elaboration of a Metal–Organic Framework Containing Free Carboxylic Acid Moieties *Inorg. Chem.* **2015**, *54*, 1785–1790. (g) De, D.; Pal, T. K.; Neogi, S.; Senthilkumar, S.; Das, D.; Gupta, S. S.;

Bharadwaj, P. K. Single-Crystal to Single-Crystal Linker Substitution, Linker Place Exchange, and Transmetalation Reactions in Interpenetrated Pillared–Bilayer Zinc(II) Metal–Organic Frameworks *Chem. Eur. J.* **2016**, *22*, 3387–3396. (h) Liu, C.; Zeng, C.; Luo, T.-Y.; Merg, A. D.; Jin, R.; Rosi, N. L. Establishing Porosity Gradients within Metal–Organic Frameworks Using Partial Postsynthetic Ligand Exchange *J. Am. Chem. Soc.* **2016**, *138*, 12045–12048. (i) Bury, W.; Fairen-Jimenez, D.; Lalonde, M. B.; Snurr, R. Q.; Farha, O. K.; Hupp, J. T. Control over Catenation in Pillared Paddlewheel Metal–Organic Framework Materials via Solvent-Assisted Linker Exchange *Chem. Mater.* **2013**, *25*, 739–744. (j) He, Y.; Shang, J.; Gu, Q.; Li, G.; Li, J.; Singh, R.; Xiao, P.; Webley, P. A. Converting 3D rigid metal–organic frameworks (MOFs) to 2D flexible networks via ligand exchange for enhanced CO₂/N₂ and CH₄/N₂ separation *Chem. Commun.* **2015**, *51*, 14716–14719.

(18) Morabito, J. V.; Chou, L.-Y.; Li, Z.; Manna, C. M.; Petroff, C. A.; Kyada, R. J.; Palomba, J. M.; Byers, J. A.; Tsung, C.-K. Molecular Encapsulation beyond the Aperture Size Limit through Dissociative Linker Exchange in Metal–Organic Framework Crystals *J. Am. Chem. Soc.* **2014**, *136*, 12540–12543.

(19) Han, T.-T.; Yang, J.; Liu, Y.-Y.; Ma, J.-F. Rhodamine 6G loaded zeolitic imidazolate framework-8 (ZIF-8) nanocomposites for highly selective luminescent sensing of Fe³⁺, Cr⁶⁺ and aniline *Micro. Meso. Mater.* **2016**, *228*, 275–288.

(20) Basnayake, S. A.; Tan, K.; Leonard, M.; Chabal, Y.; Balkus, K. J., Jr. Encapsulation of red sulfur chromophores in a zeolitic imidazolate framework (ZIF-8) via solvent assisted linker exchange *Micro. Meso. Mater.* **2016**, *219*, 172–177.

(21) (a) Wilkins, R. G. *Kinetics and Mechanism of Reactions of Transition Metal Complexes*, 2nd ed.; VCH: New York, 1991. (b) Langford, C. H.; Gray, H. B. *Ligand Substitution Processes*; Benjamin: New York, 1965. (c) Atwood, J. D. *Inorganic and Organometallic Reaction Mechanisms*, 2nd ed.; VCH Publishers, Inc.: New York, 1997. (d) Swaddle, T. W. Ligand Substitution Dynamics in Metal Complexes. In *Physical Inorganic Chemistry: Reactions, Processes, and Applications*; Bakac, A., Ed.; Wiley: Hoboken, 2010. (e) Basolo, F. and Pearson, R. G. *Mechanisms of Inorganic Reactions: A Study of Metal Complexes in Solution*, 2nd ed.; Wiley: New York, 1967. (f) Jordan, R. B. *Reaction Mechanisms of Inorganic and Organometallic Systems*, 3rd Ed.; Oxford University Press: New York, 2007.

(22) Inorganic complex chemistry (refs [21] and [23]), organometallic catalysis (ref [24]) metalloenzyme function (refs [25]), supramolecular chemistry (refs [26]), aquatic and soil geochemistry (ref [27]), nanoparticle surface chemistry (ref [28]), solvent extraction (ref [29]), ion exchange (ref [30]), metallopolymer dynamics(ref [31]), and, recently, coordination polymers (ref [32]), and metal-organic frameworks.

(23) Basolo, F. Retrospective on Studies of Ligand Substitution Reactions of Metal Complexes. *Coord. Chem. Rev.* **1990**, *100*, 47–66.

(24) Tolman, C. A. The 16 and 18 Electron Rule in Organometallic Chemistry and Homogeneous Catalysis. *Chem. Soc. Rev.* **1972**, *1*, 337–353.

(25) (a) Clore, G. M.; Omichinski, J. G.; Gronenborn, A. M. Slow Conformational Dynamics at the Metal Coordination Site of a Zinc Finger *J. Am. Chem. Soc.* **1991**, *113*, 4350–4351. (b) Daniel, A. G. and Farrell, N. P. The dynamics of zinc sites in proteins: electronic basis for coordination sphere expansion at structural sites *Metallomics* **2014**, *6*,

2230-2241. (c) Maret, W. and Li, Y. Coordination Dynamics of Zinc in Proteins *Chem. Rev.* **2009**, *109*, 4682–4707. (d) Auf der Heyde, T. P. E. and Nassimbeni, L. R. Reaction Pathways from Structural Data: Dynamic Stereochemistry of Zinc(II) Compounds *Acta Crystallogr. Sect. B* **1984**, *40*, 582–590. (e) David, S. S.; and Meggers, E. Inorganic Chemical Biology: from small metal complexes in biological systems to metallo-proteins. *Curr. Opin. Chem. Biol.* **2008**, *12*, 194–196.

(26) (a) Zheng, Y.-R. and Stang, P. J. Direct and Quantitative Characterization of Dynamic Ligand Exchange between Coordination-Driven Self-Assembled Supramolecular Polygons *J. Am. Chem. Soc.* **2009**, *131*, 3487–3489. (b) Sato, S.; Ishido, Y.; Fujita, M. Remarkable Stabilization of $M_{12}L_{24}$ Spherical Frameworks through the Cooperation of 48 Pd(II)–Pyridine Interactions *J. Am. Chem. Soc.* **2009**, *131*, 6064–6065. (c) Li, J.-R.; Zhou, H.-C. Bridging-ligand-substitution strategy for the preparation of metal-organic polyhedra *Nat. Chem.* **2010**, *2*, 893-898. (d) Amendola, V.; Fabrizzi, L.; Pallavicini, P. Controlling the assembling/disassembling process of metal-containing superstructures. *Coord. Chem. Rev.* **2001**, *216*, 435–448. (e) Kruppa, M. and König, B. Reversible Coordinative Bonds in Molecular Recognition. *Chem. Rev.* **2006**, *106*, 3520–3560. (f) Champin, B., Mobian, P., and Sauvage, J.-P. Transition metal complexes as molecular machine prototypes *Chem. Soc. Rev.* **2007**, *36*, 358–366. (g) McConnell, A. J.; Wood, C. S.; Neelakandan, P. P.; Nitschke, J. R. Stimuli-Responsive Metal–Ligand Assemblies. *Chem. Rev.* **2015**, *115*, 7729–7793.

(27) (a) Stumm, W. and Wollast, R. Coordination Chemistry of Weathering: Kinetics of the Surface-Controlled Dissolution of Oxide Minerals. *Rev. Geophys.* **1990**, *28*, 53–69. (b) Wiederhold, J. G.; Kraemer, S. M.; Teutsch, N.; Borer, P. M.; Halliday, A. N.;

Kretzschmar, R. Iron Isotope Fractionation during Proton-Promoted, Ligand-Controlled, and Reductive Dissolution of Goethite. *Environ. Sci. Technol.* **2006**, *40*, 3787–3793. (c) Brown, G. E.; Henrich, V. E.; Casey, W. H.; Clark, D. L.; Eggleston, C.; Felmy, A.; Goodman, D. W.; Grätzel, M.; Maciel, G.; McCarthy, M. I.; Neilson, K. H.; Sverjensky, D. A.; Toney, M. F.; Zachara, J. M. Metal Oxide Surfaces and Their Interactions with Aqueous Solutions and Microbial Organisms. *Chem. Rev.* **1999**, *99*, 77–174. (d) Casey, W. H. and Ludwig, C. The mechanism of dissolution of oxide minerals. *Nature* **1996**, *381*, 506–509. (e) Casey, W. H. Large Aqueous Aluminum Hydroxide Molecules. *Chem. Rev.* **2006**, *106*, 1–16. (f) Casey, W. H. and Swaddle, T. W. Why Small? The use of Small Inorganic Clusters to Understand Mineral Surface and Dissolution Reactions in Geochemistry. *Rev. Geophys.* **2003**, *41*, 1–20. (f) Schott, J.; Pokrovsky, O. S.; Oelkers, E. H. The Link Between mineral Dissolution/Precipitation Kinetics and Solution Chemistry. *Rev. Mineral. Geochem.* **2009**, *70*, 207–258. (g) Lasaga, A. C. Chemical Kinetics of Water-Rock Interactions. *J. Geophys. Res.* **1984**, *89*, 4009–4025. (h) Sigg, L. and Stumm, W. The interaction of anions and weak acids with the hydrous goethite (α -FeOOH) surface *Colloids Surf.* **1981**, *2*, 101–117. (i) Atkinson, R. J.; Posner, A. M.; Quirk, J. P. Kinetics of Isotope Exchange of Phosphate at the α -FeOOH–Aqueous Solution Interface. *J. Inorg. Nucl. Chem.* **1972**, *34*, 2201–2211. (j) Amirbahman, A.; Gfeller, M.; Furrer, G. Kinetics and mechanism of ligand-promoted decomposition of the Keggin Al₁₃ polymer. *Geochim. Cosmochim. Acta* **2000**, *64*, 911–919. (k) Ludwig, C.; Casey, W. H.; Rock, P. A. Prediction of ligand-promoted dissolution rates from the reactivities of aqueous complexes. *Nature* **1995**, *375*, 44–47. (l) Forde, S. and Hynes, M. J. Kinetics and mechanism of the reactions of the Al₁₃ Keggin oligomer,

$[\text{AlO}_4\text{Al}_{12}(\text{OH})_{24}(\text{H}_2\text{O})_{12}]^{7+}$, with a series of phenolic ligands. *New J. Chem.* **2002**, *26*, 1029–1034.

(28) (a) Anderson, N. C.; Hendricks, M. P.; Choi, J. J.; Owen, J. S. Ligand Exchange and the Stoichiometry of Metal Chalcogenide Nanocrystals: Spectroscopic Observation of Facile Metal-Carboxylate Displacement and Binding. *J. Am. Chem. Soc.* **2013**, *135*, 18536–18548. (b) Koscher, B. A.; Bronstein, N. D.; Olshansky, J. H.; Bekenstein, Y.; Alivisatos, A. P. Surface- vs Diffusion-Limited Mechanisms of Anion Exchange in CsPbBr_3 Nanocrystal Cubes Revealed through Kinetic Studies. *J. Am. Chem. Soc.* **2016**, *138*, 12065–12068. (c) De Roo, J.; De Keukeleere, K.; Hens, Z.; Van Driessche, I. From ligands to binding motifs and beyond; the enhanced versatility of nanocrystal surfaces. *Dalton Trans.* **2016**, *45*, 13277–13283. (d) Hostetler, M. J.; Templeton, A. C.; Murray, R. W. Dynamics of Place-Exchange Reactions on Monolayer-Protected Gold Cluster Molecules. *Langmuir* **1999**, *15*, 3782–3789.

(29) (a) Cleare, M. J.; Charlesworth, P.; Bryson, D. J. Solvent extraction in platinum group metal processing. *J. Chem. Technol. Biotechnol.* **1979**, *29*, 210–224. (b) Bernardis, F. L.; Grant, R. A.; Sherrington, D. C. A review of methods of separation of the platinum-group metals through their chloro-complexes. *React. Funct. Polym.* **2005**, *65*, 205–217.

(30) (a) Walton, H. F. Ligand-Exchange Chromatography: A Brief Review. *Ind. Eng. Chem. Res.* **1995**, *34*, 2553–2554. (b) Kurganov, A. Chiral chromatographic separations based on ligand exchange. *J. Chromatogr. A* **2001**, *906*, 51–71. (c) Danankov, V. A.; Semechkin, A. V. Ligand-Exchange Chromatography. *J. Chromatogr. A* **1977**, *141*, 313–353. (d) Siegel, A.; Degens, E. T. Concentration of Dissolved Amino Acids from

Saline Waters by Ligand-Exchange Chromatography. *Science* **1966**, *151*, 1098–1101. (e) Helfferich, F. ‘Ligand Exchange’: a Novel Separation Technique. *Nature* **1961**, *189*, 1001–1002. (f) Liss, I. B. and Murmann, R. K. Complex Ion Kinetics. Reaction Rates on Ion-Exchange Resins Compared to Those in Water. *Inorg. Chem.* **1975**, *14*, 2314–2317.

(31) (a) Yount, W. C.; Loveless, D. M.; Craig, S. L. Small-Molecule Dynamics and Mechanisms Underlying the Macroscopic Mechanical Properties of Coordinatively Cross-Linked Polymer Networks *J. Am. Chem. Soc.* **2005**, *127*, 14488–14496. (b) Fullenkamp, D. E.; He, L.; Barrett, D. G.; Burghardt, W. R.; Messersmith, P. B. Mussel-Inspired Histidine Network Metal Coordination Hydrogels. *Macromolecules* **2013**, *46*, 1167–1174. (c) Mozhdghi, D.; Ayala, S.; Cromwell, O. R.; Guan, Z. Self-Healing Multiphase Polymers via Dynamic Metal–Ligand Interactions *J. Am. Chem. Soc.* **2014**, *136*, 16128–16131. (d) Mozhdghi, D.; Neal, J. A.; Grindy, S. C.; Cordeau, Y.; Ayala, S.; Holten-Andersen, N.; Guan, Z. B. Tuning Dynamic Mechanical Response in Metallopolymer Networks through Simultaneous Control of Structural and Temporal Properties of the Networks. *Macromolecules* **2016**, *49*, 6310–6321. (e) Krogsgaard, M.; Nue, V.; Birkedal, H. Mussel-Inspired Materials: Self-Healing through Coordination Chemistry. *Chem. Eur. J.* **2016**, *22*, 844–857. (f) Lee, B. P.; Narkar, A.; Wilharm, R. Effect of metal ion type on the movement of hydrogel actuator based on catechol-metal ion coordination chemistry. *Sens. Actuators B Chem.* **2016**, *227*, 248–254.

(32) (a) Cui, X.; Khlobystov, A. N.; Chen, X.; Marsh, D. H.; Blake, A. J.; Lewis, W.; Champness, N. R.; Roberts, C. J., Schröder, M. Dynamic Equilibria in Solvent-Mediated Anion, Cation and Ligand Exchange in Transition-Metal Coordination Polymers: Solid-State Transfer or Recrystallisation? *Chem. Eur. J.* **2009**, *15*, 8861–8873. (b) Bradshaw,

D.; Warren, J. E.; Rosseinsky, M. J. Reversible Concerted Ligand Substitution at Alternating Metal Sites in an Extended Solid. *Science* **2007**, *315*, 977–980.

(33) (a) Pan, Y.; Liu, Y.; Zeng, G.; Zhao, L.; Lai, Z. Rapid synthesis of zeolitic imidazolate framework-8 (ZIF-8) nanocrystals in an aqueous system *Chem. Commun.* **2011**, *47*, 2071–2073. (b) Goesten, M. G.; Magusin, P. C. M. M.; Pidko, E. A.; Mezari, B.; Hensen, E. J. M.; Kapteijn, F.; Gascon, J. Molecular Promoting of Aluminum Metal–Organic Framework Topology MIL-101 by *N,N*-Dimethylformamide *Inorg. Chem.* **2014**, *53*, 882–887. (c) Bustamante, E. L.; Fernández, J. L.; Zamaro, J. M. Influence of the solvent in the synthesis of zeolitic imidazolate framework-8 (ZIF-8) nanocrystals at room temperature *J. Colloid Interface Sci.* **2014**, *424*, 37–43. (d) Tian, Y. Q.; Zhao, Y. M.; Chen, Z. X.; Zhang, G. N.; Weng, L. H.; Zhao, D. Y. Design and generation of extended zeolitic metal-organic frameworks (ZMOFs): synthesis and crystal structure of zinc(II) imidazolate polymers with zeolitic frameworks *Chem. Eur. J.* **2007**, *13*, 4146–4154. (e) Shi, Q.; Xu, W.-J.; Huang, R.-K.; Zhang, W.-X.; Li, Y.; Wang, P.; Shi, F.-N.; Li, L.; Li, J.; Dong, J. Zeolite CAN and AFI-Type Zeolitic Imidazolate Frameworks with Large 12-Membered Ring Pore Openings Synthesized Using Bulky Amides as Structure-Directing Agents. *J. Am. Chem. Soc.* **2016**, *138*, 16232–16235.

(34) Morris, R. E. and Čejka, J. Exploiting chemically selective weakness in solids as a route to new porous materials *Nat. Chem.* **2015**, *7*, 381–388.

(35) (a) Solvent-Dependent Cation Exchange in Metal–Organic Frameworks (b) Brozek, C. K.; Dinca, M. *Chem. Commun.* **2015**, *51*, 11780–11782. (c) Brozek, C. K.; Michaelis, V. K.; Ong, T.-C.; Bellarosa, L.; Lopez, N.; Griffin, R. G.; Dinca, M. *ACS Cent. Sci.* **2015**, *1*, 252–260. (d) Brozek, C. K.; Dinca, M. *Chem. Sci.* **2012**, *3*, 2110–2113.

(36) Jayachandrababu, K. C.; Sholl, D. S.; Nair, S. Structural and Mechanistic Differences in Mixed-Linker Zeolitic Imidazolate Framework Synthesis by Solvent Assisted Linker Exchange and *de Novo* Routes. *J. Am. Chem. Soc.* **2017**, Article ASAP, DOI: 10.1021/jacs.7b01660.

(37) (a) Park, K. S.; Ni, Z.; Côté, A. P.; Choi, J. Y.; Huang, R.; Uribe-Romo, F. J.; Chae, H. K.; O’Keeffe, M.; Yaghi, O. M. Exceptional chemical and thermal stability of zeolitic imidazolate frameworks *Proc. Natl. Acad. Sci. USA* **2006**, *103*, 10186–10191. (b) Huang, X.-C.; Lin, Y.-Y.; Zhang, J.-P.; Chen, X.-M. Ligand-Directed Strategy for Zeolite-Type Metal–Organic Frameworks: Zinc(II) Imidazolates with Unusual Zeolitic Topologies *Angew. Chem. Int. Ed.* **2006**, *45*, 1557–1559. (c) Richter, I.; Schubert, M.; Müller, U. Germany Patent WO2007131955 A1, Nov. 22, 2007.

(38) (a) Zhang, J.-P.; Zhang, Y.-B.; Lin, J.-B.; Chen, X.-M. Metal Azolate Frameworks: From Crystal Engineering to Functional Materials *Chem. Rev.* **2012**, *112*, 1001–1033. (b) Phan, A.; Doonan, C. J.; Uribe-Romo, F. J.; Knobler, C. B.; O’Keeffe, M.; Yaghi, O. M. Synthesis, Structure, and Carbon Dioxide Capture Properties of Zeolitic Imidazolate Frameworks *Acc. Chem. Res.* **2010**, *43*, 58–67.

(39) Several ligands have been exchanged into **sod**-Zn(MeIm)₂: imidazole (ref [16b]), 2-ethylimidazole (ref [16e]), 5,6-dimethylbenzimidazole (ref [16j]), 4,5-dichloroimidazole (ref [16i]), 4-methyl-5-imidazolecarboxaldehyde (ref [16u]), and 2-(dimethylaminomethyl)imidazole (ref [16w]). **sod**-Zn(MeIm)₂ has been obtained from ligand exchange of other ZIFs: **sod**-Zn(Im)₂ (ref [16b]) and **sod**-Zn(2-nitroimidazolato)₂ (ref [16v]).

(40) Ni, Z.; Afeworki, M.; Weston, S. C.; Zengel, J.; Stern, D. J. Linker Exchange in Zeolitic Imidazolate Frameworks U.S. Patent 8,920,541 B2, Dec. 30, 2014.

(41) The nomenclature of ImH to represent neutral imidazole was chosen to eliminate confusion between imidazole in its neutral form in solution (ImH) and its deprotonated, anionic bridging mode in the MOF (Im⁻).

(42) Sutrisno, A.; Terskikh, V. V.; Shi, Q.; Song, Z.; Dong, J.; Ding, S. Y.; Wang, W.; Provost, B. R.; Daff, T. D.; Woo, T. K.; Huang, Y. Characterization of Zn-Containing Metal–Organic Frameworks by Solid-State ⁶⁷Zn NMR Spectroscopy and Computational Modeling. *Chem. Eur. J.* **2012**, *18*, 12251–12259.

(43) Bold, three-letter codes before the chemical formula designate the framework topology, e.g. **sod**-Zn(MeIm)₂ for sodalite. For topology definitions, see the RCSR database for MOFs: (a) O'Keeffe, M.; Peskov, M. A.; Ramsden, S. J.; Yaghi, O. M. *Accts. Chem. Res.* **2008**, *41*, 1782–1789. and the IZA database for zeolites: (b) Ch. Baerlocher and L.B. McCusker, Database of Zeolite Structures: <http://www.iza-structure.org/databases/>

(44) Boyd, G. E.; Schubert, J.; Adamson, A. W. The Exchange Adsorption of Ions from Aqueous Solutions by Organic Zeolites. I. Ion-exchange Equilibria. *J. Am. Chem. Soc.* **1947**, *69*, 2818–2829.

(45) Solid-liquid exchange kinetics are rarely so simple. The exchangeable sites in solids are typically more heterogeneous (refs [27], [49b], and [49c]), but the high symmetry of MOFs allows this analysis to be valid. Some MOFs (i.e. ZIF-4/**cag**-Zn(Im)₂ (ref [42])) have distinct chemical environments for even the same type of linker molecule.

- (46) Laidler, K. J. *Chemical Kinetics*, 3rd ed.; Harper & Row, Publishers, Inc.: New York, 1987.
- (47) (a) Helfferich, F. G. Systematic Approach to Elucidation of Multistep Reaction Networks. *J. Phys. Chem.* **1989**, *93*, 6676–6681. (b) Helfferich, F. G. Kinetics of Homogeneous Multistep Reactions. In *Comprehensive Chemical Kinetics*; Compton, R. G. and Hancock, G., Ed.; Elsevier Science: Amsterdam, 2001; Vol 38.
- (48) (a) Thiele, E. W. The Effect of Grain Size on Catalyst Performance. *Am. Sci.* **1967**, *55*, 176–184. (b) Satterfield, C. N. *Mass Transfer in Heterogeneous Catalysis*; M.I.T. Press: Cambridge, 1970. (c) Klemm, E.; Köstner, M.; Emig, G. Transport Phenomena and Reaction in Porous Media. In *Handbook of Porous Solids*; Schüth, F.; Sing, K. S. W.; Weitkamp, J., Ed.; Wiley-VCH: Darmstadt, 2002; Vol. 4; pp. 2174–2219. (d) Kärger, J.; Ruthven, D. M.; Theodorou, D. N. *Diffusion in Nanoporous Materials*; Wiley-VCH Verlag GmbH & Co. KGaA: Darmstadt, 2012; Vol. 2; pp. 807–837.
- (49) (a) Weisz, P. B. and Goodwin, R. D. Combustion of carbonaceous deposits within porous particles. *J. Catal.* **1963**, *2*, 397. (b) Helfferich, F. Ion-Exchange Kinetics. V. Ion Exchange Accompanied by Reactions. *J. Phys. Chem.* **1965**, *69*, 1178–1187. (c) Dana, P. R. and Wheelock, T. D. Kinetics of a Moving Boundary Ion-Exchange Process. *Ind. Eng. Chem. Fundam.* **1974**, *13*, 20–26. (d) Helfferich, F. G. Models and Physical Reality in Ion-Exchange Kinetics. *React. Polym.* **1990**, *13*, 191–194.
- (50) Liberti, L.; Petruzzelli, D.; Boghetich, G.; Passino, R. Diffusion versus Chemically Controlled Kinetics in a Selective System. The $\text{Cl}^-/\text{SO}_4^{2-}$ Exchange. *React. Polym.* **1984**, *2*, 111–116.

(51) (a) Ishida, M. and Wen, C. Y. Comparison of Kinetic and Diffusional Models for Solid-Gas Reactions *AIChE J.* **1968**, *14*, 311–317. (b) Wen, C. Y. Noncatalytic Heterogeneous Solid Fluid Reaction Models. *Ind. Eng. Chem.* **1968**, *60*, 34–54. (c) Yoshida, H.; Kataoka, T.; Fujikawa, S. Kinetics in a Chelate Ion Exchanger—I. Theoretical Analysis. *Chem. Eng. Sci.* **1986**, *41*, 2517–2524. (d) Petruzzelli, D.; Helfferich, F. G.; Liberti, L.; Millar, J. R.; Passino, R. Kinetics of Ion Exchange with Intraparticle Rate Control: Models Accounting for Interactions in the Solid Phase. *React. Polym.* **1987**, *7*, 1–13.

(52) In this context, we mean 10 % past the y-intercept. The crystal surface contains coordination environments that are not representative of the bulk, and this is reflected in the nonzero y-intercepts of conversion versus time plots (see SI, pp. 40–42).

(53) (a) Kondo, M.; Furukawa, S.; Hirai, K.; Kitagawa, S. Coordinatively Immobilized Monolayers on Porous Coordination Polymer Crystals. *Angew. Chem. Int. Ed.* **2010**, *49*, 5327–5330.

(b) Yanai, N. and Granick, S. Directional Self-Assembly of a Colloidal Metal–Organic Framework. *Angew. Chem. Int. Ed.* **2012**, *51*, 5638–5641.

(54) This analysis assumes that k does not vary by more than D . Corrected diffusivities (D_0) of these solvents in ZIF-8, from water (3 Å) to BuOH (5 Å), span 5 orders of magnitude (see ref. [55]), whereas our observed exchange rates (for the same $[\text{ImH}_0]$) vary no more than 2 orders of magnitude.

(55) Zhang, K.; Lively, R. P.; Zhang, C.; Chance, R. R.; Koros, W. J.; Sholl, D. S.; Nair, S. Exploring the Framework Hydrophobicity and Flexibility of ZIF-8: From Biofuel Recovery to Hydrocarbon Separations *J. Phys. Chem. Lett.* **2013**, *4*, 3618–3622.

(56) The somewhat slower kinetics of the commercial material relative to crystals with a similar grain diameter (off the line in Figure 3-5) may come from the abundance of intergrown crystallites in the sample, causing lower exposed surface area than equivalent size-controlled samples, which consist of isolated crystal grains (Appendix IV), or it may come from the commercial material's bimodal size distribution (Figure 3-6). Notably, the exchange rate of the Basolite Z1200 sample is more in line with its crystal grain D50 of 265 nm as measured by TEM rather than its particle size (4.9 μm) given by the manufacturer. Dynamic light scattering (DLS) analysis of the same BASF material suggest a volume-weighted particle size distribution centered around 1 μm , which would put Basolite Z1200 on the curve in Figure 3-5. See: Emily Shearier, Peifu Cheng, Zhuan Zhu, Jiming Bao, Yun Hang Hu, Feng Zhao Surface deflection reduces cytotoxicity of Zn(2-methylimidazole)₂ (ZIF-8) without compromising its drug delivery capacity *RSC Adv.* **2016**, *6*, 4128-4135

(57) (a) Tobe, M. L. and Burgess, J. *Inorganic Reaction Mechanisms*; Longman: New York, 1999; pp 334–375. (b) Blandamer, M. J. and Burgess, J. Initial State and Transition State Solvation in Inorganic Reactions. *Coord. Chem. Rev.* **1980**, *31*, 93–121.

(58) Cravillon, J.; Münzer, S.; Lohmeier, S.-J.; Feldhoff, A.; Huber, K.; Wiebcke, M. Rapid Room-Temperature Synthesis and Characterization of Nanocrystals of a Prototypical Zeolitic Imidazolate Framework. *Chem. Mater.* **2009**, *21*, 1410–1412.

(59) In a separate analysis of much longer reaction times (10 d) than those used for kinetics measurements, we observed a phase change from **sod** to **zni** (dense phase isostructural with ZnI₂) that varied in prevalence depending on the identity of the solvent and [imidazole]. The solvents in order of increasing prevalence of the phase change are

DMSO < BuOH < MeCN < EtOH < MeOH < water. Such analysis is reserved for section 3.9; for details see summary in Table 3-3 and Figure 3-13, PXRD patterns in Figures AIII-10 to AIII-15, and discussion on pp 144–151 in Appendix III.

(60) Pearson, R. G.; Gray, H. B.; Basolo, F. Mechanism of Substitution Reactions of Complex Ions. XVI. Exchange Reactions of Platinum(II) Complexes in Various Solvents. *J. Am. Chem. Soc.* **1960**, *82*, 787–792.

(61) The solvent Lewis basicity for Zn(II), an intermediate hard/soft cation, follows the order MeCN < MeOH < water < DMSO, which could be predicted from solvent parameters of Lewis basicity (Table AV-3), e.g. Guttmann donor numbers, and is confirmed experimentally by transfer thermodynamics, ref [62a], and complex equilibria, ref [62b–c].

(62) (a) Gritzner, G. and Hörzenberger, F. Gibbs Energies, Entropies and Enthalpies of Transfer for Divalent Cations to Several Solvents *J. Chem. Soc. Faraday Trans.* **1995**, *91*, 3843–3850. (b) Wöckel, S.; Gałęzowska, J.; Dechert, S.; Meyer-Klaucke, W.; Nordlander, E.; Meyer, F. Zinc Complexes of a Bioinspired Binucleating Ligand Platform – Equilibria in Solution and Structures in the Solid State *Eur. J. Inorg. Chem.* **2012**, 4728–4738. (c) Kano, K.; Kondo, M.; Inoue, H.; Kitagishi, H.; Colasson, B.; Reinaud, O. Calorimetric Study on Coordination of Tridentate Imidazolyl Calix[6]arene Ligands to Zinc Ion in Organic Solvents *Inorg. Chem.* **2011**, *50*, 6353–6360.

(63) (a) Moggach, S. A.; Bennett, T. D.; Cheetham, A. K. The Effect of Pressure on ZIF-8: Increasing Pore Size with Pressure and the Formation of a High-Pressure Phase at 1.47 GPa. *Angew. Chem. Int. Ed.* **2009**, *48*, 7087–7089. (b) Radhakrishnan, D. and Narayana, C. Effect of pore occupancy on the acoustic properties of zeolitic imidazolate framework

- (ZIF)-8: A Brillouin spectroscopic study at ambient and low temperatures. *J. Chem. Phys.* **2015**, *143*:234703. (c) Im, J.; Yim, N.; Kim, J.; Vogt, T.; Lee, Y. High-Pressure Chemistry of a Zeolitic Imidazolate Framework Compound in the Presence of Different Fluids. *J. Am. Chem. Soc.* **2016**, *138*, 11477–11480. (d) Radhakrishnan, D. and Narayana, C. Guest dependent Brillouin and Raman scattering studies of zeolitic imidazolate framework-8 (ZIF-8) under external pressure. *J. Chem. Phys.* **2016**, *144*:134704.
- (64) Sham, S. and Wu, G. Zinc-67 NMR study of tetrahedral and octahedral zinc sites with symmetrical oxygen, nitrogen, and sulfur ligands *Can. J. Chem.* **1999**, *77*, 1782–1787.
- (65) Tkaczuk, M. N. and Lincoln, S. F. A Proton Magnetic Resonance Study of Ligand Exchange on Tetrakis(tetramethyl-thiourea)zinc(II) Ion *Aust. J. Chem.* **1979**, *32*, 1915–1920.
- (66) Lincoln, S. F.; Pisaniello, D.; Spotswood, T. M.; Tcakzuk, M. A phosphorus-31 magnetic resonance study of triphenylphosphine oxide exchange on magnesium(II) and zinc(II). *Aust. J. Chem.* **1981**, *34*, 283–289.
- (67) Eaton, D. R. and Zaw, K. NMR studies of thioureas and their zinc complexes *J. Inorg. Nucl. Chem.* **1976**, *38*, 1007–1010.
- (68) Tkaczuk, M. N. and Lincoln, S. F. A Phosphorus-31 Magnetic Resonance Study of Ligand Exchange on Tetrakis(hexamethylphosphoramidate)zinc(II) Ion *Aust. J. Chem.* **1980**, *33*, 2621–2626.

- (69) Gennaro, M. C. and Mirti, P. NMR study of intramolecular and intermolecular exchange processes in the Zn(II) ion-iminodiacetic acid system *J. Inorg. Nucl. Chem.* **1981**, *43*, 1711–1717.
- (70) Auf der Heyde, T. P. E. and Nassimbeni, L. R. Reaction Pathways from Structural Data: Dynamic Stereochemistry of Zinc(II) Compounds *Acta Crystallogr. Sect. B* **1984**, *40*, 582–590.
- (71) Rabenstein, D. L. and Kula, R. J. Ligand-Exchange Kinetics and Solution Equilibria of Cadmium, Zinc, and Lead Nitrilotriacetate Complexes *J. Am. Chem. Soc.* **1969**, *91*, 2492–2503.
- (72) Reed, G. H. and Kula, R. J. Nuclear Magnetic Resonance and Infrared Spectral Studies of Structural and Kinetic Properties of Amino Polycarboxylate Chelates of Divalent Lead, Zinc, Cadmium, and Mercury in Acidic Aqueous Solutions *Inorg. Chem.* **1971**, *10*, 2050–2057.
- (73) (a) Ryde, U. Molecular dynamics simulations of alcohol dehydrogenase with a four- or five-coordinate catalytic zinc ion *Proteins: Struct., Funct., Bioinf.* **1995**, *21*, 40–56. (b) Picot, D.; Ohanessian, G.; Frison, G. The Alkylation Mechanism of Zinc-Bound Thiolates Depends upon the Zinc Ligands *Inorg. Chem.* **2008**, *47*, 8167–8178. (c) Melnick, J. G.; Zhu, G.; Buccella, D.; Parkin, G. J. Thiolate exchange in $[\text{Tm}^{\text{R}}]\text{ZnSR}'$ complexes and relevance to the mechanisms of thiolate alkylation reactions involving zinc enzymes and proteins *Inorg. Biochem.* **2006**, *100*, 1147–1154.
- (74) Consider the dissociative mechanism for the complex in ref [65] and [66] against associative mechanisms in very similar complexes, but with less bulky ligands (ref [67] and ref[68]). Consider also steric differences leading to shifts from dissociative to

associative exchange pathways in Zn(II) chelate complexes on p 1716 in ref [69]. So too we may expect the Zn(ImH)₄ complex in solution, which follows an associative exchange pathway (ref [64]), to shift to a dissociative one when it is made anionic and has added steric bulk with methyl groups at the C2 position in ZIF-8.

(75) See pp 212–213 and 219–232 in ref [21a] and pp 84–86 in ref [21c].

(76) See pp 376–377 in ref [21d], pp 104–106 in ref [21f], and pp 216–223 in ref [21e].

(77) Clarkson, A. J.; Buckingham, D. A.; Rogers, A. J.; Blackman, A. G.; Clark, C. R. Kinetic Origin of the Chelate Effect. Base Hydrolysis, H-Exchange Reactivity, and Structures of *syn,anti*-[Co(cyclen)(NH₃)₂]³⁺ and *syn,anti*-[Co(cyclen)(diamine)]³⁺ Ions (diamine = H₂N(CH₂)₂NH₂, H₂N(CH₂)₃NH₂) *Inorg. Chem.* **2000**, *39*, 4769–4775.

(78) Wang, K.; Lv, X.L.; Feng, D.; Li, J.; Chen, S.; Sun, J.; Song, L.; Xie, Y. B.; Li, J. R.; Zhou, H. C. Pyrazolate-Based Porphyrinic Metal–Organic Framework with Extraordinary Base-Resistance *J. Am. Chem. Soc.* **2016**, *138*, 914–919.

(79) Scheiner, S. and Yi, M. Proton Transfer Properties of Imidazole *J. Phys. Chem.* **1996**, *100*, 9235–9241.

(80) (a) Kozak, A.; Czaja, M.; Chmurzyński, L. Investigations of (acid + base) equilibria in systems modelling interactions occurring in biomolecules *J. Chem. Thermodyn.* **2006**, *38*, 599–605. (b) Pawlak, Z. and Urbańczyz, G. Formation of (NHN₁)⁺ hydrogen bonded cations in acetonitrile *J. Mol. Struct.* **1988**, *177*, 401–406.

(81) Kreider-Mueller, A.; Quinlivan, P. J.; Owen, J. S.; Parkin, G. Synthesis and Structures of Cadmium Carboxylate and Thiocarboxylate Compounds with a Sulfur-Rich Coordination Environment: Carboxylate Exchange Kinetics Involving Tris(2-mercapto-

- 1-*t*-butylimidazolyl)hydroborato Cadmium Complexes, [Tm^{But}]Cd(O₂CR) *Inorg. Chem.* **2015**, *54*, 3835–3850.
- (82) Bordwell, F. G. Equilibrium acidities in dimethyl sulfoxide solution *Acc. Chem. Res.* **1988**, *21* (12), 456–463.
- (83) Wiberg, K. B. The Deuterium Isotope Effect *Chem. Rev.* **1955**, *55*, 713–743.
- (84) (a) Zhang, K.; Zhang, L.; Jiang, J. Adsorption of C₁–C₄ Alcohols in Zeolitic Imidazolate Framework-8: Effects of Force Fields, Atomic Charges, and Framework Flexibility *J. Phys. Chem. C* **2013**, *117*, 25628–25635. (b) Zhang, K.; Lively, R. P.; Dose, M. E.; Brown, A. J.; Zhang, C.; Chung, J.; Nair, S.; Koros, W. J.; Chance, R. R. Alcohol and water adsorption in zeolitic imidazolate frameworks *Chem. Commun.* **2013**, *49*, 3245–3247.
- (85) Gee, J. S. and Sholl, D.S. Characterization of the Thermodynamic Stability of Solvated Metal–Organic Framework Polymorphs Using Molecular Simulations *J. Phys. Chem. C* **2013**, *117*, 20636–20642.
- (86) Akimbekov, Z.; Wu, D.; Brozek, C. K.; Dincă, M.; Navrotsky, A. Thermodynamics of solvent interaction with the metal–organic framework MOF-5. *Phys. Chem. Chem. Phys.* **2016**, *18*, 1158–1162.
- (87) Zhang, C.; Lively, R. P.; Zhang, K.; Johnson, J. R.; Karvan, O.; Koros, W. J. Unexpected Molecular Sieving Properties of Zeolitic Imidazolate Framework-8 *J. Phys. Chem. Lett.* **2012**, *3*, 2130–2134.
- (88) (a) Swaddle, T. W. Activation Parameters and Reaction Mechanism in Octahedral Substitution. *Coord. Chem. Rev.* **1974**, *14*, 217–268. (b) Swaddle, T. W. Operationism, Mechanism, and High Pressure. *Rev. Phys. Chem. Japan* **1980**, *50*, 230–242. (c)

Swaddle, T. W. Substitution Reactions of Divalent and Trivalent Metal Ions. *Adv. Inorg. Bioinorg. Mech.* **1983**, *2*, 95–138. (d) Lay, P. A. Recent Developments on the Mechanisms of Substitution Reactions of Octahedral Coordination Complexes. *Coord. Chem. Rev.* **1991**, *110*, 213–233. (e) Swaddle, T. W. On the Mechanism of Octahedral Substitution. *Comments Inorg. Chem.* **1991**, *12*, 237–258. (f) Lincoln, S. F. and Merbach, A. E. Substitution Reactions of Solvated Metal Ions. *Adv. Inorg. Chem.* **1995**, *42*, 1–88. (g) Lincoln, S. F. Mechanistic Studies of Metal Aqua Ions: A Semi-Historical Perspective. *Helv. Chim. Acta* **2005**, *88*, 523–545.

(89) Jencks, W. P. When Is an Intermediate Not an Intermediate? Enforced Mechanisms of General Acid-Base Catalyzed, Carbocation, Carbanion, and Ligand Exchange Reactions. *Acc. Chem. Res.* **1980**, *13*, 161–169.

(90) Associative (I_a) vs. dissociative (I_d) modes of activation (using Langford and Gray's widely used nomenclature, ref [21b]) could be distinguished as for other systems (refs [88] and [91]). If these studies are undertaken, the effect of strong solvation should be considered (ref [57a]).

(91) Loring, J.; Yu, P.; Phillips, B. L.; Casey, W. H. Activation volumes for oxygen exchange between the $\text{GaO}_4\text{Al}_{12}(\text{OH})_{24}(\text{H}_2\text{O})_{12}^{7+}(\text{aq})$ (GaAl_{12}) polyoxocation and aqueous solution from variable pressure ^{17}O NMR spectroscopy. *Geochim. Cosmochim. Acta* **2004**, *68*, 2791–2798.

(92) Kozuch, S. Steady State Kinetics of Any Catalytic Network: Graph Theory, the Energy Span Model, the Analogy between Catalysis and Electrical Circuits, and the Meaning of “Mechanism” *ACS Catal.* **2015**, *5*, 5242–5255.

(93) This was carried out to extrapolate the temperature dependence of the reaction kinetics. The Eyring equation is only valid for elementary reactions, although *Eyring-type* relationships have been used for multistep pathways. We have not analyzed the calculated activation parameters for this reason. They are 26 kJ mol^{-1} for ΔH^\ddagger and $-270 \text{ J mol}^{-1} \text{ K}^{-1}$ for ΔS^\ddagger .

(94) Sholl, D. S. and Lively, R. P. Defects in Metal-Organic Frameworks: Challenge or Opportunity? *J. Phys. Chem. Lett.* **2015**, *6*, 3437–3444.

(95) Cheng, P. and Hu, Y. H. H₂O-Functionalized Zeolitic Zn(2-methylimidazole)₂ Framework (ZIF-8) for H₂ Storage. *J. Phys. Chem. C* **2014**, *118*, 21866–21872.

(96) Zhang, C.; Han, C.; Sholl, D. S.; Schmidt, J. R. Computational Characterization of Defects in Metal–Organic Frameworks: Spontaneous and Water-Induced Point Defects in ZIF-8 Computational Characterization of Defects in Metal-Organic Frameworks: Spontaneous and Water-Induced Point Defects in ZIF-8 *J. Phys. Chem. Lett.* **2016**, *7*, 459–464.

(97) (a) Chizallet, C.; Lazare, S.; Bazer-Bachi, D.; Bonnier, F.; Lecocq, V.; Soyer, E.; Quoineaud, A.-A.; Bats, N. Catalysis of Transesterification by a Nonfunctionalized Metal-Organic Framework: Acido-Basicity at the External Surface of ZIF-8 Probed by FTIR and *ab Initio* Calculations *J. Am. Chem. Soc.* **2010**, *132*, 12365–12377. (b) Pang, S. H.; Han, C.; Sholl, D. S.; Jones, C. W.; Lively, R. P. Facet-Specific Stability of ZIF-8 in the Presence of Acid Gases Dissolved in Aqueous Solutions. *Chem. Mater.* **2016**, *28*, 6960–6967. (c) Tanaka, S.; Fujita, K.; Miyake, Y.; Miyamoto, M.; Hasegawa, Y.; Makino, T.; Van der Perre, S.; Cousin Saint Remi, J.; Van Assche, T.; Baron, G. V.; Denayer, J. F. M. Adsorption and Diffusion Phenomena in Crystal Size Engineered ZIF-8

- MOF. *J. Phys. Chem. C* **2015**, *119*, 28430–28439. (d) Tian, F.; Cerro, A. M.; Mosier, A. M.; Wayment-Steele, H. K.; Shine, R. S.; Park, A.; Webster, E. R.; Johnson, L. E.; Johal, M. S.; Benz, L. Surface and Stability Characterization of a Nanoporous ZIF-8 Thin Film. *J. Phys. Chem. C* **2014**, *118*, 14449–14456.
- (98) Taddei, M.; Tiana, D.; Casati, N.; van Bokhoven, J. A.; Smit, B.; Ranocchiari, M. Mixed-linker UiO-66: structure-property relationships revealed by a combination of high-resolution powder X-ray diffraction and density functional theory calculations. *Phys. Chem. Chem. Phys.* **2017**, *19*, 1551–1559.
- (99) (a) Horike, S.; Shimomura, S.; Kitagawa, S. Soft porous crystals *Nat. Chem.* **2009**, *1*, 695–704. (b) Schneemann, A.; Bon, V.; Schwedler, I.; Senkowska, I.; Kaskel, S.; Fischer, R. A. Flexible metal–organic frameworks *Chem. Soc. Rev.* **2014**, *43*, 6062–6096. (c) Bennett, T. D.; Fuchs, A. H.; Cheetham, A. K.; Coudert, F.-X. (Eds.) Flexibility and Disorder in Metal-Organic Frameworks [Themed issue] *Dalton Trans.* **2016**, *45*, 4058–4149.
- (100) (a) Allan, P. K.; Xiao, B.; Teat, S. J.; Knight, J. W.; Morris, R. E. In Situ Single-Crystal Diffraction Studies of the Structural Transition of Metal-Organic Framework Copper 5-Sulfoisophthalate, Cu-SIP-3. *J. Am. Chem. Soc.* **2010**, *132*, 3605–3611. (b) Tian, Y.; Allan, P. K.; Renouf, C. L.; He, X.; McCormick, L. J.; Morris, R. E. Synthesis and structural characterization of a single-crystal to single-crystal transformable coordination polymer. *Dalton Trans.* **2014**, *43*, 1519–1523.
- (101) Wells, R. J.; Cheung, J.; Hook, J. M. Dimethylsulfone as a universal standard for analysis of organics by QNMR. *Accred. Qual. Assur.* **2004**, *9*, 450–456.

(102) Pan, Y.; Heryadi, D.; Zhou, F.; Zhao, L.; Lestari, G.; Su, H.; Lai, Z. Tuning the crystal morphology and size of zeolitic imidazolate framework-8 in aqueous solution by surfactants *CrystEngComm*, **2011**, *13*, 6937–6940.

(103) Hu, P.; Zhuang, J.; Chou, L.-Y.; Lee, H. K.; Ling, X. Y.; Chuang, Y.-C.; Tsung, C.-K. Surfactant-Directed Atomic to Mesoscale Alignment: Metal Nano-crystals Encased Individually in Single-Crystalline Porous Nanostructures *J. Am. Chem. Soc.* **2014**, *136*, 10561–10564.

4.0 APPENDIX I

Kinetics plots

Guide to the kinetics plots

The concentration values above the plots are that of exogenous imidazole at the beginning of the reaction. Conversion is expressed on the ordinate as the mole fraction of 2-methylimidazole ($\chi_{2\text{-MeIm}} = \frac{\text{mol } 2\text{-MeIm}}{\text{mol } 2\text{-MeIm} + \text{mol Im}}$) in the mixture of 2-methylimidazole and imidazole in solutions of digested MOF products as determined by $^1\text{H-NMR}$ ($\chi_{2\text{-MeIm}} = 1 - \text{conversion}$). Error bars on the data points are the standard deviations based on three separate reactions and the uncertainties given for the slopes are the standard deviations obtained from linear regression. The linear regressions were performed on the full dataset (i.e. ~ 12 points). Each point is from a separate batch reaction (i.e. no aliquots) and is therefore independent of all the others.

Kinetics measurements in dimethyl sulfoxide

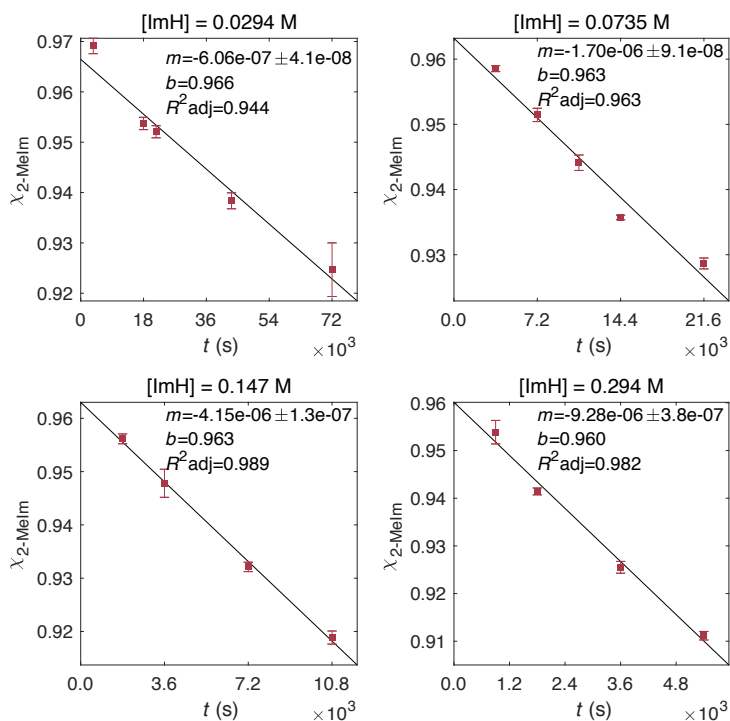


Figure AI-1. Conversion versus time plots used for determining the rate constants of ligand exchange in dimethyl sulfoxide (DMSO) at 70 °C. The black lines are the linear least squares regressions, with slopes equal to $-k_{\text{obs}}$. For reference, $72 \times 10^3 \text{ s} = 20 \text{ h}$ and $3.6 \times 10^3 \text{ s} = 1 \text{ h}$.

0.0294 M			0.0735 M			0.147 M			0.294 M		
t (s)	$\chi_{2\text{-MeIm}}$	s	t (s)	$\chi_{2\text{-MeIm}}$	s	t (s)	$\chi_{2\text{-MeIm}}$	s	t (s)	$\chi_{2\text{-MeIm}}$	s
3600	0.9691	0.0015	3600	0.9586	0.0005	1800	0.9562	0.0009	900	0.9539	0.0025
18000	0.9537	0.0012	7200	0.9515	0.0010	3600	0.9478	0.0026	1800	0.9414	0.0007
21600	0.9521	0.0012	10800	0.9441	0.0012	7200	0.9321	0.0009	3600	0.9255	0.0012
43200	0.9384	0.0016	14400	0.9357	0.0003	10800	0.9189	0.0012	5400	0.9112	0.0009
72000	0.9247	0.0053	21600	0.9287	0.0008						

Table AI-1. Values of mole fraction of 2-methylimidazole, χ_{MeIm} , and uncertainty, expressed as the experimental standard deviation, s , of three reactions, for reactions in DMSO at 70 °C.

Kinetics measurements in ethanol

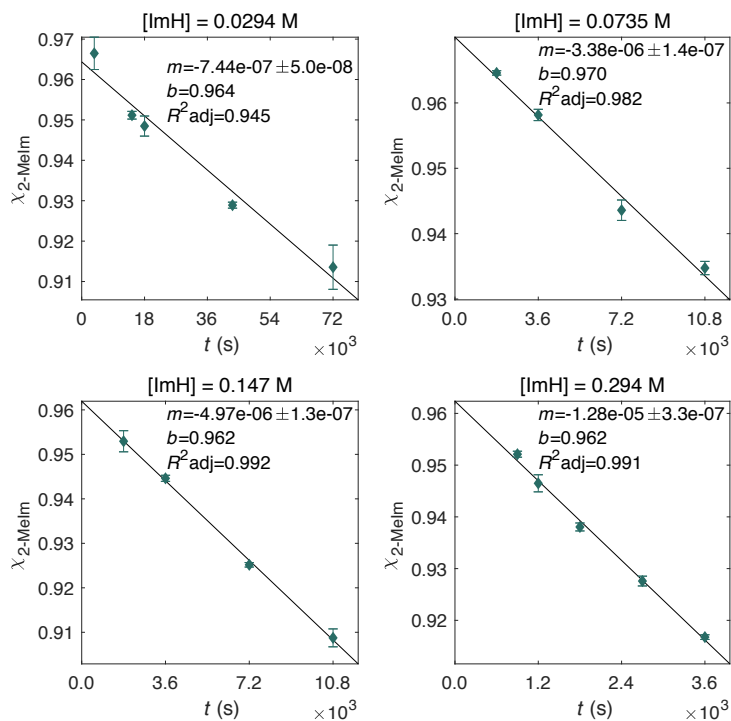


Figure AI-2. Conversion versus time plots used for determining the rate constants of ligand exchange in ethanol at 70 °C. The black lines are the linear least squares regressions, with slopes equal to $-k_{\text{obs}}$. For reference, $72 \times 10^3 \text{ s} = 20 \text{ h}$ and $3.6 \times 10^3 \text{ s} = 1 \text{ h}$.

0.0294 M			0.0735 M			0.147 M			0.294 M		
t (s)	$\chi_{2\text{-Melm}}$	s	t (s)	$\chi_{2\text{-Melm}}$	s	t (s)	$\chi_{2\text{-Melm}}$	s	t (s)	$\chi_{2\text{-Melm}}$	s
3600	0.9665	0.0040	1800	0.9646	0.0003	1800	0.9530	0.0024	900	0.9521	0.0006
14400	0.9512	0.0010	3600	0.9582	0.0009	3600	0.9446	0.0007	1200	0.9465	0.0017
18000	0.9485	0.0025	7200	0.9436	0.0016	7200	0.9252	0.0005	1800	0.9381	0.0008
43200	0.9289	0.0007	10800	0.9347	0.0010	10800	0.9088	0.0020	2700	0.9276	0.0009
72000	0.9135	0.0055							3600	0.9168	0.0005

Table AI-2. Values of mole fraction of 2-methylimidazole, χ_{Melm} , and uncertainty, expressed as the experimental standard deviation, s , of three reactions, for reactions in ethanol at 70 °C.

Kinetics measurements in *n*-butanol

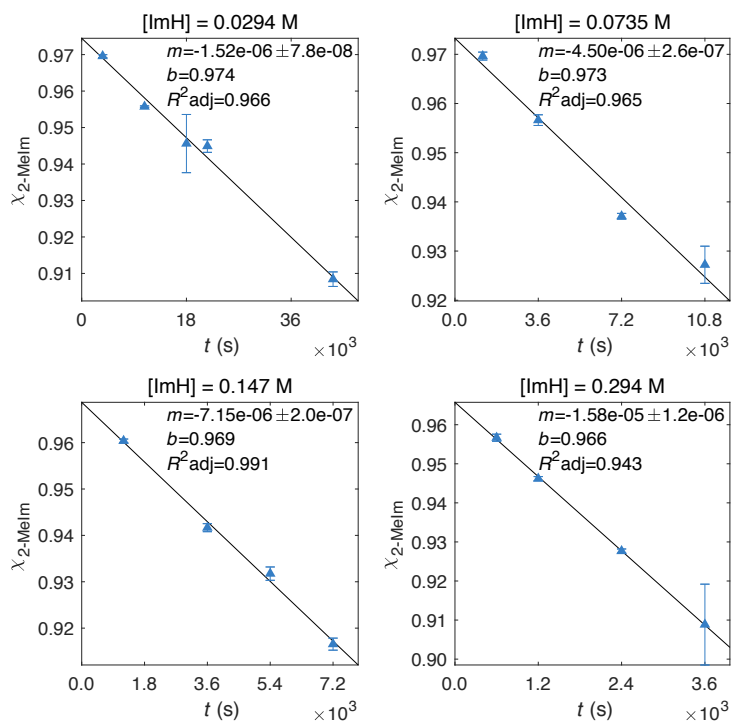


Figure AI-3. Conversion versus time plots used for determining the rate constants of ligand exchange in *n*-butanol at 70 °C. The black lines are the linear least squares regressions, with slopes equal to $-k_{\text{obs}}$. For reference, $3.6 \times 10^3 \text{ s} = 1 \text{ h}$.

0.0294 M			0.0735 M			0.147 M			0.294 M		
t (s)	$\chi_{2\text{-Meim}}$	s	t (s)	$\chi_{2\text{-Meim}}$	s	t (s)	$\chi_{2\text{-Meim}}$	s	t (s)	$\chi_{2\text{-Meim}}$	s
3600	0.9696	0.0004	1200	0.9696	0.0008	1200	0.9604	0.0004	600	0.9567	0.0009
10800	0.9557	0.0002	3600	0.9566	0.0011	3600	0.9417	0.0009	1200	0.9462	0.0005
18000	0.9456	0.0080	7200	0.9371	0.0006	5400	0.9318	0.0014	2400	0.9277	0.0005
21600	0.9449	0.0017	10800	0.9272	0.0038	7200	0.9166	0.0013	3600	0.9089	0.0103
43200	0.9084	0.0020									

Table AI-3. Values of mole fraction of 2-methylimidazole, χ_{Meim} , and uncertainty, expressed as the experimental standard deviation, s , of three reactions, for reactions in *n*-butanol at 70 °C.

Kinetics measurements in acetonitrile

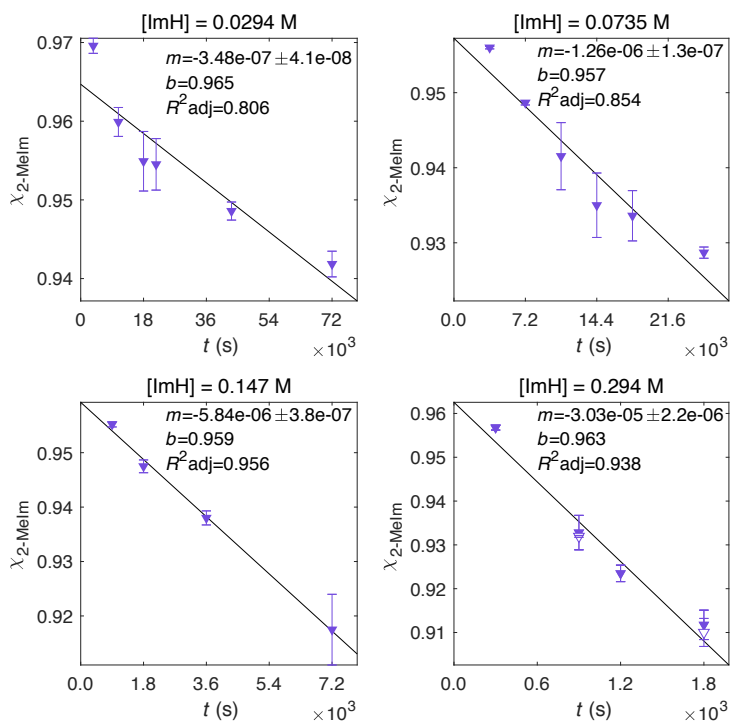


Figure AI-4. Conversion versus time plots used for determining the rate constants of ligand exchange in acetonitrile at 70 °C for ACS grade acetonitrile (filled triangle, \blacktriangledown) or anhydrous acetonitrile (open triangle, ∇ , only in the [imidazole] = 0.294 M plot). The black lines are the linear least squares regressions, with slopes equal to $-k_{\text{obs}}$. For reference, $72 \times 10^3 \text{ s} = 20 \text{ h}$, $21.6 \times 10^3 \text{ s} = 6 \text{ h}$, and $3.6 \times 10^3 \text{ s} = 1 \text{ h}$.

0.0294 M			0.0735 M			0.147 M			0.294 M		
t (s)	$\chi_{2\text{-MeIm}}$	s	t (s)	$\chi_{2\text{-MeIm}}$	s	t (s)	$\chi_{2\text{-MeIm}}$	s	t (s)	$\chi_{2\text{-MeIm}}$	s
3600	0.9696	0.0010	3600	0.9560	0.0002	900	0.9552	0.0005	300	0.9568	0.0005
10800	0.9599	0.0018	7200	0.9487	0.0003	1800	0.9475	0.0012	900	0.9328	0.0039
18000	0.9549	0.0038	10800	0.9415	0.0045	3600	0.9380	0.0013	900 (dry)	0.9319	0.0002
21600	0.9545	0.0033	14400	0.9350	0.0043	7200	0.9175	0.0065	1200	0.9235	0.0019
43200	0.9486	0.0011	18000	0.9336	0.0034				1800	0.9118	0.0034
72000	0.9419	0.0016	25200	0.9287	0.0007				1800 (dry)	0.9100	0.0032

Table AI-4. Values of mole fraction of 2-methylimidazole, χ_{MeIm} , and uncertainty, expressed as the experimental standard deviation, s , of three reactions, for reactions in acetonitrile at 70 °C.

Kinetics measurements in methanol

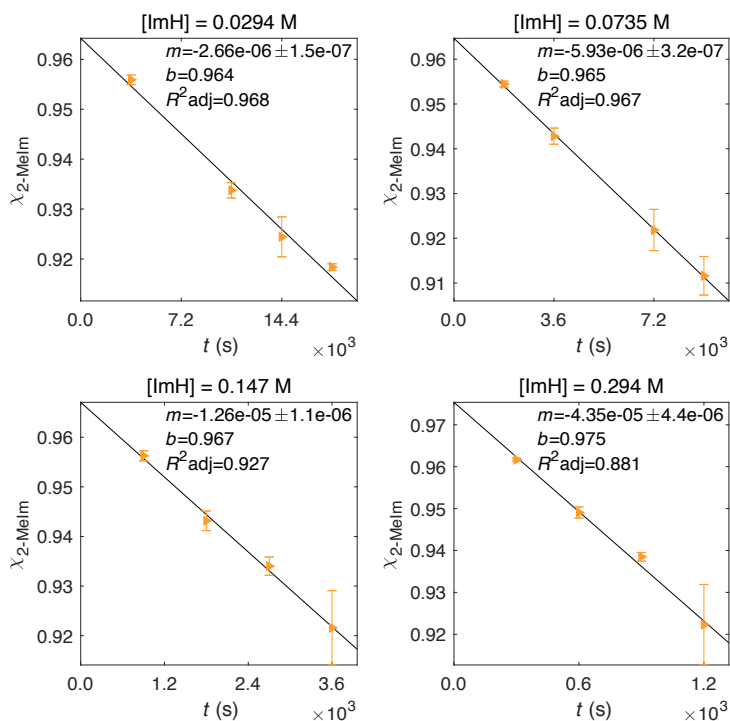


Figure AI-5. Conversion versus time plots used for determining the rate constants of ligand exchange in methanol at 70 °C. The black lines are the linear least squares regressions, with slopes equal to $-k_{\text{obs}}$. For reference, $3.6 \times 10^3 \text{ s} = 1 \text{ h}$.

0.0294 M			0.0735 M			0.147 M			0.294 M		
t (s)	$\chi_{2\text{-MeIm}}$	s	t (s)	$\chi_{2\text{-MeIm}}$	s	t (s)	$\chi_{2\text{-MeIm}}$	s	t (s)	$\chi_{2\text{-MeIm}}$	s
3600	0.9559	0.0010	1800	0.9545	0.0007	900	0.9563	0.0010	300	0.9617	0.0003
10800	0.9338	0.0015	3600	0.9428	0.0018	1800	0.9432	0.0020	600	0.9491	0.0013
14400	0.9244	0.0040	7200	0.9219	0.0046	2700	0.9340	0.0018	900	0.9385	0.0010
18000	0.9184	0.0006	9000	0.9116	0.0043	3600	0.9216	0.0075	1200	0.9223	0.0096

Table AI-5. Values of mole fraction of 2-methylimidazole, χ_{MeIm} , and uncertainty, expressed as the experimental standard deviation, s , of three reactions, for reactions in methanol at 70 °C.

Kinetics measurements in water

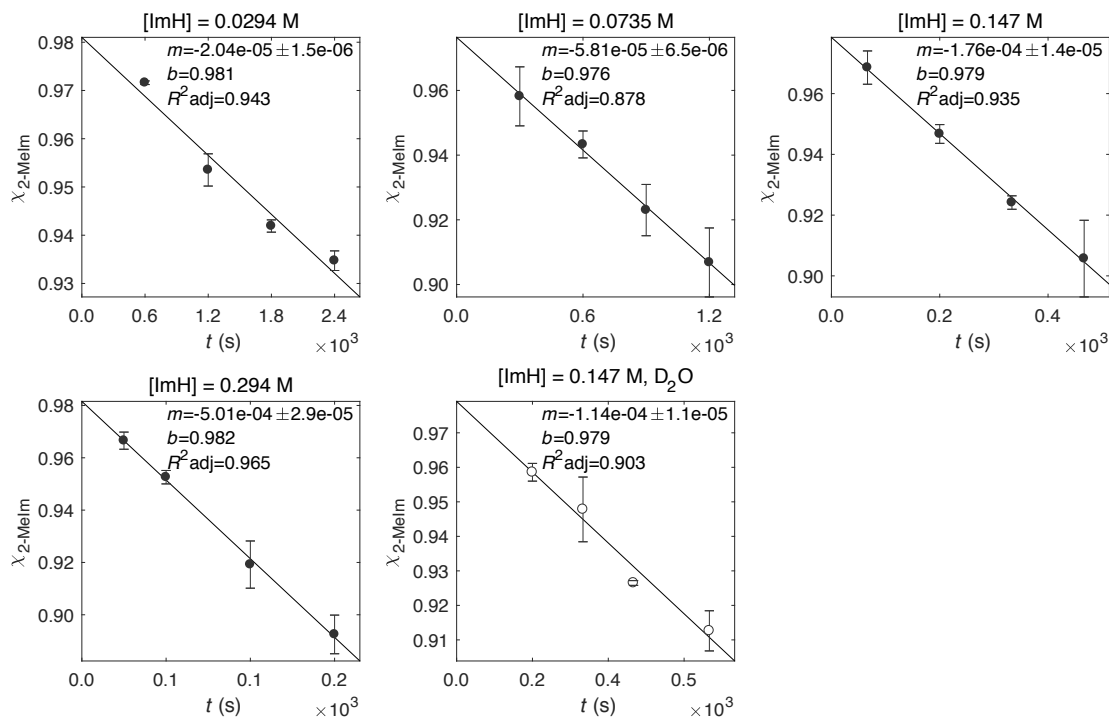


Figure AI-6. Conversion versus time plots used for determining the rate constants of ligand exchange in water and deuterium oxide at $4\text{ }^\circ\text{C}$. The black lines are the linear least squares regressions, with slopes equal to $-k_{\text{obs}}$. For reference, $2.4 \times 10^3\text{ s} = 40\text{ min}$ and $0.18 \times 10^3\text{ s} = 3\text{ min}$.

0.0294 M			0.0735 M			0.147 M			0.294 M			0.147 M, D_2O		
t (s)	$\chi_{2\text{-Melm}}$	s	t (s)	$\chi_{2\text{-Melm}}$	s	t (s)	$\chi_{2\text{-Melm}}$	s	t (s)	$\chi_{2\text{-Melm}}$	s	t (s)	$\chi_{2\text{-Melm}}$	s
600	0.9716	0.0004	300	0.9582	0.0091	60	0.9686	0.0055	30	0.9666	0.0033	180	0.9586	0.0026
1200	0.9535	0.0033	600	0.9433	0.0042	180	0.9467	0.0031	60	0.9526	0.0026	300	0.9478	0.0094
1800	0.9419	0.0013	900	0.9230	0.0079	300	0.9241	0.0022	120	0.9192	0.0090	420	0.9265	0.0007
2400	0.9347	0.0020	1200	0.9068	0.0107	420	0.9057	0.0126	180	0.8925	0.0074	600	0.9126	0.0058

Table AI-6. Values of mole fraction of 2-methylimidazole, χ_{Melm} , and uncertainty, expressed as the experimental standard deviation, s , of three reactions, for reactions in water at $4\text{ }^\circ\text{C}$.

Kinetics measurements on size-controlled ZIF-8

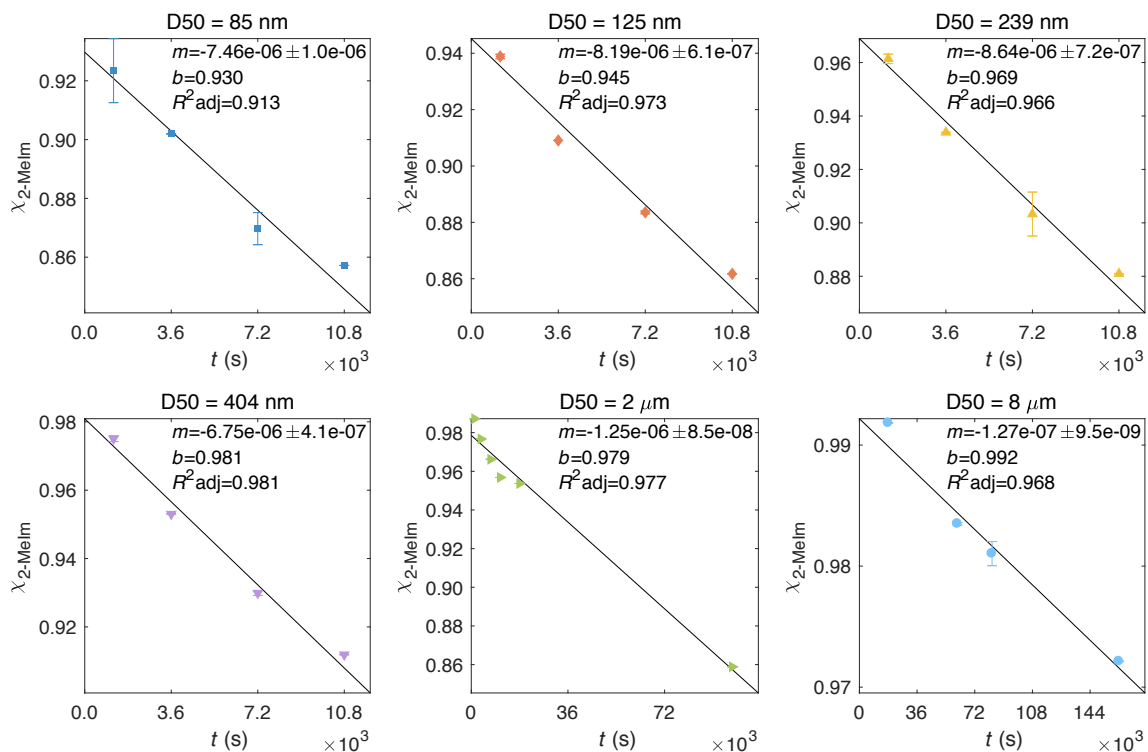


Figure AI-7. Conversion (as χ_{MeIm}) versus time plots used for determining the rate constants of ligand exchange for size-controlled ZIF-8 samples in *n*-butanol (BuOH) with 0.0735 M imidazole at 70 °C. The black lines are the linear least squares regressions, with slopes equal to $-k_{\text{obs}}$. For reference, $72 \times 10^3 \text{ s} = 20 \text{ h}$ and $3.6 \times 10^3 \text{ s} = 1 \text{ h}$.

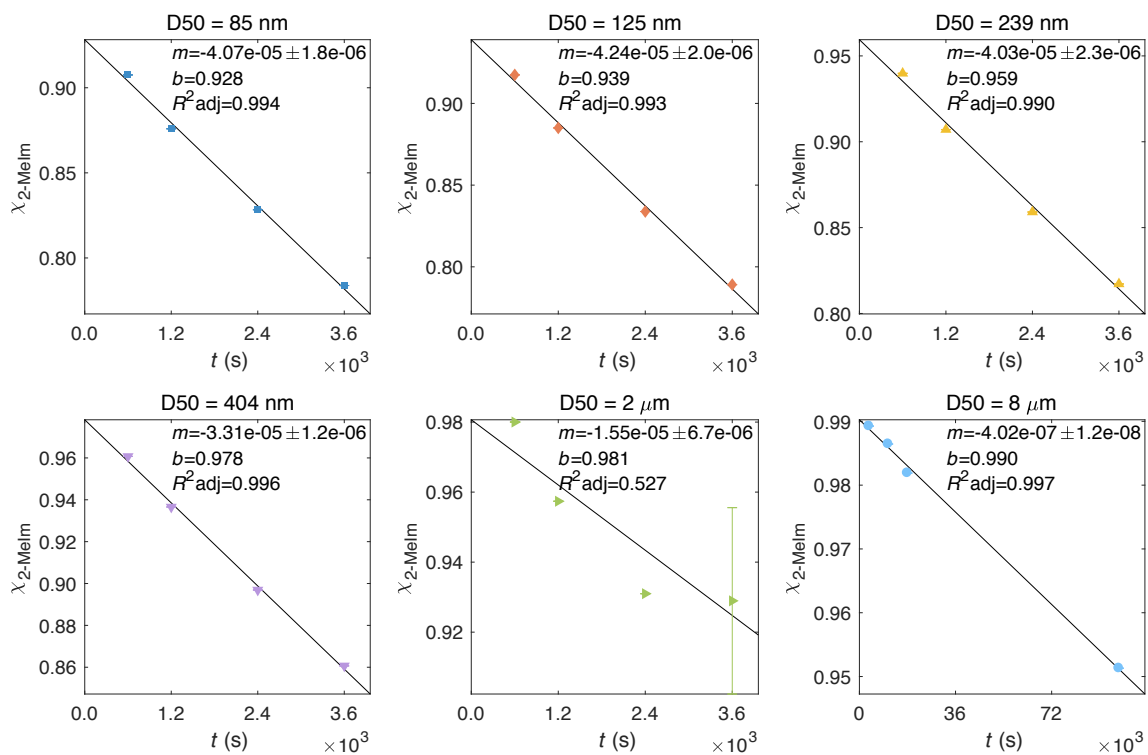


Figure AI-8. Conversion (as χ_{MeIm}) versus time plots used for determining the rate constants of ligand exchange for size-controlled ZIF-8 samples in *n*-butanol (BuOH) with 0.294 M imidazole at 70 °C. The black lines are the linear least squares regressions, with slopes equal to $-k_{\text{obs}}$.

Kinetics measurements in *n*-butanol used for Eyring analysis

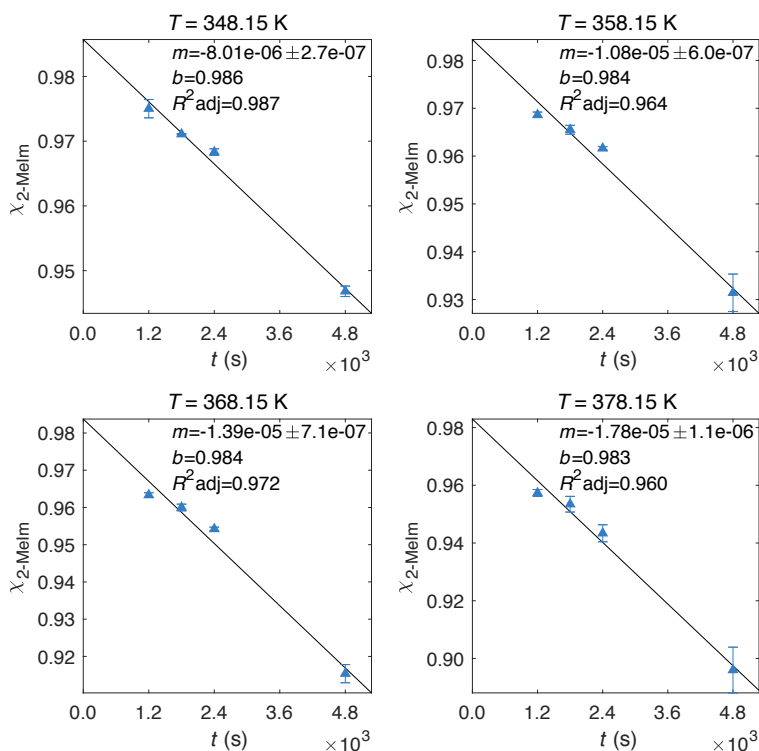


Figure AI-9. Conversion versus time plots used for determining the rate constants of ligand exchange in *n*-butanol with 0.0735 M imidazole at 75, 85, 95, and 105 °C. These rate constants were then used to generate the Eyring plot used to extrapolate the rate in *n*-butanol to 4 °C for direct comparison with water. The black lines are the linear least squares regressions, with slopes equal to $-k_{\text{obs}}$. For reference, 3.6×10^3 s = 1 h.

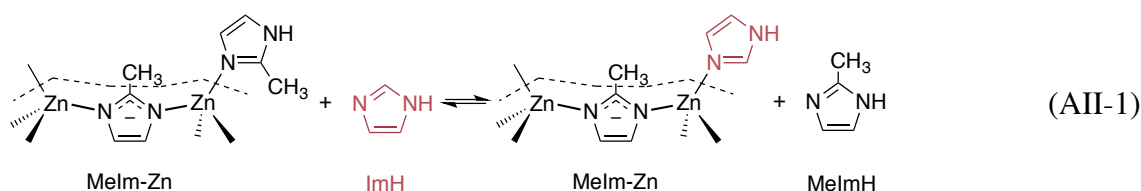
348.15 K			358.15 K			368.15 K			378.15 K		
t (s)	$\chi_{2\text{-Melm}}$	s									
1200	0.9750	0.0014	1200	0.9686	0.0006	1200	0.9633	0.0006	1200	0.9573	0.0012
1800	0.9711	0.0001	1800	0.9655	0.0009	1800	0.9600	0.0009	1800	0.9534	0.0027
2400	0.9683	0.0005	2400	0.9616	0.0004	2400	0.9542	0.0005	2400	0.9434	0.0029
4800	0.9468	0.0008	4800	0.9314	0.0039	4800	0.9154	0.0024	4800	0.8960	0.0079

Figure AI-7. Values of mole fraction of 2-methylimidazole, χ_{Melm} , and uncertainty, expressed as the experimental standard deviation, s , of three reactions, for reactions in *n*-butanol with [imidazole] = 0.0735 M.

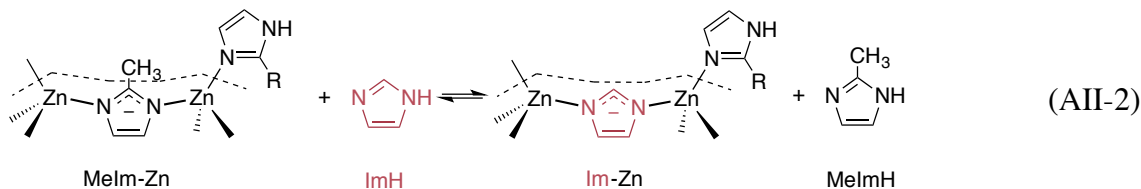
5.0 APPENDIX II

Calculations of surface ligand density

Linker exchange is expected to be more rapid at the surface of a ZIF-8 crystal than in the bulk because surface imidazole species are only mono-coordinated and neutral, and thus more weakly bonded. Two types of imidazole species are present at the crystal surface: (1) neutral dangling MeImH ligands and (2) anionic framework MeIm⁻ linkers that are identical in every way to bulk MeIm⁻ except that they are located on the crystal surface and thus bonded to two Zn(MeIm)₂(MeImH) units, instead of two Zn(MeIm)₃ units as they would be in the bulk. The substitution rate of dangling MeImH with ImH from solution (eq. (AII-1), dashed line represents crystal surface) is expected to greatly exceed bulk linker exchange (eq. (AII-2)), as the neutral mono-coordinated ligand is more labile.



The substitution rate of surface layer MeIm⁻ linkers (eq. (AII-2)) may vary somewhat from that of the bulk due to the extra substitutionally labile site on Zn.



These rapid substitution reactions are likely the origin of the shift of the y-intercept away from 1.0 in the χ_{MeIm} versus time plots. As such, these reactions cause a constant offset, do not affect the rate of change of χ_{MeIm} , and thus their presence does not conflict with our interpretation of k_{obs} (the slope of χ_{MeIm} vs. time plots) as the rate

constant of bulk linker exchange. To support the idea that these reactions are the origin of $b < 1$ in χ_{MeIm} vs. time, we can calculate the fraction of surface to bulk linkers. Starting with a typical surface of ZIF-8 (Figure AII-1), we can see that a {100} surface has 12 surface ligands: 4 dangling MeImH and 8 MeIm⁻.

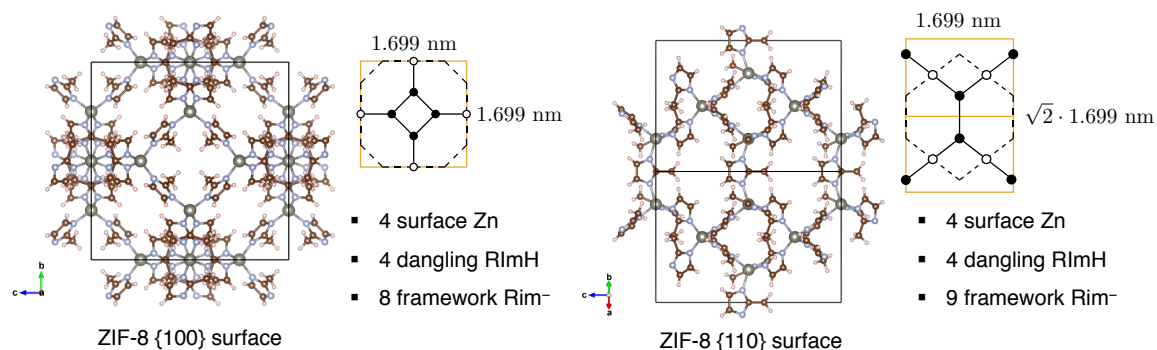


Figure AII-1. Two typical surfaces of ZIF-8 {100} and {110} used to calculate the surface density (molecules per nm²) of surface RIm(H) species. Surface projection images generated using VESTA.¹

The density of surface ligands RIm(H) on the crystal surface can then be calculated from the unit cell dimensions of ZIF-8 and the stoichiometry in Figure AII-1 for dangling MeImH only (eq. (AII-3)) and dangling MeImH plus framework MeIm⁻ (eq. (AII-4)).

$$\frac{4 \text{ surface Zn}}{(1.699 \text{ nm})^2} \cdot \frac{1 \text{ dangling RImH}}{\text{surface Zn}} = 1.3857 \text{ dangling RImH/nm}^2 \quad (\text{AII-3})$$

$$\frac{4 \text{ surface Zn}}{(1.699 \text{ nm})^2} \cdot \frac{1 \text{ dangling RImH} + 2 \text{ framework RIm}^-}{\text{surface Zn}} = 4.1571 \text{ surface RIm(H)/nm}^2 \quad (\text{AII-4})$$

¹ Momma, K. and Izumi, F. VESTA 3 for three-dimensional visualization of crystal, volumetric and morphology data *J. Appl. Crystallogr.* **2011**, *44*, 1272–1276.

Then using the surface area of a ZIF-8 particle (e.g. eq. (AII-5) for a 265 nm crystal assuming spherical geometry), we can obtain the number of surface ligands RIm(H) for dangling only (eq. (AII-6)) and dangling + framework (eq. (AII-7)).

$$\text{surface area} = 4 \cdot \pi \cdot \left(\frac{265 \text{ nm}}{2} \right)^2 = 2.2142 \times 10^5 \text{ nm}^2 \quad (\text{AII-5})$$

$$2.2142 \times 10^5 \text{ nm}^2 \cdot \frac{1.3857 \text{ dangling RImH}}{\text{nm}^2} = 3.0682 \times 10^5 \text{ surface dangling RImH} \quad (\text{AII-6})$$

$$2.2142 \times 10^5 \text{ nm}^2 \cdot \frac{4.1571 \text{ dangling RImH}}{\text{nm}^2} = 9.2047 \times 10^5 \text{ surface RIm(H)} \quad (\text{AII-7})$$

Then using the volume of a ZIF-8 particle (e.g. eq. (AII-8) for a 265 nm crystal assuming spherical geometry) and the density of ZIF-8 (expressed as T/V , for tetrahedral metal (T) per unit volume in nm^3), we can obtain the number of linkers in the crystal (eq. (AII-9)).

$$\text{volume} = \frac{4}{3} \cdot \pi \cdot \left(\frac{265 \text{ nm}}{2} \right)^3 = 9.7972 \times 10^6 \text{ nm}^3 \quad (\text{AII-8})$$

$$9.7972 \times 10^6 \text{ nm}^3 \cdot \frac{2.45 \text{ Zn}}{\text{nm}^3} \cdot \frac{2 \text{ RIm}^-}{\text{Zn}} = 4.8006280 \times 10^7 \text{ RIm}^- \quad (\text{AII-9})$$

From the ligand quantities in eq. AII-6, AII-7, and AII-9, we can calculate the fraction surface to bulk ligands for dangling only (eq. (AII-10)) and dangling + framework (eq. (AII-11)).

$$\text{fraction of dangling ligands at surface} = \frac{3.0682 \times 10^5 \text{ RImH}}{4.8006280 \times 10^7 \text{ RIm}^-} = 0.0064 \quad (\text{S7.10})$$

$$\text{fraction of ligands (dangling + first layer) at surface} = \frac{9.2047 \times 10^5 \text{ RIm(H)}}{4.8006280 \times 10^7 \text{ RIm}^-} = 0.0192 \quad (\text{S7.11})$$

From this analysis, we can see that, for a 265 nm diameter spherical ZIF-8 crystal with {100} surfaces, surface ligands comprise 0.64 % or 1.92 % of the total ligands in the crystal, depending on if you count only dangling MeImH or dangling + first-layer framework MeIm⁻, respectively. By the above equations, the fractions of surface to bulk ligands for all the ZIF-8 crystal sizes used in this study can be calculated and compared with their experimental y-intercepts in χ_{MeIm} vs. time plots (Table AII-1). The linear correlation between the experimental y-intercepts and the calculated % surface RIm(H) values based on the experimental particle size distributions (Figure AII-1) is consistent with our hypothesis that the shift of the y-intercept comes from rapid surface ligand exchange reactions (eq. (AII-1) to (AII-2)). The experimental y-intercepts in all cases exceed the highest calculated % surface RIm(H), which could come from the fact that a real crystal, in addition to {100} and {110} surfaces, contains edge and corner sites with a higher density of surface RIm(H).

D_{50} (nm)	y-int in mole % Im		calc. % surface RIm(H)			
	0.0735 M	0.294 M	{100} lower	{100} upper	{110} lower	{110} upper
85	7.0	7.2	2.0	6.0	1.4	4.6
126	5.5	6.1	1.4	4.1	1.0	3.1
239	3.1	4.1	0.71	2.1	0.50	1.6
266	2.7	3.4	0.64	1.9	0.45	1.5
404	1.9	2.2	0.42	1.3	0.30	1.0
1963	2.1	1.9	0.086	0.26	0.06	0.20
7755	0.8	1.0	0.022	0.066	0.016	0.050

Table AII-1. The correlation between ZIF-8 crystal size and the y-intercept in conversion vs. time plots. The lower (dangling RImH only) and upper (dangling RImH + framework RIm⁻) bounds are given for the calculated % surface RIm(H) of each surface.

6.0 APPENDIX III

Powder X-ray diffraction patterns

PXRD patterns of samples used in the initial rates kinetic analysis

There were no observable crystalline phases besides sodalite (**sod**) in the samples used to measure k_{obs} (Figures AI-1 to AI-6). Samples in this kinetics group were chosen for PXRD analysis randomly from one of the three reactions (15 mg/ea.) at the longest time point used for that solvent/concentration. MOF powders collected after reaction and washing were used for PXRD measurements and then recollected for digestion $^1\text{H-NMR}$.

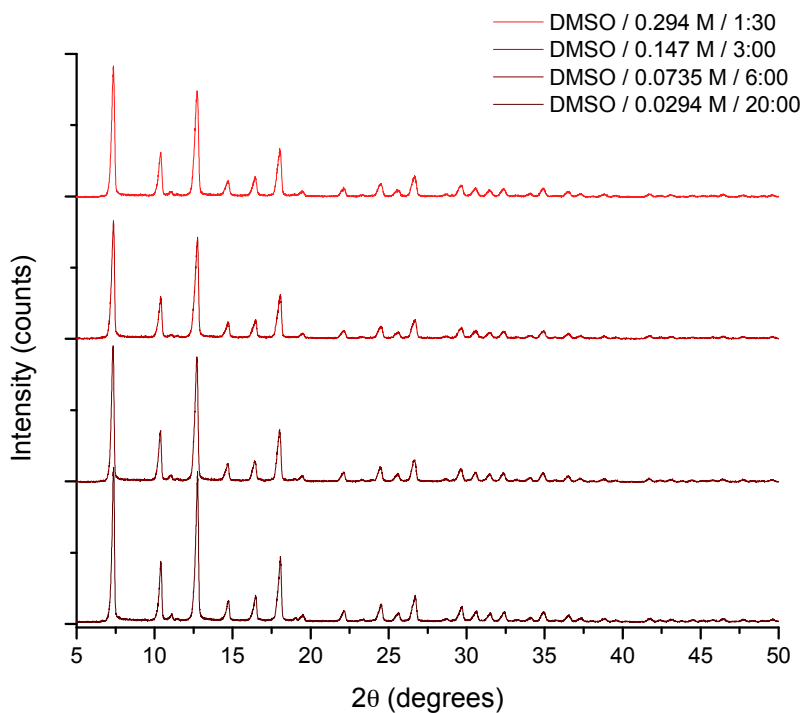


Figure AIII-1. PXRD patterns of the products with the highest values of conversion that were used for determining rate constants in dimethyl sulfoxide solutions. Time is given in h:min.

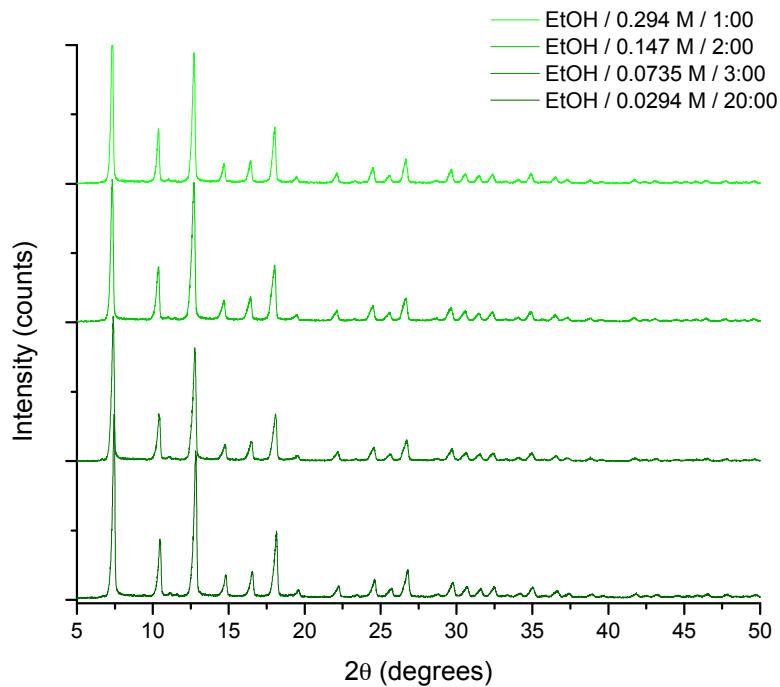


Figure AIII-2. PXRD patterns of the products with the highest values of conversion that were used for determining rate constants in ethanol solutions.

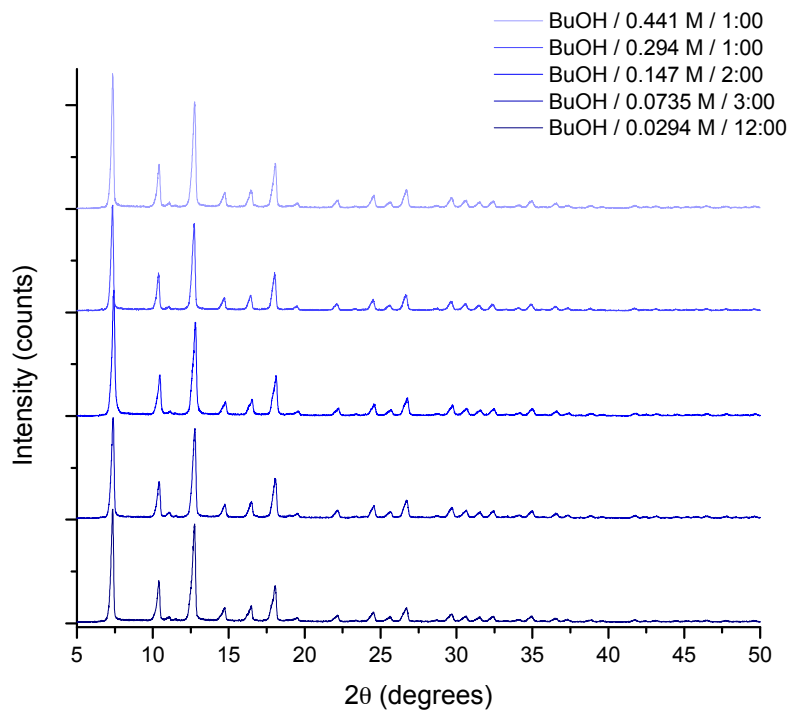


Figure AIII-3. PXRD patterns of the products with the highest values of conversion that were used for determining rate constants in *n*-butanol solutions.

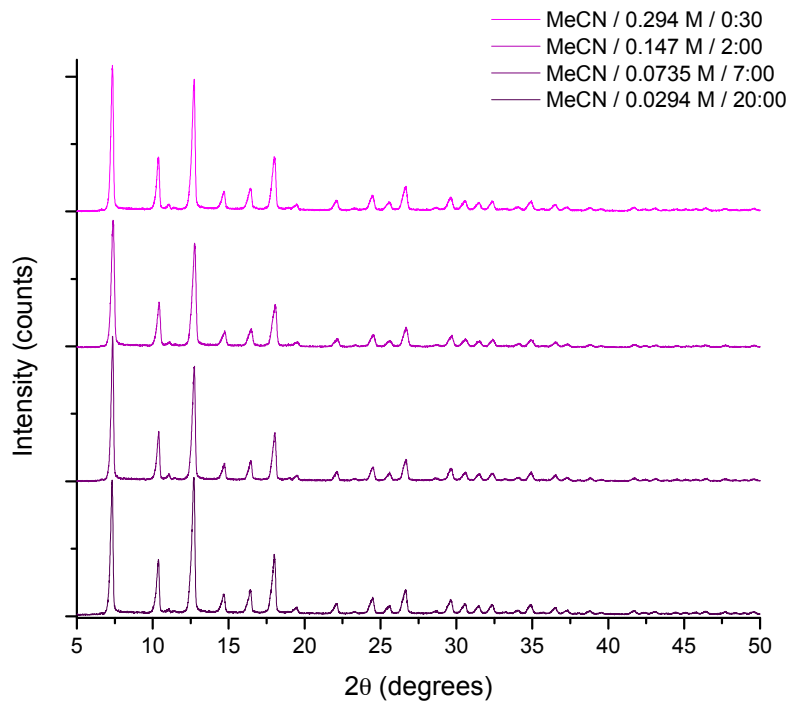


Figure AIII-4. PXRD patterns of the products with the highest values of conversion that were used for determining rate constants in acetonitrile solutions.

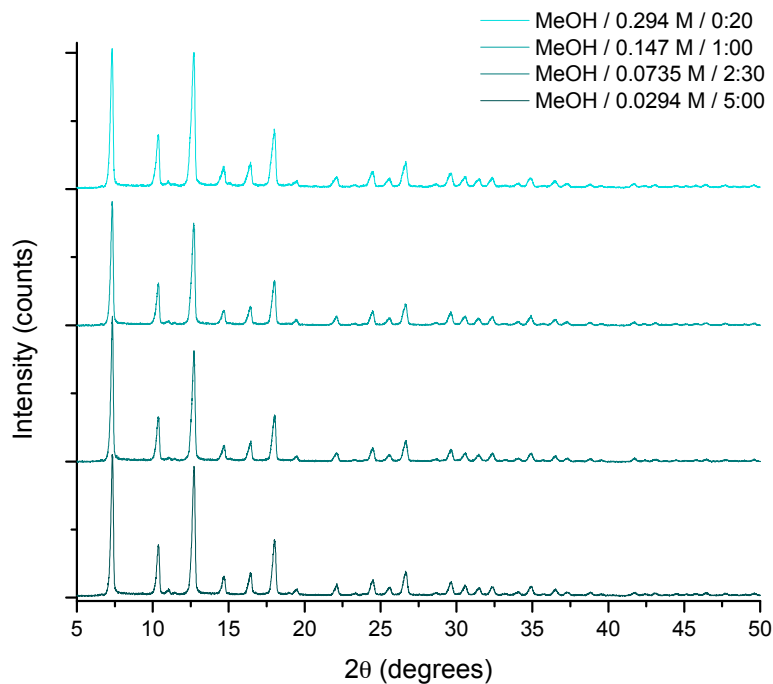


Figure AIII-5. PXRD patterns of the products with the highest values of conversion that were used for determining rate constants in methanol solutions.

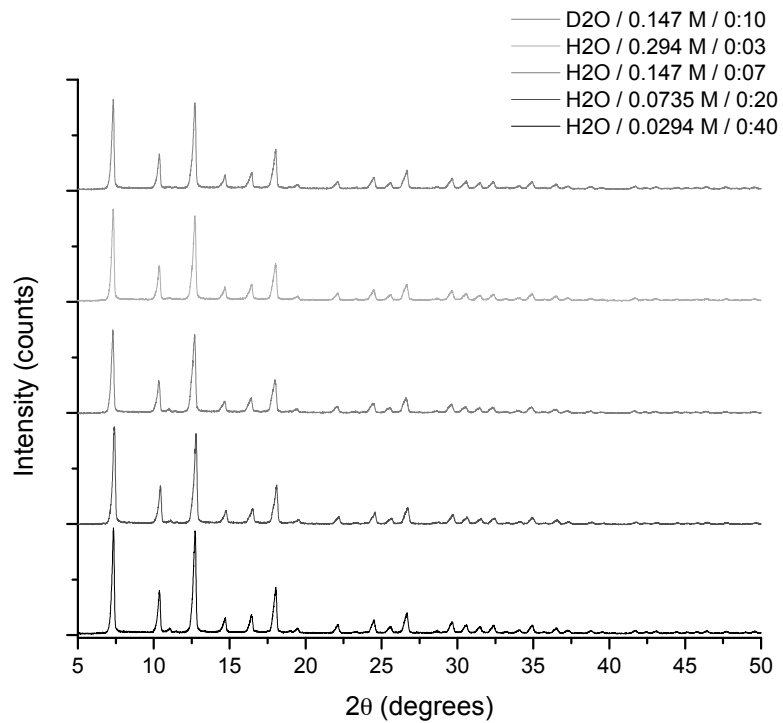


Figure AIII-6. PXRD patterns of the products with the highest values of conversion that were used for determining rate constants in aqueous solutions at 4 °C.

PXRD patterns for extended (10 d) reaction times

We noticed that extending the reaction times beyond those used for initial rate kinetics resulted in new PXRD peaks for some samples (Table 3-3). The appearance of this new phase was correlated with the solvent and imidazole concentration (summarized: Table 3-3 and Figure 3-13, PXRD: Figures AIII-10 to AIII-15). Two samples representative of a mixed phase and a pure phase after long (3 d) reactions are shown in Figure AIII-7. By comparison with the simulated patterns for ZIF-61,¹ IMIDZB01,² and ZIF-8,³ we can see that the mixed phase material is a mixture of **sod** and **zni** with no other detectable phases. ZIF-61 (Zn(2-MeIm)(Im)) and IMIDZB01 (Zn(Im)₂) both have the **zni** (from ZnI₂) topology, which for ZIFs results in a dense nonporous material (Figure AIII-7).

The lack of porosity limits the applications of ZIFs with the **zni** topology. Moreover, the **sod** → **zni** phase change is a separate chemical process with a different rate than the ligand substitution reaction of interest, and therefore samples that display a phase change are unusable for determining the kinetics of exchange. There is evidence that the phase change to **zni** accelerates the exchange reaction by changing the reaction from endergonic ($x \text{ ImH} + \text{sod-Zn(2-MeIm)}_2 \rightarrow x \text{ 2-MeImH} + \text{sod-Zn(2-MeIm)}_{2-x}(\text{Im})_x$) to exergonic ($x \text{ ImH} + \text{sod-Zn(2-MeIm)}_2 \rightarrow x \text{ 2-MeImH} + \text{zni-Zn(2-MeIm)}_{2-x}(\text{Im})_x$) (Figure AIII-9).

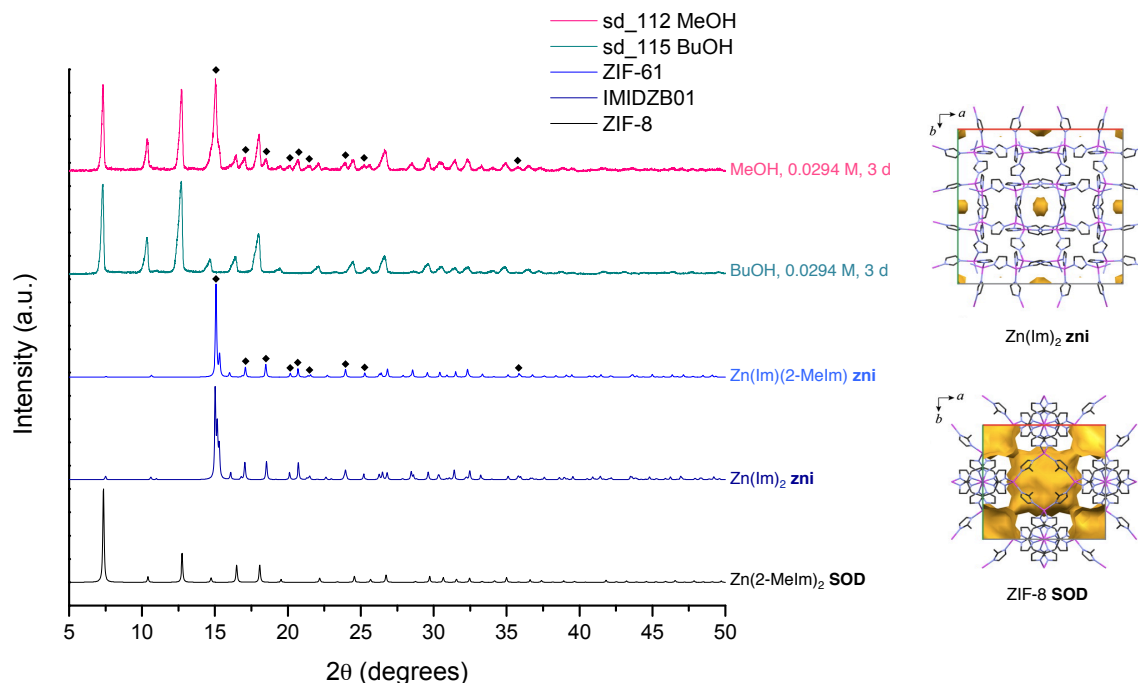


Figure AIII-7. PXRD patterns for a mixed **sod/zni** phase sample (MeOH, 0.0294 M, 3 d, conv. = 54.5 %) (w = peaks indexed to **zni**) and a sample run for an equivalent time and concentration for which there was no phase change (BuOH, 0.0294 M, 3 d, conv. = 13.9 %), along with simulated patterns for ZIF-61 (**zni**), IMIDZB01 (**zni**), and ZIF-8 (**sod**). Cartoons adapted from a publication⁴ showing the solvent-accessible volumes for **zni**-Zn(Im)₂ (IMIDZB01) and **sod**-Zn(2-MeIm)₂ (ZIF-8) illustrate the nonporous nature of ZIFs with the **zni** topology.

The phase change to **zni** is unsurprising as it is the thermodynamic sink of ZIF topologies.⁵⁻⁸ The frequency of occurrence of the **zni** phase change follows the order: water > MeOH > EtOH > MeCN > BuOH > DMSO. This order correlates somewhat with the order of k_{obs} but even better with the order of molecular size/kinetic diameter (for definitions see section VI/Solvent size and mass transport terms, p. S37), with the phase change occurring most frequently for smaller molecules. The kinetic diameters of the solvents follow the order: water < MeOH < MeCN < EtOH < DMSO⁹ < BuOH (Table

AV-5). This correlation with solvent molecular size suggests that solvent packing may play a role in preserving the low-density **sod** topology, similar to the role proposed for the solvent as a structure-directing agent during the synthesis of some MOFs.¹⁰ We observed a phase change in BuOH after 10 days at 0.147 M ImH in contrast to the observations of Karagiari et al.,¹¹ which may be related to the smaller ZIF-8 crystal size in our case (~270 nm vs. ~1 mm). The **zni** phase was however observed by the same authors after boiling **sod**-Zn(MeIm)_{0.3}(Im)_{1.7} (SALEM-2) in water for 24 h.¹² DMSO is the only solvent found to display no phase change under any of the reaction times tested. The highest conversion reached with a pure **sod** phase from the 10-day reactions was 59.8 % (DMSO, 0.294 M), or composition Zn(2-MeIm)_{0.8}(Im)_{1.2}.

While the tendency of the Zn/imidazole system to undergo phase changes to **zni** has clear practical drawbacks, its benefit to kinetics studies is worth noting. The question is often asked in MOF linker exchange studies whether exogenous linker incorporation is due to exchange or to dissolution-recrystallization (see Chapter 3 refs [16b], [16c], [16i], and [17j]), which is often phrased as whether the process occurs in a single-crystal-to-single-crystal (SCSC) fashion. For the exchange reaction under investigation (eq. (3-2)) the absence of the **zni** phase in a product is evidence that dissolution-recrystallization did not occur, at least not up to the detection limit of PXRD (ca. 1 %, whereas exchange is up to 10 %). Whether the cases in which we do observe the **zni** phase come from dissolution-recrystallization or a SCSC phase change of **sod**-Zn(2-MeIm)_{2-x}(Im)_x → **zni**-Zn(2-MeIm)_{2-x}(Im)_x is unclear and it is reasonable to expect that one process or the other could dominate depending on the conditions.

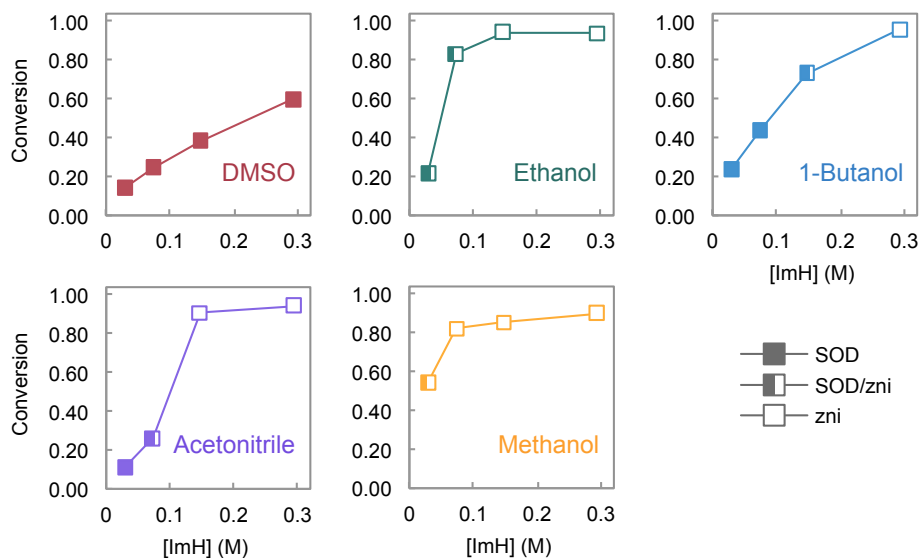


Figure AIII-8. Plots of the data from Table 3-3: conversion ($= \chi_{\text{Im}} = 1 - \chi_{2\text{-MeIm}}$) versus initial [ImH]. Shading of the data points indicates qualitatively the relative amount of each phase observed in PXRD.

Equilibrium constant calculations: (values appear in Chapter 3, Figure 3-13)

For the reaction $\text{ZnA}_2 + x \text{B} \rightarrow \text{ZnA}_{2-x}\text{B}_x + x \text{A}$, with $\text{A} = 2\text{-MeIm}^-$, $\text{B} = \text{Im}^-$, and $c_{\text{B}} =$ initial concentration of ImH:

$$\text{Total amount of A or B: } n_{\text{A total}} = \text{wt. ZIF-8} \times \left(\frac{\text{mol ZIF-8}}{227.57 \text{ g}} \right) \times \left(\frac{2 \text{ mol A}}{\text{mol ZIF-8}} \right) \quad n_{\text{B total}} = c_{\text{B}} \times 0.003 \text{ L}$$

Amount of A or B in solution:

$$n_{\text{A soln.}} = \chi_{\text{B}} \times n_{\text{A total}}$$

$$n_{\text{B soln.}} = n_{\text{B total}} - n_{\text{A soln.}}$$

Mole fraction of A or B in solution:

$$\chi_{\text{A soln.}} = \frac{n_{\text{A soln.}}}{n_{\text{B total}}}$$

$$\chi_{\text{B soln.}} = 1 - \chi_{\text{A soln.}}$$

Equilibrium constant:

$$K_{\text{eq}} = \frac{\chi_{\text{A soln.}} \chi_{\text{B solid}}}{\chi_{\text{B soln.}} \chi_{\text{A solid}}}$$

Standard Gibbs free energy change:

$$\Delta G^\circ = -RT \ln K_{\text{eq}}$$

Using the above relations, in a manner analogous to Brozek,¹³ and assuming that the reactions have come to equilibrium, we can estimate K_{eq} (Figure 3-13) and ΔG° (Figure AIII-9) for the 10-day reactions. From this analysis we see that values of $K_{eq} > 1$ and $\Delta G^\circ < 0$ are only observed for reactions with **zni** as the majority phase.

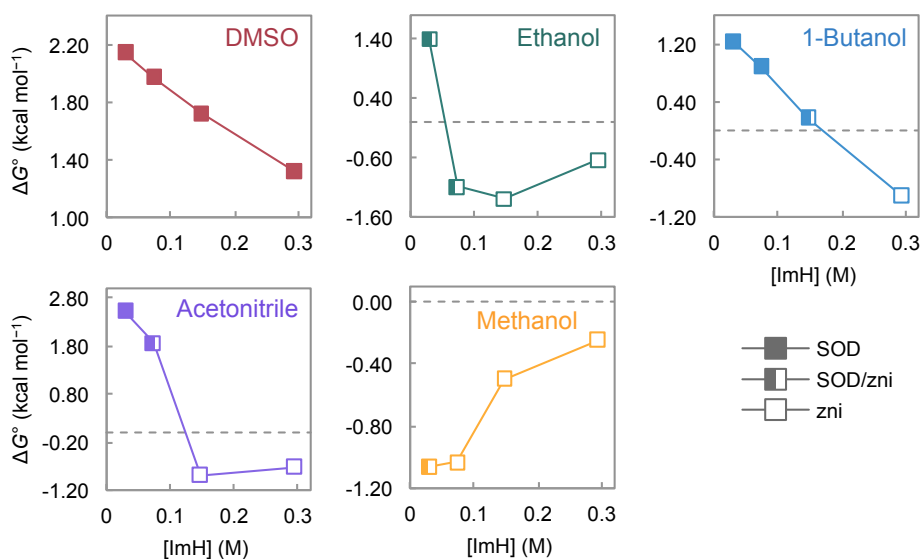


Figure AIII-9. Change in free energy, ΔG° , versus initial [ImH] for 10-day reactions at 70 °C. Shading of the data points indicates qualitatively the relative amount of each phase observed in PXRD (patterns in Figures AIII-10 to -14). $\Delta G^\circ = 0$ (thermoneutral) is indicated with dashed lines.

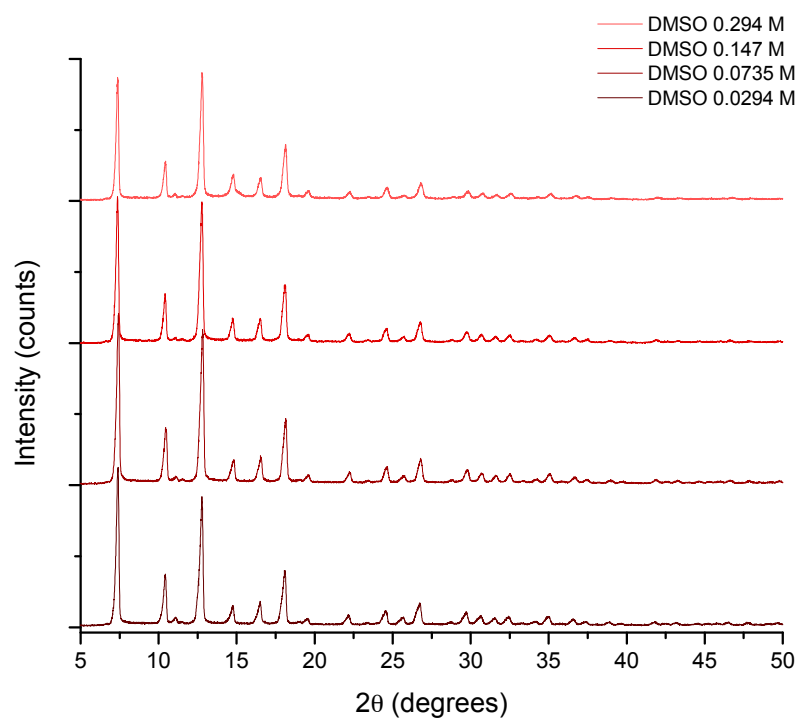


Figure AIII-10. PXRD patterns of the products from 10-day reactions in dimethyl sulfoxide.

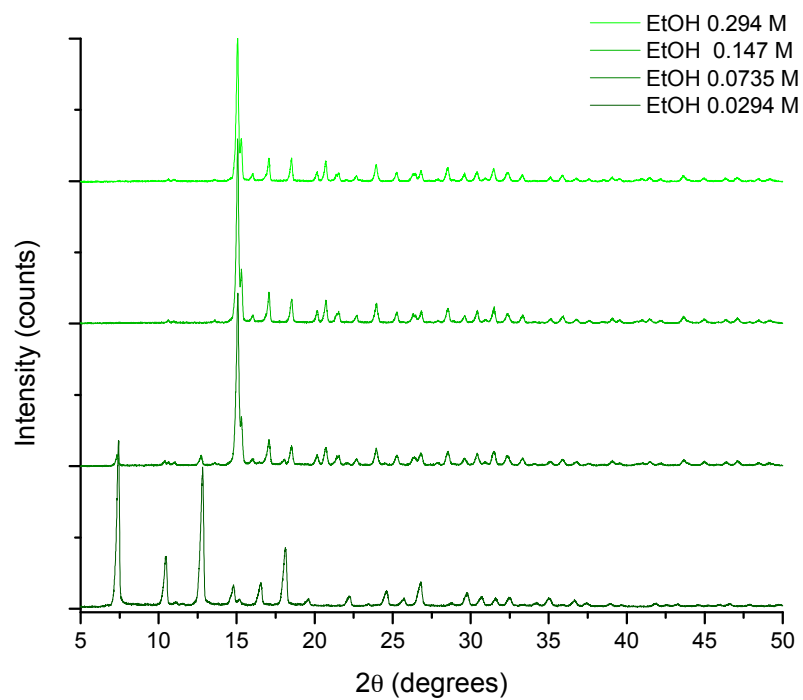


Figure AIII-11. PXRD patterns of the products from 10-day reactions in ethanol.

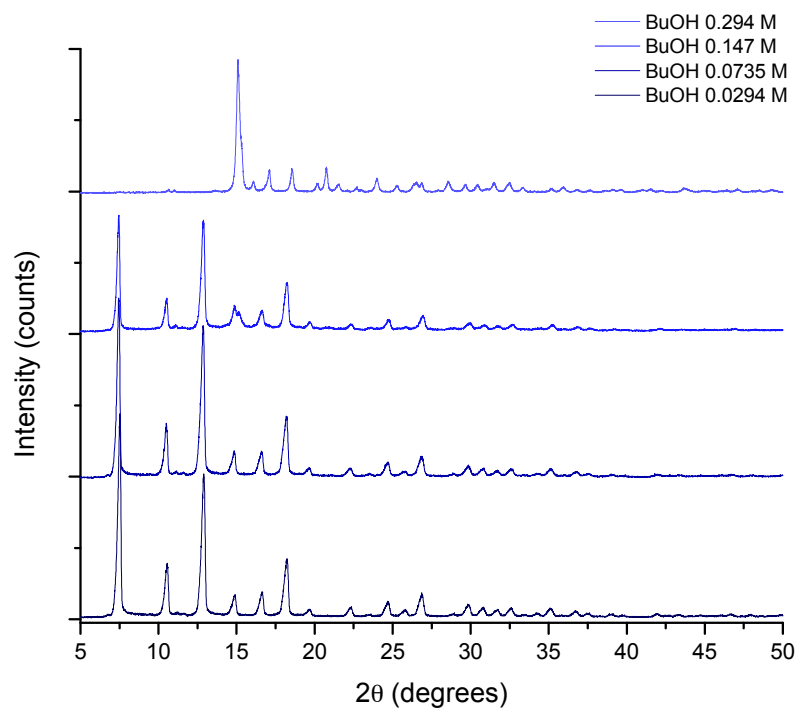


Figure AIII-12. PXRD patterns of the products from 10-day reactions in *n*-butanol.

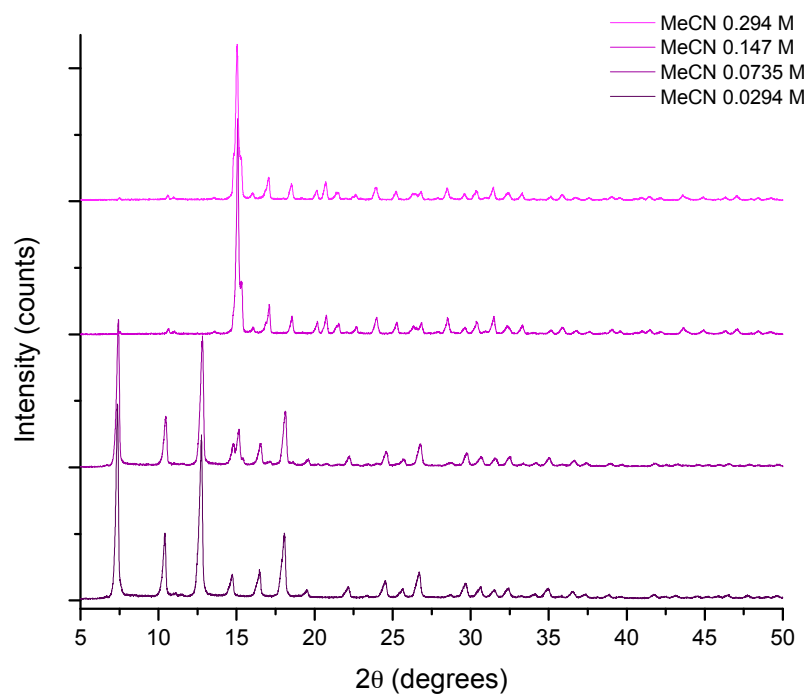


Figure AIII-13. PXRD patterns of the products from 10-day reactions in acetonitrile.

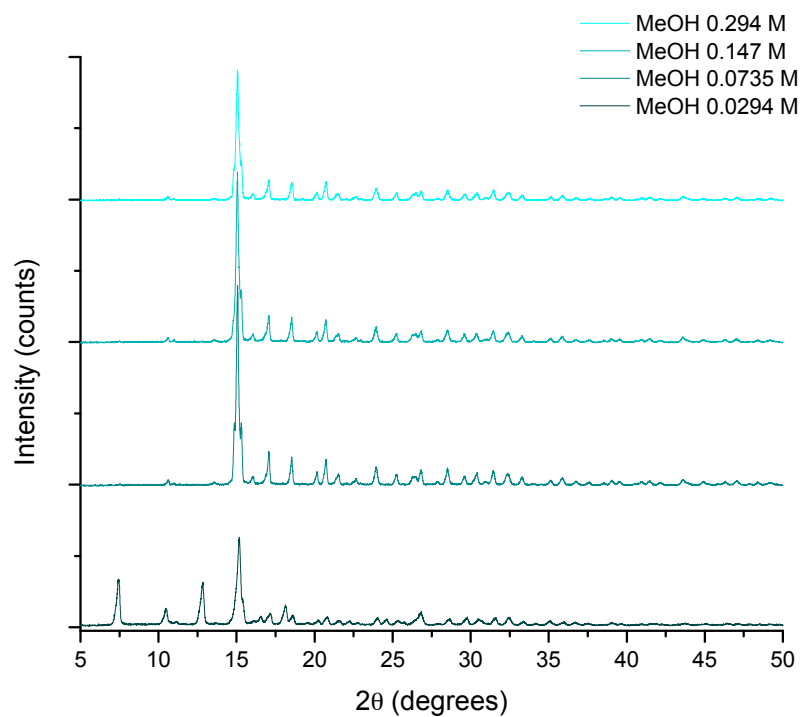


Figure AIII-14. PXRD patterns of the products from 10-day reactions in methanol.

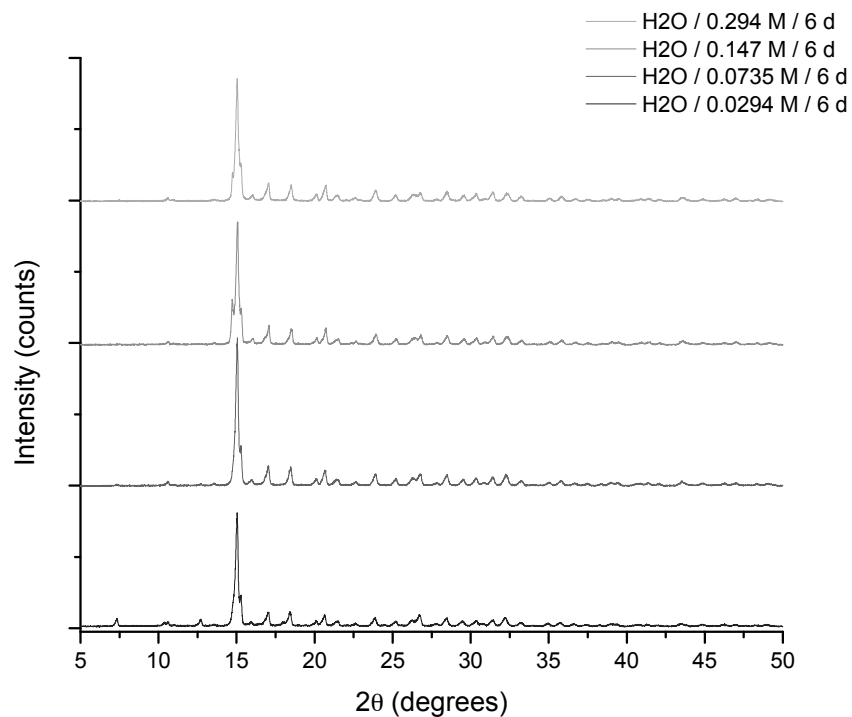


Figure AIII-15. PXRD patterns of the products from 6-day reactions in water at 4°C .

Appendix III References

- (1) Banerjee, R.; Phan, A.; Wang, B.; Knobler, C.; Furukawa, H.; O’Keeffe, M.; Yaghi, O. M. High-Throughput Synthesis of Zeolitic Imidazolate Frameworks and Application to CO₂ Capture. *Science* **2008**, *319*, 939– 943. (CCDC code GITTAF)
- (2) Lehnert, R.; Seel, F. *Z. Anorg. Allg. Chem.* **1980**, *464*, 187–194. (CCDC code IMIDZB01)
- (3) Park, K. S.; Ni, Z.; Côté, A. P.; Choi, J. Y.; Huang, R.; Uribe-Romo, F. J.; Chae, H. K.; O’Keeffe, M.; Yaghi, O. M. Exceptional chemical and thermal stability of zeolitic imidazolate frameworks. *Proc. Natl. Acad. Sci. U.S.A.* **2006**, *103*, 10186– 10191. (CCDC code VELVOY01)
- (4) Tan, J. C.; Bennett, T. D., Cheetham, A. K. Chemical structure, network topology, and porosity effects on the mechanical properties of Zeolitic Imidazolate Frameworks. *Proc. Natl. Acad. Sci. U.S.A.* **2010**, *107* (22), 9938-9943.
- (5) Gee, J. S. and Sholl, D.S. Characterization of the Thermodynamic Stability of Solvated Metal–Organic Framework Polymorphs Using Molecular Simulations. *J. Phys. Chem. C* **2013**, *117*, 20636–20642.
- (6) Baburin, I. A. and Leoni, S. The energy landscapes of zeolitic imidazolate frameworks (ZIFs): towards quantifying the presence of substituents on the imidazole ring. *J. Mater. Chem.* **2012**, *22*, 10152–10154.
- (7) Lewis, D. W.; Ruiz-Salvador, A. R.; Gómez, A.; Rodriguez-Albelo, L. M.; Coudert, F.-X.; Slater, B.; Cheetham, A. K., Mellot-Draznieks, C. Zeolitic imidazole frameworks: structural and energetics trends compared with their zeolite analogues. *CrystEngComm* **2009**, *11*, 2272–2276.

- (8) Hughes, J. T.; Bennett, T. D.; Cheetham, A. K.; Navrotsky, A. Thermochemistry of Zeolitic Imidazolate Frameworks of Varying Porosity. *J. Am. Chem. Soc.* **2013**, *135*, 598–601.
- (9) A few molecular sizing methods reverse the generally accepted order of BuOH as larger than DMSO, e.g. a 5.8 Å diameter for DMSO in: Schrader, A. M.; Donaldson, S. H. Jr; Song, J.; Cheng, C.Y.; Lee, D. W.; Han, S., Israelachvili, J. N. Correlating steric hydration forces with water dynamics through surface force and diffusion NMR measurements in a lipid–DMSO–H₂O system. *Proc. Natl. Acad. Sci. USA* **2015**, *112*, 10708–10713.
- (10) Tian Y.-Q.; Zhao, Y.-M.; Chen, Z.-X.; Zhang, G.-N.; Weng, L.-H.; Zhao, D.-Y. Design and Generation of Extended Zeolitic Metal–Organic Frameworks (ZMOFs): Synthesis and Crystal Structures of Zinc(II) Imidazolate Polymers with Zeolitic Topologies. *Chem. Eur. J.* **2007**, *13*, 4146–4154.
- (11) Karagiari, O.; Lalonde, M. B.; Bury, W.; Sarjeant, A. A.; Farha, O. K.; Hupp, J. T., Opening ZIF-8: A Catalytically Active Zeolitic Imidazolate Framework of Sodalite Topology with Unsubstituted Linkers. *J. Am. Chem. Soc.* **2012**, *134* (45), 18790-18796.
- (12) Supporting information from Ref. [11], file: ja308786r_si_004.pdf, p. S7, figure S6
- (13) Brozek, C. K. and Dincă, M. Thermodynamic parameters of cation exchange in MOF-5 and MFU-4l. *Chem. Commun.* **2015**, *51*, 11780–11782.

7.0 APPENDIX IV

Transmission electron micrographs

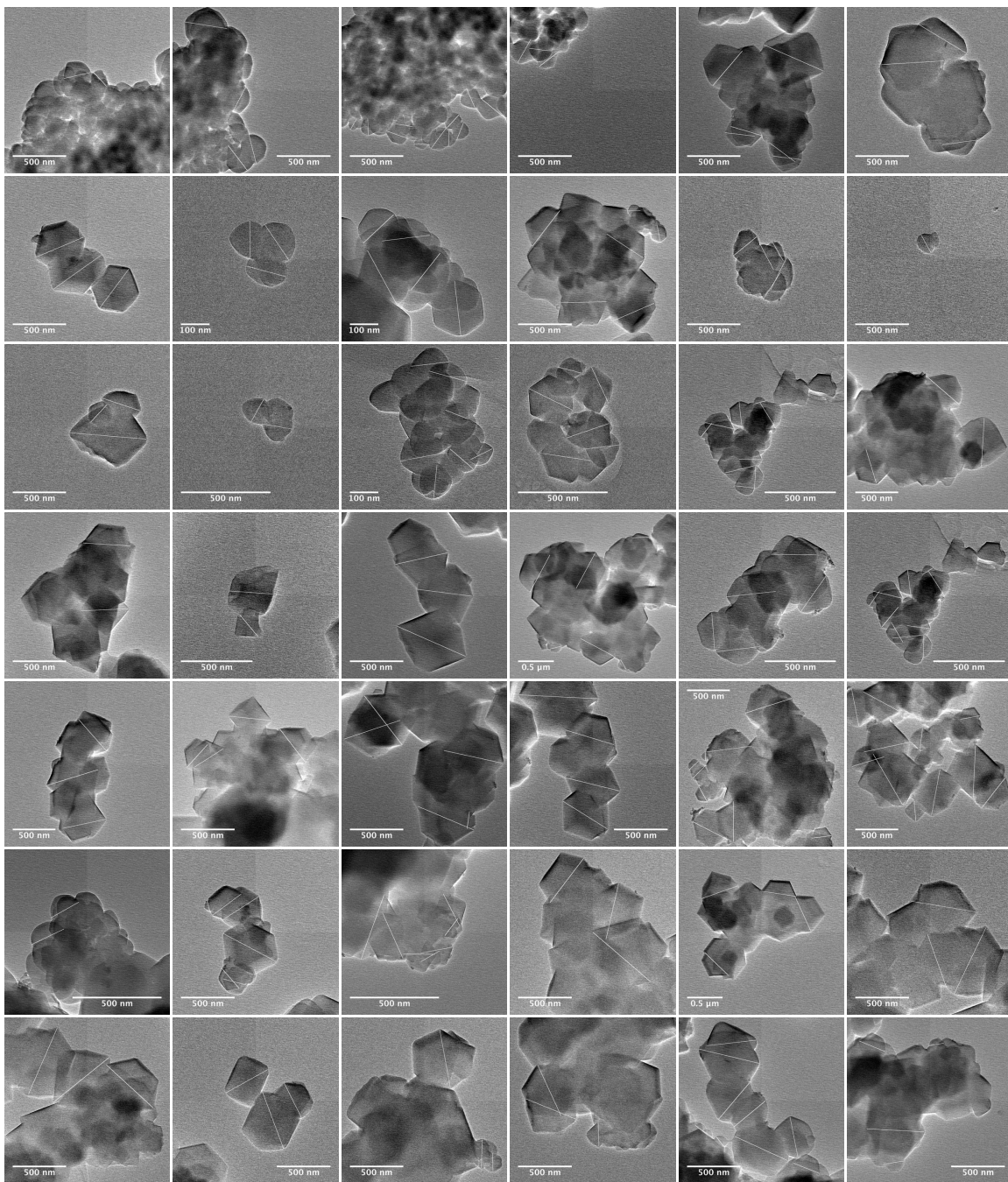


Figure AIV-1. TEM images used to calculate the grain size distribution of the commercial sample, Basolite Z1200, with a D50 of 265 nm. White lines are the grain diameter, d , measurements. The distinction between grain size and particle size is seen to matter for this sample, which is composed of crystals (grain size, d) that are intergrown into larger aggregates (particle size). Individual crystal grains are recognized by the contrast with surrounding crystals

and by the crystal habit of ZIF-8. High resolution imaging of the lattice of ZIF-8 to confirm that the measured crystals were actually composed of one grain only was not possible due to the instability of ZIF-8 under the 200 kV electron beam.

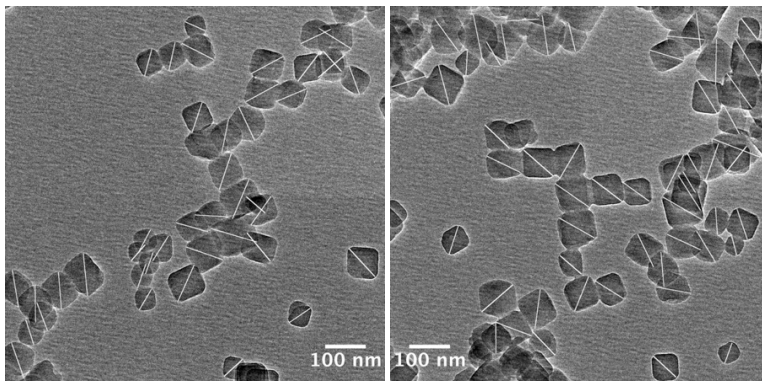


Figure AIV-2. TEM images used to calculate the grain size distribution of the sample “M” with a D50 of 85 nm. White lines are the grain diameter measurements. For this sample grain size, d , equals particle size.

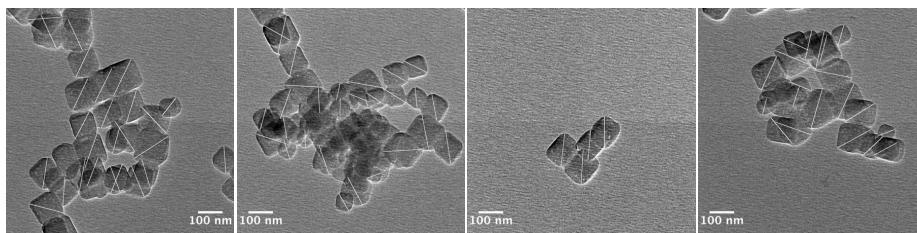


Figure AIV-3. TEM images used to calculate the grain size distribution of the sample “L” with a D50 of 125 nm. White lines are the grain diameter measurements. For this sample grain size, d , equals particle size.

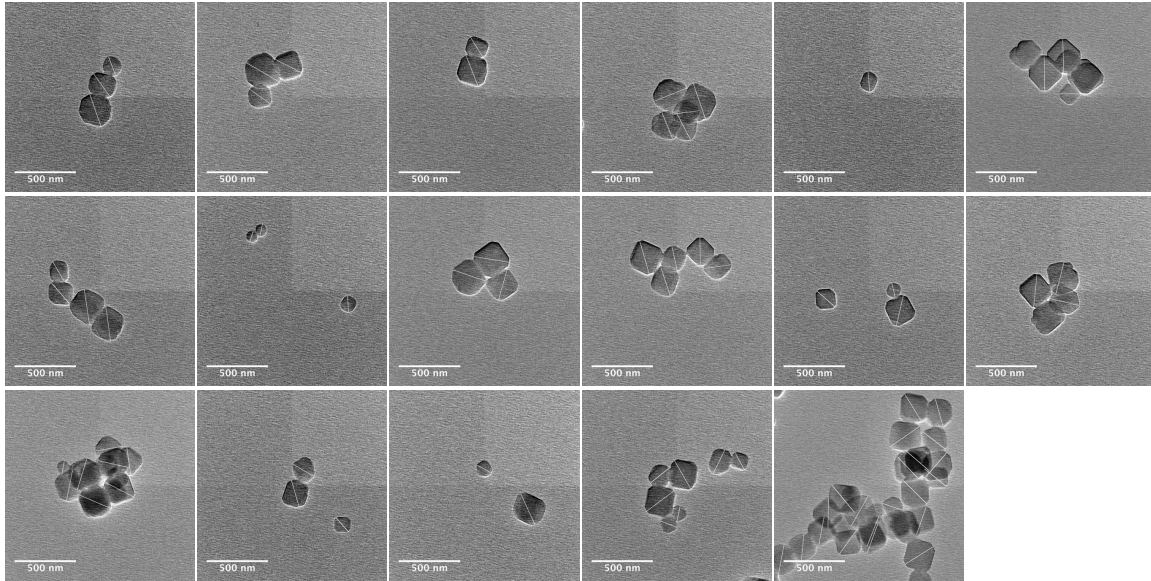


Figure AIV-4. TEM images used to calculate the grain size distribution of the sample “XL” with a D50 of 239 nm. White lines are the grain diameter measurements. For this sample grain size, d , equals particle size.

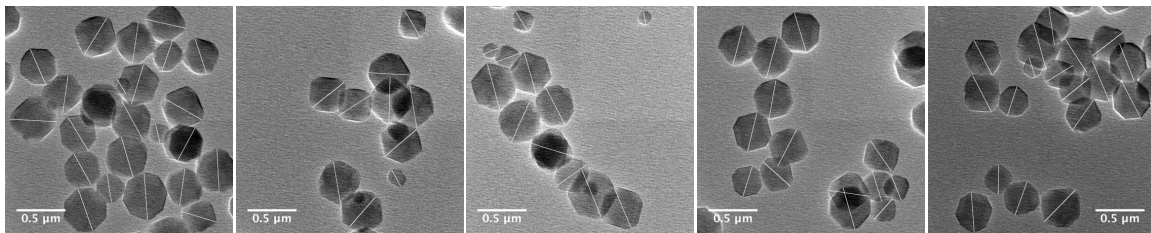


Figure AIV-5. TEM images used to calculate the grain size distribution of the sample “XXL” with a D50 of 404 nm. White lines are the grain diameter measurements. For this sample grain size, d , equals particle size.

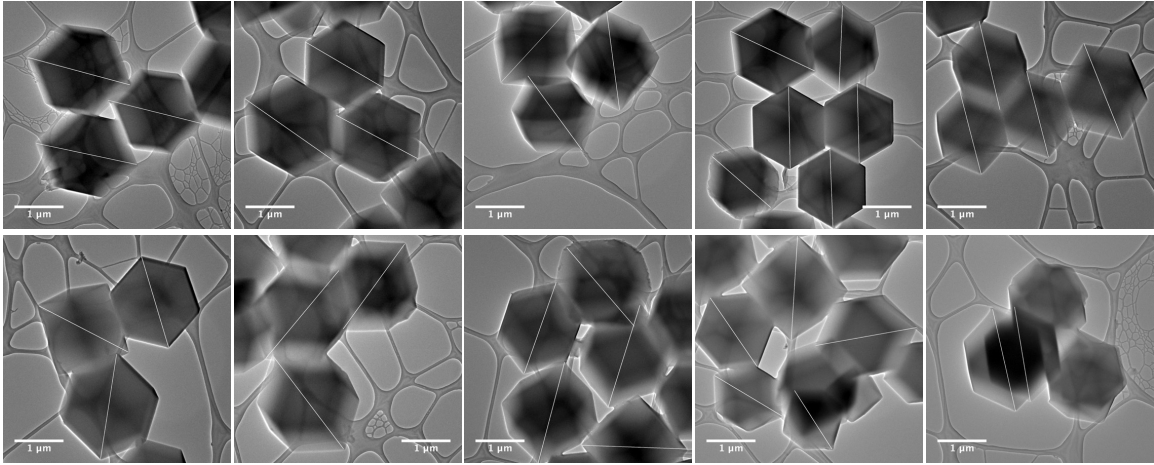


Figure AIV-6. TEM images used to calculate the grain size distribution of the sample with a D50 of 1.96 μm . White lines are the grain diameter measurements. For this sample grain size, d , equals particle size.

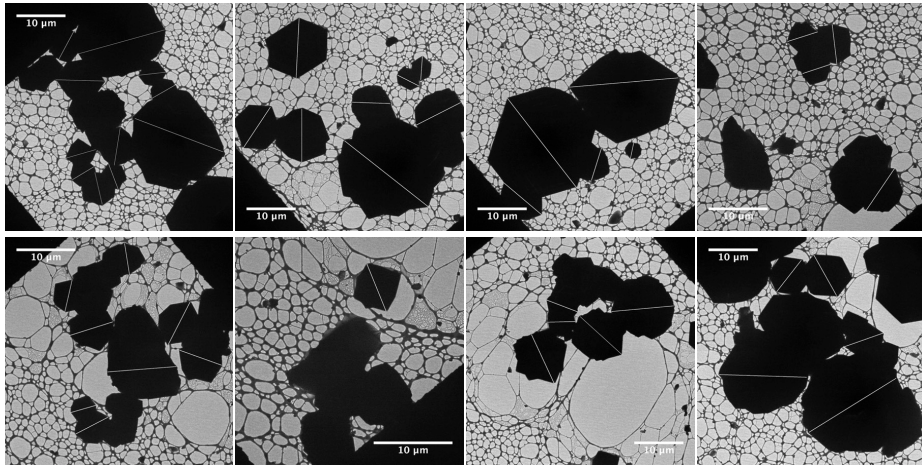


Figure AIV-7. TEM images used to calculate the grain size distribution of the sample with a D50 of 7.76 μm . White lines are the grain diameter measurements.

8.0 APPENDIX V

Solvent properties

Polarity

Parameter	Units	Description	Solvent							Ref.
			DMSO	EtOH	BuOH	MeCN	MeOH	H ₂ O	D ₂ O	
ϵ_r (25 °C)	–	Dielectric constant	46.45	24.55	17.51	35.94	32.66	78.36	78.06	[1]
$\mu \times 10^{30}$	C · m	Dipole moment	13.5	5.8	5.8	13.0	5.9	6.2	–	[1]
E_T^N	–	Ionizing power	0.444	0.654	0.586	0.460	0.762	1.000	0.991	[1–3]

Table AV-1. Parameters of solvent polarity.

Parameters of solvent polarity or ionizing power are valuable for mechanistic studies because a positive correlation of rate with solvent polarity can indicate a buildup of charge in a transition state, which the solvent acts to stabilize. The solvent relative permittivity (dielectric constant), ϵ_r , and dipole moment, μ , are useful for classifying solvents, but are less suitable for quantifying the effect of solvent charge stabilization on reaction rates.¹ Dimroth and Reichardt's solvent polarity parameter, $E_T(30)$ (normalized, E_T^N), is a better measure of solvent ionizing power and is determined empirically from the energy of the absorbance bands of a solvatochromic pyridinium *N*-phenolate betaine dye.^{1–3}

Lewis Acidity

Parameter	Description	Solvent							Ref.
		DMSO	EtOH	BuOH	MeCN	MeOH	H ₂ O	D ₂ O	
α	H-bond donor strength	0	0.86	0.84	0.19	0.98	1.17	–	[1, 4]
A_j	Anion-solvating tendency	0.34	0.66	0.61	0.37	0.75	1.00	–	[1,5]

Table AV-2. Parameters of solvent Lewis acidity.

Parameters of solvent Lewis acidity and hydrogen bond donor strength quantify the solvent's ability to stabilize negative charge and act as a proton donor. Kamlet and Taft's solvatochromic parameter of solvent hydrogen bond donor acidity, α , is widely used in linear solvation energy relationships and was obtained by averaging many solvent-dependent properties.⁴ Swain's acidity parameter, A_j , is a multi-parameter description of solvent Lewis acidity derived from empirical parameters of 77 solvent-sensitive processes and quantifies the solvent's ability to solvate anions.⁵

Lewis Basicity

Parameter	Units	Description	Solvent / molecule								Ref.
			DMSO	EtOH	BuOH	MeCN	MeOH	H ₂ O	D ₂ O	imidazole	
β	–	H-bond acceptor strength	0.76	0.75	0.84	0.40	0.66	0.47	–	–	[1,4]
B_j	–	Cation-solvating tendency	1.08	0.45	0.43	0.86	0.50	1.00	–	–	[1,5]
DN	kcal mol ⁻¹	Lewis basicity	29.8 29.8	32 –	29 –	14.1 14.6	30 19.1	18.0 24.3	–	–	[6] [7]
log β_{ZnTPhP}	–	Lewis basicity for Zn(II)	6.51	2.86	3.19	2.87	2.78	–	–	7.30	[9]
pK_{BHX}	–	H-bond basicity	2.54	1.02	1.02	0.91	0.82	0.65	–	–	[7]
PA	eV	Gas-phase proton affinity	9.17 ¹⁰	8.11 ⁸	8.17 ⁸	8.11 ⁸	7.91 ⁸	7.33 ⁸	–	9.69 ¹¹	[8,10,11]

Table AV-3. Parameters of solvent Lewis basicity.

Parameters of solvent Lewis basicity and hydrogen bond acceptor strength quantify the solvent's ability to stabilize positive charge and correlate with its tendency to act as a ligand for Zn(II). Kamlet and Taft's solvatochromic parameter of solvent hydrogen bond acceptor strength, β , is the widely used counterpart to α .⁴ Swain's basicity parameter, B_j , is the counterpart to A_j and quantifies the solvent's ability to solvate cations.⁵ Gutmann's donor number, DN, scale is an empirical measure of Lewis basicity defined as the $-\Delta H$ of formation of a 1:1 complex of the solvent with SbCl_5 in dilute solution of 1,2-dichloroethane. The DN scale is widely used and hence is included in Table AV-3, however there are discrepancies in reported values for some of the solvents of interest and so other Lewis basicity scales are preferred in this instance.^{6,7} Kolling's electron donor strength scale is attractive because it is based on reactions of solvent reactions with Zn(II), specifically on the solvatochromic shift of the Soret band of (tetraphenylporphyrinato)zinc(II) (ZnTPhP).⁸ Lebedeva extended this concept to derive a basicity parameter, $\log(\beta_{\text{ZnTPhP}})$, based on the formation constants of electron pair donor solvent complexes with ZnTPhP in solution of benzene or carbon tetrachloride.⁹ Their

dataset includes imidazole and so it offers a comparison of the relative strengths of the solvent to act as a ligand versus imidazole. Laurence and Gal's scale of hydrogen bond basicity is defined as the $-\log$ of the equilibrium constant for the hydrogen bonding of 4-fluorophenol to the electron pair donor solvent in carbon tetrachloride at 25 °C.⁷ Their scale covers a very wide range of solvents, does not have the inconsistency problems of the DN scale, and includes water. Finally, the gas-phase proton affinities offer a measure of the Lewis basicity of the solvent molecule that is intrinsic to the isolated molecule and not a function of its ensemble properties.^{10,11}

Brønsted-Lowry Acid/Base

		Solvent						
		DMSO	EtOH	BuOH	MeCN	MeOH	H ₂ O	D ₂ O
pK_a^{Water} of SH $\text{SH} \rightleftharpoons \text{S}^- + \text{H}^+$	Solvent acidity	–	15.9 ¹²	–	–	15.5 ¹³	13.995 ¹	14.951 ¹
pK_a^{DMSO} of SH $\text{SH} \rightleftharpoons \text{S}^- + \text{H}^+$	Solvent acidity	35.1 ¹⁴	29.8 ¹²	–	31.3 ¹⁴	29.0 ¹³	31.4 ¹²	–
pK_a^{Solvent} of ImH ₂ ⁺ $\text{ImH}_2^+ \rightleftharpoons \text{ImH} + \text{H}^+$	Imidazolium acidity	6.4 ¹⁵ 6.94 ²¹	–	–	14.2 ¹⁶ 11.74 ²¹	7.37 ²¹	6.99 ¹⁷ ($\mu = 0$ M) 7.11 ¹⁸ ($\mu = 0.1$ M)	–
pK_a^{Solvent} of ImH $\text{ImH} \rightleftharpoons \text{Im}^- + \text{H}^+$	Imidazole acidity	18.6 ¹³	–	–	30 ¹⁹	–	14.4 ¹⁸ 19.98 ²⁰	–
pK_a^{Solvent} of 2-MelmH ₂ ⁺ $2\text{-MelmH}_2^+ \rightleftharpoons 2\text{-MelmH} + \text{H}^+$	2-methylimidazolium acidity	–	–	–	–	–	8.0 ¹⁷	–
$\log K_{\text{BHB}^+}^{\text{Solvent}}$ for B = ImH	[ImH-H-ImH] ⁺ formation constant	n.m. ²¹	–	–	1.68 ²¹	n.m. ²¹	–	–

Table AV-4. Parameters of solvent Brønsted-Lowry acidity and solvent effects on imidazole and imidazolium acidity (n.m. = not measurable).

Parameters of the Brønsted-Lowry acidity (as pK_a^{medium}) are known for (1) dissociation of the solvent $\text{SH} \rightleftharpoons \text{S}^- + \text{H}^+$ when it is the solute in aqueous (pK_a^{Water}) and DMSO (pK_a^{DMSO}) media and (2) the effect of the solvent when it is the media on the dissociation of imidazole (ImH) and imidazolium (ImH₂⁺).^{12–20} Additionally, homoconjugation constants for the reaction $\text{ImH}_2^+ + \text{ImH} \rightleftharpoons \text{ImH}_2\text{ImH}^+$ ($K_{\text{BHB}^+}^{\text{Solvent}}$) have been determined, with the finding that out of DMSO, MeOH, MeCN, and acetone, ImH₂ImH⁺ only forms in measurable quantities in MeCN and acetone.²¹

Solvent size and mass transport

Parameter	Units	Description	Solvent							Ref.
			DMSO	EtOH	BuOH	MeCN	MeOH	H ₂ O	D ₂ O	
Kinetic diameter	Å	Molecular diameter	–	4.30	5.05	4.28	3.80	2.96	–	[24,25]
MIN-2	Å	Molecular diameter	–	4.27 ²⁶	4.46 ²⁶	–	4.18 ²⁶	3.226 ²⁷	–	[26,27]
σ_{SPT}	Å	Molecular diameter	5.13	4.69	5.58	4.36	4.08	3.43	–	[28]
V_{vdw}	cm ³ mol ⁻¹	Molecular volume	41.8	31.9	52.4	28.4	21.7	12.4	–	[28]
η (25 °C)	mPa s	Viscosity	1.987 ²⁹	1.074 ²⁹	2.54 ²⁹	0.369 ²⁹	0.544 ²⁹	0.890 ¹	1.121 ¹	[1,29]
η (75 °C)	mPa s	Viscosity	–	0.476	0.833	0.234	–	0.378	–	[29]
D_0 (70 °C)	cm ² s ⁻¹	Diffusivity in ZIF-8	–	6.26×10^{-8}	6.8×10^{-13}	–	–	3.39×10^{-7}	–	[30]
E_d	kJ mol ⁻¹	Diffusion activation energy in ZIF-8	–	23.4	26.8	–	–	19.1	–	[30]
S/pore	–	Solvent molecules per pore at saturation	–	8.3 ³¹	5.9 ³¹	–	14 ³¹	48 ³⁴	–	[31–34]

Table AV-5. Solvent molecular sizes and parameters affecting mass transport in solution and in ZIF-8.

ZIF-8 has cage-like pores that are accessible through apertures with a crystallographic diameter of 3.4 Å but that function as if they have a larger effective aperture size for molecular sieving of 4.0–4.2 Å due to framework flexibility.²² Transport of a molecule through a cage-like material like ZIF-8 can be predicted well by the cross section of a molecule, described by a one-dimensional molecular diameter, ignoring the three-dimensional structure. Additionally, although few adsorbents are completely spherical, an assumption of spherical shape is often used in description of molecular size for simplification. To describe molecular size, zeolite and MOF literature frequently cite kinetic diameters, which are the characteristic length scales of the Lennard-Jones potentials in the gas phase (i.e. σ_k in $r_{\text{min}} = 2^{1/6}\sigma_k$).²³ These values have strong predictive power for the molecular sieving of spherical, non-polar molecules in porous materials but are inadequate for polar molecules. Stockmayer length parameters derived from phase-coexistence data offer an analogous treatment for spherical, polar molecules, and are

listed as the kinetic diameters in Table AV-5.^{24,25} Another method of molecular sizing that does not assume that a molecule is spherical is the parameter MIN-2, the second smallest perpendicular distance that encompasses the atomic van der Waals radii, which corresponds to the critical diameter for entrance into a cylindrical pore.²⁶⁻²⁷ A set of molecular sizes that includes DMSO is the molecular diameter from Marcus's scaled particle theory, σ_{SPT} , derived from the packing fraction of the solvent and assuming roughly spherical molecules.²⁸ The van der Waals volume, V_{vdW} is the volume enclosed by the van der Waals radii surface on energy-minimized molecular structures.²⁸ To provide reference, pyrrole, a molecule with a similar size as imidazole, has a σ_{SPT} value of 5.01 Å and a V_{vdW} value of 42.0 cm³ mol⁻¹.

For diffusion-controlled reactions in solution, a correlation between solvent viscosity and reaction rate is often observed. In our present case, diffusion through the micropores of ZIF-8 is more likely to be rate-limiting than transport through bulk solution, but viscosity values at 25 °C and 75 °C are provided for reference.^{1,29} Temperature-dependent diffusion measurements of ethanol, *n*-butanol, and water have been made in ZIF-8, showing the dependence of corrected diffusivity (D_o) and diffusion activation energy (E_d) on molecular size.³⁰ The term E_d arises from the fact that diffusivity in cage-like materials such as ZIF-8 follows an Arrhenius relationship because hopping between pores is the rate-limiting step of diffusion (i.e. activated diffusion). Diffusivities are seen to vary over several orders of magnitude for the three solvents in ZIF-8, and counter diffusion of imidazole may be expected to also vary correspondingly. Significantly, the order of observed reaction rates of in ethanol and *n*-butanol ($k_{\text{obs,EtOH}} < k_{\text{obs,BuOH}}$) is the opposite of what one would expect if D_o controlled the reaction.

Finally, it is interesting to consider how confinement effects of the ZIF-8 pores may limit the number of solvent or imidazole molecules that can participate in a reaction. Solvent molecules per pore at saturation can be calculated from adsorption data,³¹⁻³⁴ converting to molecules per pore from the standard units of mmol g⁻¹ MOF by the formula (data in AV-5):

$$\frac{n \text{ mmol S}}{\text{g ZIF-8}} \cdot \frac{227.59 \times 10^{-3} \text{ g}}{\text{mmol Zn(MeIm)}_2} \cdot \frac{6 \text{ unique Zn}}{\text{pore}} = n \cdot 1.3655 \times 10^3 \text{ molecules/pore}$$

$$\text{E.g. for ethanol: } \frac{6.1 \text{ mmol S}}{\text{g ZIF-8}} \cdot \frac{227.59 \times 10^{-3} \text{ g}}{\text{mmol Zn(MeIm)}_2} \cdot \frac{6 \text{ unique Zn}}{\text{pore}} = 8.3298 \text{ molecules/pore}$$

Additionally, the average number of molecules of imidazole per pore at different [ImH₀] can be estimated (Table AV-6) by assuming that imidazole equilibrates completely through the ZIF-8 crystal and that its concentration in the pore volume equals that in the bulk (no enhancement from adsorption). This situation is unrealistic as we measured kinetics using initial rates, at which point imidazole has not equilibrated throughout the entire pore volume of the crystal, however this simplified picture demonstrates that at no value of [ImH₀] is the calculated average number of molecules of imidazole per pore physically unreasonable. Additional support for the idea that linker substitution is not limited by the number of imidazole molecules that can participate in the reaction due to pore confinement is the absence of saturation kinetics in any of the solvents within the range of [ImH] tested (Figure 3-8), even in those solvents exhibiting second order in imidazole kinetics. Each bridging linker in ZIF-8/**sod**-Zn(MeIm)₂ is shared between 3 neighboring pores, and therefore a second order in imidazole process could involve the two imidazole molecules in separate, adjoining pores.

To arrive at the average number of molecules of imidazole per pore in Table AV-6, we first convert the initial concentration of imidazole, $[\text{ImH}_0]$, from mol/L to molecules/ \AA^3 :

$$\frac{[\text{ImH}_0] \text{ mol}}{\text{L}} \cdot \frac{6.022 \times 10^{23} \text{ molecules}}{\text{mol}} \cdot \frac{\text{L}}{\text{dm}^3} \cdot \frac{\text{dm}^3}{(10^9 \text{\AA})^3} = [\text{ImH}_0] \cdot 6.022 \times 10^{-4} \text{ molecules}/\text{\AA}^3$$

And then calculate the volume of a single pore (in \AA^3) either by using the dimensions of ZIF-8's cubic unit cell (UC) and the void fraction:

$$\frac{(16.99 \text{\AA})^3 \text{ total } V}{\text{UC}} \cdot \frac{\text{UC}}{2 \text{ pores}} \cdot \frac{0.44 \text{ void } V}{\text{total } V} = 1.0790 \times 10^3 \text{\AA}^3/\text{pore}$$

Or by using the density of ZIF-8 (cm^3/g) and the number of unique components (nodes and linkers) per sodalite cage, accounting for sharing (24 total Zn, each shared between 4 cages = 6 unique Zn, and 36 total MeIm^- , each shared between 3 cages = 12 unique MeIm^-):

$$\frac{0.485 \text{ cm}^3}{\text{g}} \cdot \frac{(10^8 \text{\AA})^3}{\text{cm}^3} \cdot \frac{1.3655 \times 10^3 \text{ g}}{\text{mol Zn}_6(\text{C}_4\text{H}_5\text{N}_2)_{12}} \cdot \frac{\text{mol Zn}_6(\text{MeIm})_{12}}{6.022 \times 10^{23} \text{ pores}} = 1.0997 \times 10^3 \text{\AA}^3/\text{pore}$$

And finally convert to molecules per pore (data in Table AV-6):

$$\frac{[\text{ImH}_0] \cdot 6.022 \times 10^{-4} \text{ molecules}}{\text{\AA}^3} \cdot \frac{1.0790 \times 10^3 \text{\AA}^3}{\text{pore}} = 0.6498 \cdot [\text{ImH}_0] \text{ molecules/pore}$$

[imidazole] (M)	Molecules per pore at equilibrium
0.0294	0.02
0.0735	0.05
0.147	0.10
0.294	0.19

Table AV-6. Imidazole molecules per pore on average by the above assumptions and equations.

Appendix V References

- (1) Reichardt, C. and Welton, T. *Solvents and Solvent Effects in Organic Chemistry*, 4th ed. Wiley-VCH, 2011.
- (2) Reichardt, C. Solvatochromic Dyes as Solvent Polarity Indicators *Chem. Rev.* **1994**, *94*, 2319–2358.
- (3) Dimroth, K.; Reichardt, C. Siepmann, T.; Bohlmann, F. *Liebigs Ann. Chem.* **1963**, *661*, 1.
- (4) Kamlet, M. J.; Abboud, J.-L. M.; Abraham, M. H.; Taft, R. W. Linear Solvation Energy Relationships. 23. A Comprehensive Collection of the Solvatochromic Parameters, π^* , α , and β , and Some Methods for Simplifying the Generalized Solvatochromic Equation *J. Org. Chem.* **1983**, *48*, 2877–2887.
- (5) Swain, C. G.; Swain, M. S.; Powell, A. L.; Alunni, S. Solvent effects on chemical reactivity. Evaluation of anion- and cation-solvation components *J. Am. Chem. Soc.* **1983**, *105*, 502–513.
- (6) Marcus, Y. The Effectivity of Solvents as Electron Pair Donors *J. Sol. Chem.* **1984**, *13*, 599–624.
- (7) Laurence, C.; Gal, J.-F. *Lewis Basicity and Affinity Scales: Data and Measurement*. Wiley:Chichester, 2010.
- (8) Kolling, O. W. Comparison of Donor-Acceptor Parameters in Nonaqueous Solvents. *Anal. Chem.* **1982**, *54*, 260–264.
- (9) Lebedeva, N. Sh.; Pavlycheva, N. A.; V'yugin, A. I. Basicity Parameter of Weak Organic Bases, Derived from Thermodynamic Parameters of Their Reactions with (Tetraphenylporphyrinato)zinc(II) *Russian J. Org. Chem.* **2004**, *40*, 1727–1736.

- (10) "Proton Affinities" in CRC Handbook of Chemistry and Physics, 97th Edition (Internet Version 2017), W. M. Haynes, Ed., CRC Press/Taylor & Francis, Boca Raton, FL.
- (11) Scheiner, S.; Yi, M. Proton Transfer Properties of Imidazole *J. Phys. Chem.* **1996**, *100*, 9235–9241.
- (12) Olmstead, W. N.; Margolin, Z.; Bordwell, F. G. Acidities of water and simple alcohols in dimethyl sulfoxide solution *J. Org. Chem.* **1980**, *45*, 3295–3299.
- (13) Bordwell, F. G. Equilibrium acidities in dimethyl sulfoxide solution *Acc. Chem. Res.* **1988**, *21*, 456–463.
- (14) Matthews, W. S.; Bares, J. E.; Bartmess, J. E.; Bordwell, F. G.; Cornforth, F. J.; Drucker, G. E.; Margolin, Z.; McCallum, R. J.; McCollum, G. J.; Vanier, N. R. Equilibrium acidities of carbon acids. VI. Establishment of an absolute scale of acidities in dimethyl sulfoxide solution *J. Am. Chem. Soc.* **1975**, *97*, 7006–7014.
- (15) Crampton, M. R. and Robotham, I. A. Acidities of Some Substituted Ammonium Ions in Dimethyl Sulfoxide *J. Chem. Res. (S)*, **1997**, 22-23.
- (16) Pawlak, Z.; Urbanczyk, G. *J. Mol. Struct.* **1988**, *177*, 401–6. Cited in: Streitwieser, A.; Kim, Y.-J. Ion Pair Basicity of Some Amines in THF: Implications for Ion Pair Acidity Scales¹ *J. Am. Chem. Soc.* **2000**, *122*, 11783–11786.
- (17) Goldberg, R. N.; Kishore, N.; Lennen, R. M. Thermodynamic Quantities for the Ionization Reactions of Buffers *J. Phys. Chem. Ref. Data* **2002**, *31*, 231–370.
- (18) Catalán, J.; Claramunt, R. A.; Elguero, J.; Laynez, J.; Menéndez, M., Anvia, F.; Quiñan, J. H.; Taagepera, M.; Taft, R. W. Basicity and acidity of azoles: the annelation effect in azoles *J. Am. Chem. Soc.* **1988**, *110*, 4105–4111.

- (19) Calculated value: Ding, F.; Smith, J. M.; Wang, H. First-Principles Calculation of pK_a Values for Organic Acids in Nonaqueous Solution *J. Org. Chem.* **2009**, *74*, 2679–2691.
- (20) Calculated value: Magill, A. M.; Yates, B. F. An Assessment of Theoretical Protocols for Calculation of the pK_a Values of the Prototype Imidazolium Cation *Aust. J. Chem.* **2004**, *57*, 1205–1210.
- (21) Kozak, A.; Czaja, M.; Chmurzyński, L. Investigations of (acid + base) equilibria in systems modelling interactions occurring in biomolecules *J. Chem. Thermodyn.* **2006**, *38*, 599–605.
- (22) Zhang, C.; Lively, R. P.; Zhang, K.; Johnson, J. R.; Karvan, O.; Koros, W. J. Unexpected Molecular Sieving Properties of Zeolitic Imidazolate Framework-8 *J. Phys. Chem. Lett.* **2012**, *3*, 2130-2134.
- (23) Breck, D. W. Zeolite Molecular Sieves; John Wiley & Sons: New York, 1974. pp. 634–636.
- (24) Bowen, T. C.; Noble, R. D.; Falconer, J. L. Fundamentals and applications of pervaporation through zeolite membranes *J. Membr. Sci.* **2004**, *245*, 1–33. Citing:
- (25) van Leeuwen, M. E. Derivation of Stockmayer potential parameters for polar fluids *Fluid Phase Equilib.* **1994**, *99*, 1–18. The 1-butanol value was excluded by Bowen et al. because of its non-spherical shape but is included here.
- (26) Webster, C. E., Drago, R. S., and Zerner, M. C. Molecular Dimensions for Adsorptives *J. Am. Chem. Soc.* **1998**, *120*, 5509–5516.

- (27) Fletcher, A. J. and Thomas, K. M. Compensation Effect for the Kinetics of Adsorption/Desorption of Gases/Vapors on Microporous Carbon Materials *Langmuir* **2000**, *16*, 6253–6266. (water, MeOH, EtOH, BuOH)
- (28) Marcus, Y. *The Properties of Solvents*; Wiley:Chichester, 1998. pp. 85–94.
- (29) "Viscosity of Liquids" in CRC Handbook of Chemistry and Physics, 97th Edition (Internet Version 2017), W. M. Haynes, ed., CRC Press/Taylor & Francis, Boca Raton, FL.
- (30) 1-Butanol value taken directly and EtOH and H₂O values extrapolated from Arrhenius plots in: Zhang, K.; Lively, R. P.; Zhang, C.; Chance, R. R.; Koros, W. J.; Sholl, D. S.; Nair, S. Exploring the Framework Hydrophobicity and Flexibility of ZIF-8: From Biofuel Recovery to Hydrocarbon Separations *J. Phys. Chem. Lett.* **2013**, *4*, 3618–3622.
- (31) The alcohol values are from simulation results in 34a, but agree well with experimental results from refs [30], [33], and [34]
- (32) Zhang, K.; Zhang, L.; Jiang, J. Adsorption of C₁–C₄ Alcohols in Zeolitic Imidazolate Framework-8: Effects of Force Fields, Atomic Charges, and Framework Flexibility *J. Phys. Chem. C* **2013**, *117*, 25628–25635.
- (33) Zhang, K.; Lively, R. P.; Dose, M. E.; Brown, A. J.; Zhang, C.; Chung, J.; Nair, S.; Koros, W. J.; Chance, R. R. Alcohol and water adsorption in zeolitic imidazolate frameworks *Chem. Commun.* **2013**, *49*, 3245–3247.
- (34) Zhang, K.; Lively, R. P.; Zhang, C.; Koros, W. J.; Chance, R. R. Investigating the Intrinsic Ethanol/Water Separation Capability of ZIF-8: An Adsorption and Diffusion Study *J. Phys. Chem. C* **2013**, *117*, 7214–7225.